The Dissertation Committee for Ruijie Liu
certifies that this is the approved version of the following dissertation:

Discontinuous Galerkin Finite Element Solution for Poromechanics

Committee:

Mary F. Wheeler, Supervisor

Clint N. Dawson, Supervisor

Mark E. Mear

J. Tinsley Oden

John L. Tassoulas

Discontinuous Galerkin Finite Element Solution for Poromechanics

by

Ruijie Liu, B.S., M.S.

DISSERTATION

Presented to the Faculty of the Graduate School of

The University of Texas at Austin

in Partial Fulfillment

of the Requirements

for the Degree of

DOCTOR OF PHILOSOPHY

THE UNIVERSITY OF TEXAS AT AUSTIN

December 2004

Dedicated to my wife Aiju and my daughter Pai.

Acknowledgments

I would like to express my deepest appreciation to my advisor, Dr. Mary F. Wheeler, for her wonderful unremitting guidance on this research. As an erudite mentor, she showed me the beauty of the mathematical theories and applications to engineering sciences. I greatly value her enthusiasm and persistence on doing a rigor research. The greatest appreciation is also attributed to my coadvisor, Dr. Clint N. Dawson, for his generous advices on my graduate study and research work. In particular, I'm grateful to him for his introducing me to Dr. Wheeler and letting me share their DG ideas.

A special thank goes to Dr. Rick Dean, who let me share his wonderful industrial research experience and knowledge and taught me advanced plasticity theory and geomechanics. For wonderful suggestions, comments and references, I thank the members of my committee, Dr. Mark Mear, Dr. Tinsley Oden and Dr. John Tassoulas. Also, I thank Dr. Wolfgang Bangerth and Dr. Shuyu Sun for their reading and suggestions on my dissertation draft.

I am very thankful to many friends and colleagues in Aerospace and Engineering Mechanics Department and Institute for Computational Engineering and Sciences, in particular to Dr. Vadym Aizinger, Mr. Owen Eslinger, Dr. Xiuli Gai, Dr. Hector Klie, Dr. Douglas Migliano, Mr. Phillip Phillips, Dr. Jennifer Proft, Dr. Albert Romkes, Dr. Raul Tempone, Dr. Mingji Wang. Es-

pecially, I thank Connie Baxter and Andrew Pacetti at Center for Subsurface Modeling for their kind help.

Finally, of course without the unselfish support from my dear wife Aiju and daughter Pai I would never have finished this dissertation work. In particular, I'm grateful to my daughter Pai for her yielding whenever I want to work on weekends.

Discontinuous Galerkin Finite Element Solution for Poromechanics

Publication No. _____

Ruijie Liu, Ph.D.
The University of Texas at Austin, 2004

Supervisors: Mary F. Wheeler
Clint N. Dawson

This dissertation focuses on applying discontinuous Galerkin (DG) methods to poromechanics problems. A few challenges have been presented in traditional and popular continuous Galerkin (CG) finite element methods for solving complex coupled thermal, flow and solid mechanics. For example, nonphysical pore pressure oscillations often occur in CG solutions for poroelasticity problems with low permeability. A robust and practical numerical scheme for removing or alleviating the oscillation is not available. In modeling thermoporoelastoplasticity, CG methods require the use of very small time steps to obtain a convergent solution. The temperature profile predicted by CG methods in the fine mesh zones is often seriously polluted by large errors produced in coarse mesh zones in the case where the convection dominates the thermal process. The nonphysical oscillations in pore pressure and temperature solutions induced by CG methods at very early time stages seriously corrupt the solutions at longer time. We propose DG methods to handle

these challenges because they are physics driven, provide local conservation of mass and momentum, have high stability and robustness, are locking-free, and because of their meshing and implementation capabilities.

We first apply a family of DG methods, including Oden-Babuska-Baumann (OBB), Nonsymmetric Interior Penalty Galerkin (NIPG), Symmetric Interior Penalty Galerkin (SIPG) and Incomplete Interior Penalty Galerkin (IIPG), to 3D linear elasticity problems. This family of DG methods is tested and evaluated by using a cantilever beam problem with nearly incompressible materials. It is shown that DG methods are simple, robust and locking-free in dealing with nearly incompressible materials. Based on the success of DG methods in elasticity, we extend the DG theory into plasticity problems. A DG formulation has been implemented for solving 3D poroelasticity problems with low permeability. Numerical examples solved by DG methods demonstrate that the nonphysical pore pressure oscillation can be avoided. Finally, we apply DG schemes to thermoporoelastoplasticity problems, which are of high nonlinearity. Excellent performance of DG methods in avoiding nonphysical pressure and temperature oscillations and in blocking error propagation from coarse mesh zones into fine mesh zones is clearly observed.

Table of Contents

Acknowledgments **v**

Abstract **vii**

List of Tables **xiii**

List of Figures **xiv**

Chapter 1. Introduction **1**

1.1 Research Motivation 1
1.2 Bibliographical Review 3
1.2.1 Poromechanics Theory 3
1.2.2 Continuous Galerkin (CG) Methods 6
1.2.3 Discontinuous Galerkin (DG) Methods 8
1.3 Contributions 11
1.4 Outline of Dissertation 14

Chapter 2. Modeling Linear Elasticity **16**

2.1 Objective 16
2.2 Mathematical Theory of Elasticity 16
2.3 DG Variational Formulation 18
2.4 DG Implementation 22
2.5 Convergence Analysis 25
2.6 A Bracket in Bending 28
2.7 A Breast Reconstruction Model 33
2.8 Summary 38

Chapter 3. Modeling Plasticity **42**
3.1 Objective . . . 42
3.2 Theory of Plasticity . . . 43
3.2.1 Governing Equations . . . 43
3.2.2 Plastic Behavior . . . 46
3.2.3 Evolutionary Modulus . . . 48
3.2.4 Material Models . . . 50
3.3 DG Variational Formulation . . . 56
3.4 DG Implementation . . . 57
3.4.1 Integration of Constitutive Law . . . 58
3.4.2 Stresses on Faces . . . 60
3.4.3 Iteration on Material Level . . . 62
3.4.4 Iteration on Global Level . . . 65
3.5 A Beam in Bending . . . 68
3.6 Summary . . . 70

Chapter 4. Modeling Poroelasticity-I **74**
4.1 Objective . . . 74
4.2 Governing Equations . . . 74
4.2.1 Notations . . . 74
4.2.2 Material Constants . . . 76
4.2.3 Governing Equations . . . 77
4.3 CG Solutions . . . 80
4.3.1 Abstract Spaces and Bilinear Forms . . . 80
4.3.2 Variational Formulation . . . 82
4.3.3 Discretization in Spatial Domain . . . 83
4.3.4 Discretization in Temporal Domain . . . 84
4.3.5 Stable and Unstable Methods . . . 85
4.4 Nonphysical Pressure Oscillation . . . 88
4.4.1 Mandel Problem . . . 88
4.4.1.1 Problem Statement . . . 88
4.4.2 Analytical Solution . . . 90

4.4.3 CG Solution . . . 93
4.4.3.1 Time Step Effect . . . 93
4.4.3.2 Element Type Effect . . . 96
4.4.3.3 Permeability Effect . . . 96
4.4.3.4 Compressibility Effect . . . 100
4.4.4 Discussion . . . 100
4.5 Summary . . . 105

Chapter 5. Modeling Poroelasticity-II **106**
5.1 Objective . . . 106
5.2 DG Formulation for Poroelasticity . . . 107
5.3 A Porous Rock Sample in Compression . . . 111
5.4 A Lacunar Bone Sample in Compression . . . 113
5.5 Summary . . . 115

Chapter 6. Modeling Poroelasticity-III **116**
6.1 Objective . . . 116
6.2 CCFD for Flow . . . 117
6.3 Numerical Study . . . 120
6.4 Summary . . . 127

Chapter 7. Modeling Thermoporoelastoplasticity **128**
7.1 Objective . . . 128
7.2 Three-Field Theory . . . 129
7.2.1 Governing Equations . . . 129
7.2.2 Constitutive Equations . . . 130
7.2.3 Boundary and Initial Conditions . . . 132
7.2.4 Problem Statement . . . 134
7.3 DG Weak Formulation . . . 134
7.4 DG Implementation . . . 142
7.5 A Single Injection Well . . . 145
7.5.1 Thermoporoelasticity . . . 148
7.5.2 Plasticity Effect . . . 157
7.6 Summary . . . 158

Chapter 8. Conclusions and Future Work **164**
8.1 Conclusions 164
8.2 Future Work 167

Bibliography **169**

Vita **186**

List of Tables

5.1 Mechanical Properties of Bone and Rock (S. Cowin, Bone Poroelasticity, J. of Biomechanics, 32 vol., 1999) 113

7.1 Data for Injection Well 149

7.2 Plastic Parameters for Injection Well Problem 158

List of Figures

2.1 A Domain and Its Boundary 17

2.2 Local Faces 19

2.3 Isoparametric Hexahedral Elements; Corner Nodes in Red . . 24

2.4 Procedures of DG Program for Elasticity 26

2.5 Nodal Stresses Extrapolated by Stresses at Interior GIP . . . 27

2.6 A Bracket Problem 29

2.7 Tensile Stress Contours ($\sigma_y > 0.15\,Mpa$) of CG Solutions of Bracket Problem. (a) Poisson Ratio = 0.3; $(\sigma_y)_{max} = 0.51\,Mpa$; Tip Deflection = 1.61 mm. (b) Poisson Ratio = 0.499; $(\sigma_y)_{max} = 0.86\,Mpa$; Tip Deflection = 1.12 mm. 31

2.8 Tensile Stress Contours ($\sigma_y > 0.15\,Mpa$) of DG Solutions of Bracket Problem with Poisson's Ratio 0.499. (a) OBB; $(\sigma_y)_{max} = 0.75\,Mpa$; Tip Deflection = 1.62 mm. (b) NIPG; $(\sigma_y)_{max} = 0.68\,Mpa$; Tip Deflection = 1.62 mm. (c) SIPG; $(\sigma_y)_{max} = 0.55\,Mpa$; Tip Deflection = 1.62 mm. (d) IIPG; $(\sigma_y)_{max} = 0.59\,Mpa$; Tip Deflection = 1.62 mm. 32

2.9 A Breast Reconstructive Model Under Gravity Loading 36

2.10 Evolution Progress of Deformation and Stress of Reconstructed Breast under Gravity Loading Predicted by CG Method: Tensile Stress in Horizontal Direction Is Contoured in Red Color; $(\sigma_y)_{max} = 1349\,Pa$, $(u_z)_{max} = -34\,mm$. 37

2.11 Evolution Progress of Deformation and Stress of Reconstructed Breast under Gravity Loading Predicted by DG Method: Tensile Stress in Horizontal Direction Is Contoured in Red Color; $(\sigma_y)_{max} = 484\,Pa$, $(u_z)_{max} = -37\,mm$. 39

2.12 Geometry Updating of Reconstructed Breast under Gravity Loading (DG). 40

3.1 Admissible Stress Space and Set 44

3.2 Material Hardening 47

3.3 The Drucker-Prager Model without Cap 53

3.4 Elliptic Cap in the Drucker-Prager Model 54
3.5 Drucker-Prager's Model with Cap 55
3.6 Extrapolation of Elastoplastic and Stress Tensors at Interior GIP for GIP on Surfaces 61
3.7 Radial Stress Return 62
3.8 Radial Stress Return Scheme 65
3.9 Nonlinear Iteration Methods 66
3.10 Newton-Raphson Method for Plasticity 67
3.11 A Beam in Pure Bending 69
3.12 Meshing Profile of Beam Problem Solved by CG 69
3.13 Plastic Development and Propagation of Beam Predicted by CG Simulation 71
3.14 Broken Elements for DG Methods 72
3.15 Plastic Development and Propagation of Beam Predicted by DG Simulation 73

4.1 Mandel Problem 89
4.2 Mandel Problem: Analytical Solution of Pore Pressure 92
4.3 Mandel's Problem: CG Solution of Pore Pressure; Incompressible Case; Linear-Linear Element. 94
4.4 Mandel's Problem: CG Solution of Pore Pressure; Incompressible Case; Linear-Linear Element; Much Larger Time Step . . 95
4.5 Mandel's Problem: CG Solution of Pore Pressure; Incompressible Case; Taylor-Hood's Element. 97
4.6 Mandel's Problem: CG Solution of Pore Pressure; Incompressible Case; Linear-Linear Element; Relatively Lower Permeability 98
4.7 Mandel's Problem: CG Solution of Pore Pressure; Incompressible Case; Taylor-Hood's Element; Relatively Lower Permeability 99
4.8 Mandel Problem: CG Solution of Pore Pressure; Compressible Case; Linear-Linear Element 101
4.9 CG Solution of Pore Pressure; Compressible Case; Linear-Linear Element; Relatively Lower Permeability 102
4.10 CG Solution of Pore Pressure; Compressible Case; Taylor-Hood's Element 103
4.11 CG Solution of Pore Pressure; Compressible Case; Taylor-Hood's Element; Relatively Lower Permeability 104

5.1 Pressure Distributions of DG and CG Solutions of Mandel's Problem 112
5.2 Pressure Distributions of DG and CG Solutions of Bone Problem 114
5.3 Pressure Distributions of DG and CG Solutions of Bone Problem 115

6.1 A Cantilever Bracket Problem 121
6.2 Pressure Distribution of CG-CCFD Solution at Earlier Stage for Cantilever Bracket Problem with High Permeability. 122
6.3 Pressure Distribution of CG-CCFD Solution at Earlier Stage for Cantilever Bracket Problem with Low Permeability. 123
6.4 Pressure Distribution of CG-CCFD Solution at Longer time for Cantilever Bracket Problem with Low Permeability. 124
6.5 Pressure Contour of CG-CCFD Solution at Earlier Stage for Cantilever Bracket Problem with Low Permeability. 125
6.6 Pressure Distribution of DG-CCFD Solution at Earlier Stage for Cantilever Bracket Problem with Low Permeability. 126
6.7 Pressure Contour of DG-CCFD Solution at Earlier Stage for Cantilever Bracket Problem with Low Permeability. 127

7.1 Dirichlet and Neumann Boundaries of the 3-Field Problems . . 133
7.2 Flow Diagram of DG for Thermoporoelastoplasticity Problems 146
7.3 (a) Geometric Profile of a Single Well Model and (b) Well Computational Model 147
7.4 Meshing of Injection Well 149
7.5 Evolution of Pressure Profile for the Injection Well Problem Predicted by DG and Analytical Methods. 151
7.6 Comparison of Conduction and Convection Effects Predicted by CG Methods. 153
7.7 Temperature Profile at Early Time Predicted by CG and DG Methods. 154
7.8 Evolution of Temperature Profile Obtained from CG methods (thermoporoelasticity model). (a) t=10 seconds; (b) t=800 seconds; (c) t=1450 seconds; (d) t=1700 seconds; (e) t=1850 seconds; (f) t=1950 seconds. 155
7.9 Evolution of Temperature Profile Obtained from DG methods (thermoporoelasticity model). (a) t=10 seconds; (b) t=800 seconds; (c) t=1450 seconds; (d) t=1700 seconds; (e) t=1850 seconds; (f) t=1950 seconds. 156

7.10 Well Compaction Predicted by DG Methods 157
7.11 Evolution of Temperature Profile Obtained from CG methods (thermoporoelastoplasticity model). (a) t=10 seconds; (b) t=800 seconds; (c) t=1450 seconds; (d) t=1700 seconds; (e) t=1850 seconds; (f) t=1950 seconds. 159
7.12 Evolution of Temperature Profile Obtained from DG methods (thermoporoelastoplasticity model). (a) t=10 seconds; (b) t=800 seconds; (c) t=1450 seconds; (d) t=1700 seconds; (e) t=1850 seconds; (f) t=1950 seconds. 160
7.13 Development of Plastic Zone. (a) t=1 second; (b) t=50 seconds; (c) t=200 seconds; (d) t=550 seconds; (e) t=750 seconds; (f) t=950 seconds. 161
7.14 Well Compaction Predicted by Plasticity Theory and DG Methods 162

Chapter 1

Introduction

1.1 Research Motivation

Porous media are solid skeletons containing pores connected and filled with fluids. The deformation of solid skeletons and the flow of fluids are coupled. In general, the diffusion of fluid pressure is accompanied with the consolidation of the media. The process is also time-dependent. Many materials and structures such as soils, rocks, soft tissues, and bones can be viewed as porous media. A strict mathematical theory on poromechanics was first established by Terzaghi and Biot [11–14, 109]. Poromechanics has many important applications in civil engineering, petroleum engineering, and biomedical engineering. The prediction of the subsidence of a high-rise building built on a soft foundation is the key to avoid the functional failure of the building. The effective management of underground water extraction relies on the reliable evaluation of the subsidence of the ground surface. The modeling of oil well problems by poromechanics theory can provide valuable information regarding well failure and sand production. The deformation of soft tissue and the flow of blood can be modeled using poromechanics. Poromechanics is also valuable in the study of bone deformation and healing.

However, the number of poromechanics problems that can be solved analytically is highly limited due to the complex coupled nature of the problems. In practical applications, generally, we have to seek numerical solutions. The most popular numerical method is the continuous Galerkin (CG) finite element method, in particular in commercial finite element packages. Engineers can use these packages to model problems with very complex geometries and materials. Along with much success in practical applications, traditional CG methods have also met a few challenges in dealing with poromechanics [44, 63, 86, 95, 111]. First of all, the performance of the popular CG methods is problem-dependent. A nonphysical pressure oscillation often occurs in the zones with low permeabilities when small time steps are used. When thermal effects are taken into account, all too frequently the CG solutions become even more oscillatory. This is contrary to the common expectation in computational fluid and structural dynamics fields that the smaller the time step, the better the accuracy. While removing and alleviating the oscillation has been a subject of considerable research [86, 94, 114, 122] for many years, a robust and practical scheme is still unavailable. Second, CG is not able to efficiently model problems that have an abrupt change in the pressure or temperature field. For example, when the thermal behavior is dominated by convection, the temperature field has a jump discontinuity. CG always gives a smooth temperature field not matching the actual jump. Third, to implement local refinement often needed in practical applications, a tremendous effort must be invested for CG methods to avoid any meshing with hanging nodes. For

example, complex transition elements are designed and used in the transition zones between coarse and fine meshes.

It is known that the discontinuous Galerkin finite element method (DG) has attractive advantages over CG. These advantages include local mass and momentum conservation, high stability of schemes, ability to model fields with discontinuities, and easy meshing and implementation. These features strongly motivate us to apply DG to poromechanics problems to remove oscillations. In this dissertation, we discuss the formulation, implementation, and provide a numerical study of DG for poromechanics systems, and we conclude that DG is a powerful alternative for solving these multi-field coupled problems.

1.2 Bibliographical Review

1.2.1 Poromechanics Theory

The first study on the mechanical response of one-dimensional fluid-saturated porous soil problems was given by Terzaghi [109] in 1923. He first established the effective stress concept by which the deformation of solid skeletons is controlled. Terzaghi decoupled the flow equation and the equilibrium equation by assuming that the total stress at any point remains constant for time-independent loading. Thus, changes in the pore fluid pressure are equal to variations of the volumetric effective stresses. The effective stress theory became the cornerstone of poromechanics theory.

Later, using Terzaghi's effective stress theory, Biot [11] derived a set of complete governing equations for three-dimensional poroelasticity problems,

which is now referred to as Biot's consolidation theory. It differs from Terzaghi's theory in that the pore pressure diffusion process is coupled to the rate of volumetric change in solid skeletons. Many practical problems can be solved using Biot's theory. Furthermore, more complex poromechanics theories dealing with plasticity and thermal effect can easily be derived from the framework of Biot's consolidation theory. Therefore, Biot's theory plays a key role in modeling poromechanics.

The original Biot's poroelasticity theory has been revisited [12–14, 88]. An important reformulation of Biot's theory was done by Rice and Cleary [88]. They formulated the equations using material coefficients that are more concise and easier to use in practical applications.

Poroplasticity theory is a natural extension of Biot's theory when considering the nonlinear behavior of solid materials [63, 98, 99, 104]. In 1970's, the thermal effect was incorporated into Biot's equations to study the consolidation of water and oil reservoirs due to hot water injection or pumping [10, 21]. A general theory of thermoporoelastoplasticity for saturated materials was introduced by Coussy [30].

A considerable effort has been focused on seeking analytical solutions for poromechanics problems. Problems with analytical solutions may provide limited help to complex applications in practice but play a key role in the validation of numerical methods. The 1-D Terzaghi problem [109] can be solved analytically in the cases where solid skeletons are linear elastic. The pore pressure in the Terzaghi solution always monotonically diffuses over time.

Mandel [68] gave an analytical solution for a 2-D plane strain problem based on Biot's consolidation theory. The solution demonstrates a non-monotonic pore pressure response. This non-monotonic behavior of pore pressure was also presented by Cryer [32] and is referred to as the Mandel-Cryer effect. This interesting phenomenon was proved and validated by Verruijt [112, 113] through field experiment tests.

However, the classic Mandel problem assumes that both solid grains and fluid particles are incompressible. In 1988, Cheng and Detournay [23] obtained a complete analytical solution for the Mandel problem that takes into account the effect of the compressible behavior of solid grains and fluid particles. The importance of their work is that the solution can be applied to rocks and bones where the compressible effect is significant. Moreover, because of their elegant and detailed documentation, the solution of this extended Mandel problem has become a popular benchmark for the validation of numerical schemes of poroelasticity.

In the analytical solutions for more general and complex cases including shear stresses, Gibson presented solutions for half-space [70] and strip footing problems [45] and Detournay and Cheng [37] for borehole problems. Due to the complex coupling nature, few analytical solutions are available for nonlinear poromechanics.

1.2.2 Continuous Galerkin (CG) Methods

The most popular numerical techniques for solving poromechanics problems are the continuous Galerkin (CG) finite element methods. The first application of the CG finite element methods began in 1969 by Sanhu and Wilson [96]. Their finite element formulation was based on Gurtin's variational principle [47] and applied to true three-dimensional soil consolidation problems, which was revisited by Yokoo [123]. The stability of the CG methods was first briefly commented on by Ghaboussi and Wilson [44]. They pointed out that a very small time step results in oscillatory pressure for problems with low permeability. However, they didn't present their unstable results obtained by small time steps.

The earliest appropriate use of finite element spaces for consolidation problems is attributed to Hwang et al [57]. In their numerical study on plane strain consolidation problems, a six node triangle was used to represent a quadratic displacement field and a three node triangle was selected to represent a linear pore pressure field. These proposed finite element spaces happened to represent a stable scheme, which satisfies the Ladyzhenskaya-Babuska-Brezzi(LBB) inf-sup condition [19]. However, this scheme is not popular in practical applications due to the constraint on approximation spaces which requires complex programming.

Vermeer and Verruijt [111] were the first who demonstrated nonphysical pressure oscillations in CG finite element solutions, which are induced by using small time steps. Their stability analysis was based on a 1-D problem.

They showed that there is a time step lower bound dependent on the order of the finite elements employed, below which spatial oscillations in pressure will occur. The oscillation in pressure solutions for 2-D problems solved by some composite elements for displacement and pressure was studied by Reed [86].

Zienkiewicz and Shiomi [126] discussed various CG formulations for soil consolidation problems. Mixed finite elements, reduced integrations, and penalty methods [19, 67, 79], which were studied and used for dealing with incompressible elasticity problems and Stokesian flows, were proposed for consolidation problems with incompressible fluid models. Their work implied that the stability issues of numerical schemes for consolidation problems could be studied by mixed finite element theories.

The stability analysis in time was performed by Booker and Small [15]. Their work showed that the time parameter has to be set above 0.5 in order to get a stable result. A formal mathematical stability analysis of CG in the spatial domain for 2-D consolidation problems with incompressible solid grains and fluid particles was given by Murad [71–73]. He used Wheeler's elliptic projection theory [117] to derive an error estimate and also proved the oscillation decay behavior of CG solutions for pressure. A convergence analysis for coupled mixed and Galerkin finite element methods for poroelasticity has been performed by Wheeler and Phillips [85].

A few techniques have been proposed to remove the oscillation in pressure solution obtained by the popular CG methods. An obvious technique is to use a fine mesh or a high order element near the boundary. Indeed, this

method can help to alleviate the oscillation. But it is not able to completely remove the oscillation until an extremely fine mesh is used, which is not practical. Sanhu [94, 95] proposed to use singular elements near the loaded surface. However, the appropriate polynomial degree of singular elements could exceed 60, which could be difficult for its computer implementation. Wan et al [114] recommended a stabilized scheme for CG applied to consolidation problems. An intensive search for an appropriate stabilizing parameter is required for this stabilized CG method.

There is a rich literature for CG applications to various practical poromechanics problems. For civil engineering applications, we refer to [16, 17, 33, 62, 63, 104, 126]. Applications in the area of petroleum engineering can be found in [24, 35, 36, 42, 97–99]. For biomedical engineering, we refer to [31, 64, 75, 125].

1.2.3 Discontinuous Galerkin (DG) Methods

In this section we review the development of DG methods. The properties and advantages of DG methods are introduced through this review. A family of DG methods are proposed for solving poromechanics in this dissertation.

Wilson's nonconforming elements [108] were used for solving fourth order differential equations of plate and shell problems. Discontinuous finite element spaces were proposed by Oden and Wellford [115] for elastic wave propagation problems. These discontinuous spaces are either used to tackle the locking obtained by CG or designed to fit the sharp discontinuity in shock

waves. The idea of DG finite element methods originated from Nitsche's work in 1971 [74]. Instead of enforcing the Dirichlet boundary condition strongly in CG methods, he did it weakly. In 1976, the continuity of the stress in elliptic equations and the flux in parabolic equations across the interior faces between elements was weakly enforced by Douglas and Dupont [38]. The Interior Penalty Galerkin (IPG or SIPG) finite element method was first derived and formulated for second order elliptic equations by Wheeler [118] and Wheeler and Percell [84]. In their DG formulations, the stiffness contributed from interior faces is obtained by using the average of tractions and jumps on primary variables across the faces between elements. Also, the continuity condition of the primary variable is controlled by adding a penalty term involving the jump on the primary variable and its corresponding test function. If the penalty parameter is set to infinity, DG coincides with CG. The IPG method was exploited by Arnold [4] to solve parabolic equations and nonlinear elliptic problems.

Much research work has been focused on CG methods since finite element methods were just developed. Recently, DG methods have become more popular and have been exploited to deal with the challenges that CG methods are not able to handle easily. A non-symmetric DG method was proposed by Oden, Babuska and Baumann (OBB) [77] to solve diffusion problems. The formulation of OBB results in a positive definite stiffness matrix. Therefore, the method is more stable and robust than the symmetric DG formulation. Also, it exhibits a property of local mass conservation at the element level,

which is very important for solving convection and/or diffusion problems. In addition, another family of DG different from the primal DG, the local DG (LDG), was developed by Cockburn and Shu [28] and extended by Cockburn and Dawson [26, 28] for convection-diffusion equations in multi-dimensions. In the LDG method, besides the primary variable, the flux also appears as an unknown.

Because of the symmetric advantage of the stiffness matrix, SIPG is often applied to problems that do not have strict requirements on the stability. SIPG was also used by Hansbo and Larson [50] to solve 2-D nearly incompressible elasticity and Stokes flow problems. Recently, SIPG was extended by Sun and Wheeler [105, 107] to reactive transport problems by using the upwinding technique. Based on both IPG and OBB, a Non-symmetric Interior Penalty Galerkin (NIPG) formulation was presented by Riviere and Wheeler et al [89–91] for flow and elasticity problems. This formulation exhibits more stable and robust behavior than SIPG. Compared to OBB, NIPG allows one to adjust penalty parameters to achieve more accurate results.

A new scheme, the Incomplete Interior Penalty Galerkin (IIPG) method, was proposed by Dawson, Sun and Wheeler [34] to improve the performance of DG methods. IIPG has the best performance in terms of stability and accuracy of solutions for solving nearly incompressible elasticity problems as shown by Wheeler and Liu [119].

The advantages of DG methods over CG methods can be summarized as follows. First of all, the feature of local mass and momentum conservation is

very important to achieve a satisfactory flux or stress result for flow problems in the domains where the flow has large gradient and for elasticity problems with nearly incompressible materials. Second, DG allows hanging nodes. This is a really remarkable feature, which greatly facilitates the refinement on an original mesh in that each element can be refined or coarsened arbitrarily and independently, which could be a challenge for CG methods. Third, the ability of DG to handle problems with abrupt variations of solutions in the spatial or temporal domain. Fourth, DG is able to prevent a larger error occurring in a small area from propagating and polluting to the whole domain. This feature is particularly important to diffusion and /or convection-dominated problems. Finally, the high stability of DG schemes can be exploited to model a very unstable process like the last evolution stage of ideal plasticity problems.

1.3 Contributions

This section summarizes the main original research work of this dissertation on DG applied to modeling poromechanics problems.

• A nodal-based DG finite element code has been implemented and tested for three-dimensional linear elasticity problems. This program reads a similar input file to the one for traditional CG methods and then breaks the elements in some required domains into DG elements. The coupled use of DG and CG elements can be easily and naturally done in this code. Also, the Dirichlet boundary conditions can be enforced either weakly by treating boundary surfaces as interior faces or strongly by following the same procedure

as CG methods do. Various options for different DG schemes are implemented in this code.

• DG is proved to be a simple and robust candidate for solving three-dimensional nearly incompressible elasticity problems. DG is still a pure displacement-based method, which makes the implementation of computer code much easier than other complex alternatives like mixed finite elements. The first effort has also been invested in evaluating the performance of different DG schemes including SIPG, OBB, NIPG and IIPG for elasticity problems. This detailed evaluation is quite important to the selection on DG schemes for complex coupled systems of thermal, flow and solid problems.

• The first DG formulation for plasticity problems has been carried out. Besides the computational work on the Gaussian yielding points inside each element, the stiffness involving yielding points on interfaces across elements must be also computed. A technique has been proposed for obtaining stresses at an interface by extrapolating the stresses at the Gaussian points inside the element. This can help save memory and CPU time to store and compute the stress evolution on interfaces.

• A three-dimensional DG code has been implemented for solving elasto-plasticity problems. The code can handle the Von-Mises and Drucker-Prager materials with or without hardening behaviors. The nonlinear iteration schemes such as initial stiffness method, modified Newton-Raphson and Newton-Raphson method are implemented. It has been demonstrated that the feature of the high stability of DG schemes is particularly useful in modeling the whole plas-

tic evolution process for materials with ideal plasticity.

• Numerical examples have been presented to show that the popular CG scheme might not have any oscillatory solutions in solving those problems with small Biot's modulus, even when the permeability is very low in some domains. Particularly, this work also shows that the decay rate of the oscillation is independent of CG schemes.

• A weak formulation of DG methods has been derived for solving poroelasticity models. Discontinuous spaces are proposed for both displacement and pore pressure. A three-dimensional nodal-based DG code has been developed to verify the proposed DG formulation. The computer program is written in Fortran 90. Isoparametric elements with 8 , 20 and 27 nodes are used, which are particularly important to handling those problems with complex curved boundaries.

• The performance of DG for solving poroelasticity with very low permeability has been tested and compared with CG methods. These results show that DG is quite robust and powerful in avoiding any obvious nonphysical oscillation in the pressure solution and is particularly useful for modeling lacuna bone problems.

• DG has also been applied to the elasticity equation while the coupled flow equation is solved by the cell-centered finite difference method. A two-dimensional code has been implemented to verify this scheme. Numerical examples show that DG is powerful in avoiding oscillations. This scheme is

particularly useful in modeling oil reservoirs where the numerical schemes for solving flow problems are dominated by finite difference methods.

• A weak formulation using DG methods has been also derived for solving thermoporoelastoplasticity models. Discontinuous spaces are proposed for all three fields. The DG code for poroelasticity has been extended for this three-field problem by incorporating the plasticity code and by adding new code for the thermal equation. The nice performance of DG is again observed by the numerical examples taking into account thermal and plastic effects.

1.4 Outline of Dissertation

A thorough DG formulation on linear elasticity is derived and various DG schemes are tested in Chapter 2. Chapter 3 incorporates these DG schemes into plasticity models. Some new and special considerations on DG applied to plasticity are discussed in this chapter.

A large part of this work is focused on poroelasticity. A well-posed poroelasticity theory is reviewed and the stability analysis of CG for a general compressible model is carried out in Chapter 4. In Chapter 5, the framework of DG for elasticity is extended for poroelasticity by considering the effective stress and flow equation. Various numerical examples are presented and solved by both CG and DG methods. Chapter 6 proposes a new scheme for poroelasticity. DG is applied to elasticity equation but the flow equation is solved by a cell-centered finite difference method. A detailed formation on how the coupling stiffness is computed from both finite element spaces and finite difference

schemes is documented in this chapter.

Chapter 7 describes incorporating DG into thermoporoelastoplasticity. The convection is also included in the model. Well pumping and fluid injection are simulated by exploiting many features of DG methods.

The dissertation is finished by summarizing the results of this research work in Chapter 8 and future work and research directions are also discussed in this chapter.

Chapter 2

Modeling Linear Elasticity

2.1 Objective

In this chapter we will present a detailed DG formulation and implementation for linear elasticity problems. Numerical examples are presented and used to test the performance of a family of DG methods including OBB, SIPG, NIPG, and IIPG. This work will provide an important framework for further study of coupled fluid and solid problems to be solved by DG methods. It is also shown that DG can be a good alternative to other methods such as mixed finite element methods in dealing with nearly incompressible elasticity problems.

2.2 Mathematical Theory of Elasticity

Let a body occupy a domain $\Omega \in R^3$ shown in Figure 2.1. Ω has a boundary surface $\partial\Omega$ which is further divided into Γ_u and Γ_t with

$$\partial\Omega = \Gamma_u \cup \Gamma_t, \quad \Gamma_u \cap \Gamma_t = \emptyset \tag{2.1}$$

where the prescribed displacement $\bar{u}(x) \in H^1(\Gamma_u)$ is given on the part Γ_u of the boundary and the surface traction $\bar{t}(x) \in L^2(\Gamma_t)$ is given on the remainder Γ_t of the boundary. We denote the body force by $f(x) \in L^2(\Omega)$. To avoid

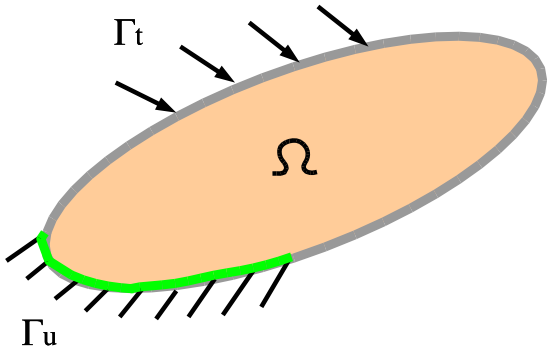

Figure 2.1: A Domain and Its Boundary

any confusion, we denote the Cauchy stress tensor σ'' for effective stress and σ for total stress. In Chapters 2 and 3, $\sigma \equiv \sigma''$ is implied as we only consider the case of pure solid or completely drained poromechanics. The variable u denotes the displacement field.

The linear momentum equation for three-dimensional linear elasticity is

$$\nabla \cdot \sigma + f = 0, \tag{2.2}$$

with the kinematic relation

$$\varepsilon = \frac{1}{2}(\nabla u + \nabla u^T), \tag{2.3}$$

and the elastic constitutive law

$$\sigma = D\varepsilon, \tag{2.4}$$

where D is the fourth order elasticity tensor with the following properties

$$\begin{gathered} D \in L^{\infty}(\Omega), \\ D_{ijkl} = D_{jikl} = D_{ijlk} = D_{klij}, \qquad (symmetry) \\ \varepsilon : D\varepsilon > 0 \qquad \forall \mid \varepsilon \mid \neq 0, \qquad (positive\ definite) \\ \varepsilon : D\varepsilon > \alpha \mid \varepsilon \mid^2 \qquad \alpha > 0, \qquad (pointwise\ stable) \end{gathered} \tag{2.5}$$

and ε is the strain tensor. The boundary conditions are:

$$\begin{gathered} u = \bar{u} \quad on\ \Gamma_u, \\ \sigma n = \bar{t} \quad on\ \Gamma_t, \end{gathered} \tag{2.6}$$

where n is the unit normal vector to the surface. The mathematical statement for linear elasticity problems is, find $u(x)$ such that:

$$\begin{gathered} \nabla \cdot (D(x)\nabla u(x)) + f(x) = 0 \qquad \forall\, x \in \Omega, \\ u(x) = \bar{u} \quad on\ \Gamma_u, \\ (D(x)\nabla u(x))n = \bar{t} \quad on\ \Gamma_t. \end{gathered} \tag{2.7}$$

2.3 DG Variational Formulation

We now establish key notations for DG methods. Let

$$\chi = \{E_1,\, E_2, \cdots,\, E_N\} \tag{2.8}$$

be a non-degenerate subdivision of domain $\Omega \in R^n$ where E_j is a triangle or quadrilateral if $n = 2$ or a tetrahedron or hexahedron if $n = 3$. Let $|s|$ be the

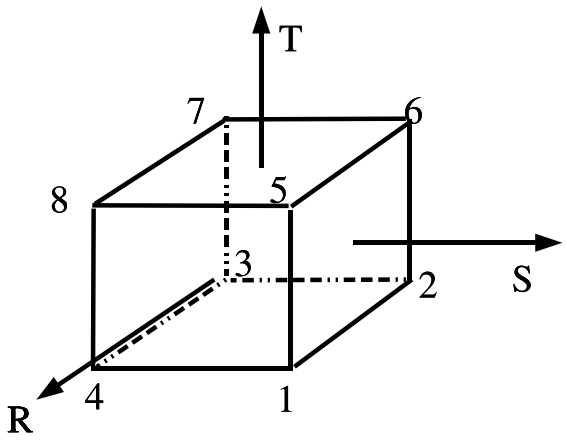

Figure 2.2: Local Faces

length of the ith edge for $n = 2$ or the square root of the area of the ith face for $n = 3$. Let $S = S_i + \Gamma_u + \Gamma_t$ be the set of faces of χ. S_i, Γ_D, and Γ_t indicate the interior faces, displacement boundary, and traction boundary. We define the following broken space

$$\begin{aligned} H^1(\chi) &= \{v \in L^2(\Omega) : v\mid_{E_j} \in H^1(E_j) \quad \forall E_j \in \chi\} \\ V &= \{v \in H^1(\chi),\ v = \bar{u}\ on\ \Gamma_u\}. \end{aligned} \tag{2.9}$$

We use Figure 2.2 to define negative (-) and positive (+) faces. In this figure R, S and T indicate local coordinates. Faces 1-5-8-4, 1-2-6-5, and 5-6-7-8 are defined to be positive. We assign numbers 1, 2, and 3 for these three positive faces, respectively. Faces 2-6-7-3, 3-7-8-4, and 1-2-3-4 are defined to be negative. We assign numbers 4, 5, and 6 for these three negative faces, respectively. For a given edge or face $s \in S$, we associate a unit normal vector

n^s and define jump and average values across s. More precisely, we define

$$[w] = w^+ - w^- \tag{2.10}$$

as the jump term on an interior face and

$$[w] = w^+ \tag{2.11}$$

the jump term on a boundary surface if its local face number is 1, 2, or 3. If a local boundary face number is 4, 5, or 6, we have the jump at this bounday surface below:

$$[w] = w^-. \tag{2.12}$$

We set

$$\{w\} = \frac{1}{2}(w^+ + w^-) \tag{2.13}$$

to be the average term on an interior face and

$$\{w\} = w^+ \tag{2.14}$$

the average term on the boundary surface if its local face number is 1, 2, or 3. If a local boundary face number is 4, 5, or 6, we have the average term at this bounday surface below:

$$[w] = w^-. \tag{2.15}$$

The finite element subspace consists of discontinuous piecewise polynomials:

$$D_r(\varepsilon) = \{v : \ v \mid_E \in (P_r(E))^n \ \forall \ E \in \chi\}. \tag{2.16}$$

We now define bilinear and linear forms. Let $E \in \chi$. Multiplying (2.2) by $v \in V$, and integrating by parts, we obtain

$$\int_E \sigma(u){:}\nabla v dV - \int_{\partial E} (\sigma n^s) \cdot v dS = \int_E f \cdot v dV. \tag{2.17}$$

Noting that $\sigma(u){:}\nabla v = \sigma(u){:}\nabla v^T = \sigma(u){:}\varepsilon(v)$, we have

$$\int_E \sigma(u){:}\varepsilon(v) dV - \int_{\partial E} (\sigma n^s) \cdot v dS = \int_E f \cdot v dV. \tag{2.18}$$

Then, summing over all elements χ, we obtain

$$\sum_{E\in\chi} \int_E \sigma(u){:}\varepsilon(v) dV - \sum_{\partial E \in S} \int_{\partial E} (\sigma n^s) \cdot v dS = \sum_{E\in\chi} \int_E f \cdot v dV. \tag{2.19}$$

Applying the definitions of average and jump terms defined in (2.10)-(2.15) and using the fact

$$[\phi\varphi] = \{\phi\}[\varphi] + [\phi]\{\varphi\}, \tag{2.20}$$

we have

$$\begin{aligned} &\textstyle\sum_{E\in\chi} \int_E \sigma(u){:}\varepsilon(v) dV - \sum_{\partial E \in S-\Gamma_t} \int_{\partial E} \{(\sigma(u) n^s)\} \cdot [v] dS \\ &= \textstyle\sum_{E\in\chi} \int_E f \cdot v dV + \int_{\Gamma_t} \bar{t} \cdot v dS. \end{aligned} \tag{2.21}$$

Adding face integrals $\int_{\partial E} \{(\sigma(v) n^s)\} \cdot [u] dS$ and $\frac{\delta}{|s|} \int_{\partial E} [u] \cdot [v] dS$ to 2.21, we have the bilinear and linear forms as follows

$$\begin{aligned} a(u,v) &= \textstyle\sum_{E\in\chi} \int_E \sigma(u){:}\varepsilon(v) dV - \sum_{\partial E \in S_i+\Gamma_u} \int_{\partial E} \{(\sigma(u) n^s)\} \cdot [v] dS \\ &+ \textstyle\sum_{\partial E \in S_i+\Gamma_u} \theta_{DG} \int_{\partial E} \{(\sigma(v) n^s)\} \cdot [u] dS + \sum_{\partial E \in S_i+\Gamma_u} \frac{\delta}{|s|} \int_{\partial E} [u] \cdot [v] dS \end{aligned} \tag{2.22}$$

and

$$\begin{aligned} L(v) &= \textstyle\sum_{E\in\chi} \int_E f \cdot v dV + \int_{\Gamma_t} \bar{t} \cdot v dS \\ &+ \textstyle\sum_{\partial E \in \Gamma_u} \theta_{DG} \int_{\partial E} (\sigma(v) n^s) \cdot \bar{u} dS + \sum_{\partial E \in \Gamma_u} \frac{\delta}{|s|} \int_{\partial E} \bar{u} \cdot v dS \end{aligned} \tag{2.23}$$

where δ is a penalty parameter chosen to be a function of r.

In (2.22) and (2.23), the DG method is referred to as SIPG if $\theta_{DG} = -1$, and NIPG if $\theta_{DG} = +1$, and OBB if $\theta_{DG} = +1$ and $\delta = 0$, and IIPG if $\theta_{DG} = 0$. It should be emphasized that the equilibrium is approximately satisfied weakly on each element in that

$$\int_{\partial E} \sigma(u) n^s dS + \int_E f dV = \sum_{\partial E} \frac{\delta}{|s|} \int_{\partial E} [u] dS. \tag{2.24}$$

The DG variational formulation can be stated:

find $u \in V$ such that:

$$a(u, v) = L(v) \qquad \forall v \in V. \tag{2.25}$$

2.4 DG Implementation

The popular CG finite element codes are nodal based. In general, a CG program uses geometric data containing the coordinates of nodes. The configuration of an element is defined by its nodes. These nodes completely determine the order of the element. Moreover, as the solutions are just the values at nodes, they can be directly used for output and visualization without any further post-processing. The nodal-based CG computer programs for linear elasticity have been thoroughly implemented, tested, and documented. For example, the shape functions are well established and can be easily found in the literature. Our idea on the design of DG programs for elasticity is

to fully exploit well tested CG programs. The main additional work for implementation of DG is to add some code to CG programs for computing the interface stiffness. We denote U as the node displacement vector, N as the interpolation matrix, B as the strain matrix. The displacement, strain, and stress fields can then be interpolated by U:

$$\begin{aligned} u &= NU \\ \varepsilon &= BU \\ \sigma &= DBU. \end{aligned} \tag{2.26}$$

Inserting (2.26) into (2.25), we obtain an algebraic system:

$$KU = F \tag{2.27}$$

where

$$\begin{aligned} K &= \textstyle\sum_E k_V^E + \sum_S k_S^S \\ k_V^E &= \textstyle\sum_{i=1}^{n_{gip}} [B_i, D_i] \\ k_S^S &= \textstyle\sum_{j=1}^{m_{gip}} [B_j^L, D_j^L, B_j^R, D_j^R, n^s] \\ F &= \textstyle\sum_{j=1}^{m_{gip}} [\bar{t}_j, N_j] \end{aligned} \tag{2.28}$$

where K is the global stiffness matrix, F is the load vector, k refers to the stiffness related to an element or a face, S indicates the face, E refers to the element, L and R means the left and right elements that share the face, and square brackets refers to functions.

In our computer code, we use 8 (trilinear), 20 and 27-node isoparametric hexahedral elements. These elements are shown in Figure 2.3. The red nodes in this figure indicate corner nodes. These isoparametric elements are particularly

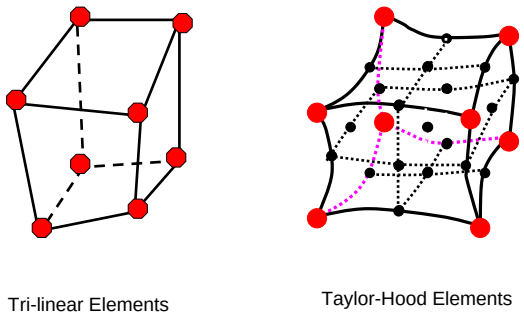

Figure 2.3: Isoparametric Hexahedral Elements; Corner Nodes in Red

useful in handling complex curved geometry. The procedures for 3-D DG programs are shown in Table 2.1. The key procedures for the code are as follows. It first reads an input file that is similar to the one for traditional CG programs and then another input file for information on breaking elements. The program then breaks some continuous elements into discontinuous ones, sets up resulting interfaces, and reorders nodes and elements. The element stiffness contributed from volume integration is first computed and assembled into the global stiffness matrix which is stored in a band format. Next, the interface stiffness is computed for each face by loading the information of the two elements which share the same face. After the stiffness is assembled for all interfaces, standard CG procedures are followed in enforcing boundary

conditions, computing the right-hand load vector, and using an LU direct solver to obtain displacement solutions.

It should be noted that the stresses at nodes directly computed by using the node displacements are not accurate and thus must be post-processed. We follow the post-processing procedure of traditional CG methods for stresses. The stresses at the Gaussian Integration Points (GIP) are first computed. The stresses at nodes are then extrapolated by using these interior stresses at GIP. As there are multiple values at each nodal point extrapolated from different elements in DG methods, we simply do the average on the multiple values for nodal stresses as we assume that the stress (flux) is continuous across the face. The post-processing is further illustrated in Figure 2.5.

2.5 Convergence Analysis

In general, the pure displacement-based CG methods work very well for linear elasticity problems with normal materials. However, their performance can be bad for cases where materials have Poisson's ratio close to 0.5. In these cases, CG gives a smaller displacement solution. This phenomena is called locking. The locking of CG and pure displacement methods for incompressible elasticity problems was proved by Babuska and Suri [6]. Let $L_{\lambda,h}$ defined by

$$L_{\lambda,h} := sup\{\frac{\left|u - u_h^{\lambda}\right|_{H^1(\Omega)}}{\|div\sigma_{\lambda}(u)\|_{L^2(\Omega)}} : \quad 0 \neq u \in H^2(\Omega) \cap H_0^1(\Omega)\} \tag{2.29}$$

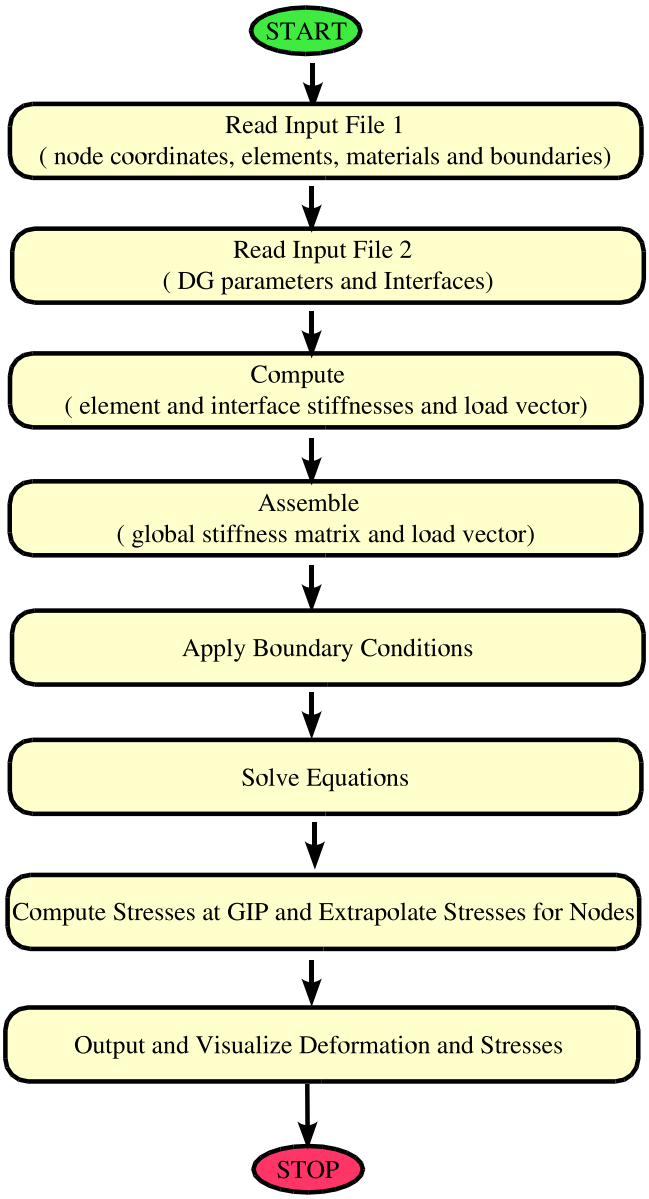

Figure 2.4: Procedures of DG Program for Elasticity

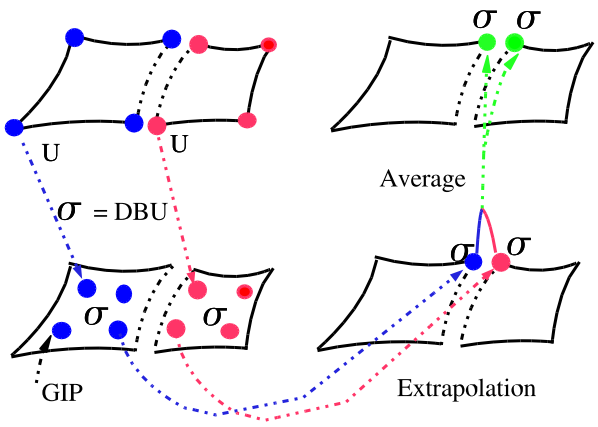

Figure 2.5: Nodal Stresses Extrapolated by Stresses at Interior GIP

then they proved that there exists a positive constant C independent of h such that

$$lim_{\lambda\to\infty} inf\ L_{\lambda,h} \geq C \tag{2.30}$$

where λ is the Lame's constant. This means that no matter how small h is, if λ is large enough, then we can find $u \in H^2(\Omega) \cap H_0^1(\Omega)$ such that the relative error $\left|u - u_h^\lambda\right|_{H^1(\Omega)} / \left\|div\sigma_\lambda(u)\right\|_{L^2(\Omega)}$ is bounded below by a constant independent of h. In other words, the performance of the CG and pure displacement methods will deteriorate for large λ.

Methods for handling locking include mixed finite element methods, reduced integration, nonconforming methods, and stabilized finite elements [50]. The locking may be completely removed by mixed finite element methods. However, the selection of the spaces for displacement and pressure may

not be independent. Also, much more effort is required for program implementation and users must be experts on the advanced finite element theories. A severe under-integration is needed for the reduced integration method to work, which greatly reduces the accuracy. The coercivity of the discrete operator must be ensured for nonconforming methods to obtain a stable solution. Stabilized finite element methods require determination of an appropriate stabilized parameter. Because DG is locking-free and also simple in its program implementation, we propose DG for solving nearly incompressible elasticity.

Optimal rates of convergence in the energy norm for NIPG applied to elasticity problems were derived by Riviere and Wheeler [89, 90]. They proved that the convergence of NIPG is independent of Poison's ratio. The locking-free property of SIPG for nearly incompressible elasticity was proved by Hansbo and Larson [50] and by Wihler [120] for NIPG for simplicial elements. Their results can be summarized by

$$\left\|u - U^{DG}\right\| \leq Ch^k(\|f\|_{H^{k-1}(\Omega)} + \|u_D\|_{H^{k-1}(\partial\Omega_D)} + \|t\|_{H^{k-1/2}(\partial\Omega_N)}) \qquad (2.31)$$

where C is independent of h and λ. Clearly, this means that if λ is large, the performance of the DG methods will not deteriorate. The DG methods are locking-free.

2.6 A Bracket in Bending

In this section we consider a three-dimensional version of a bracket problem used in [8] as a benchmark in comparing four DG formulations and

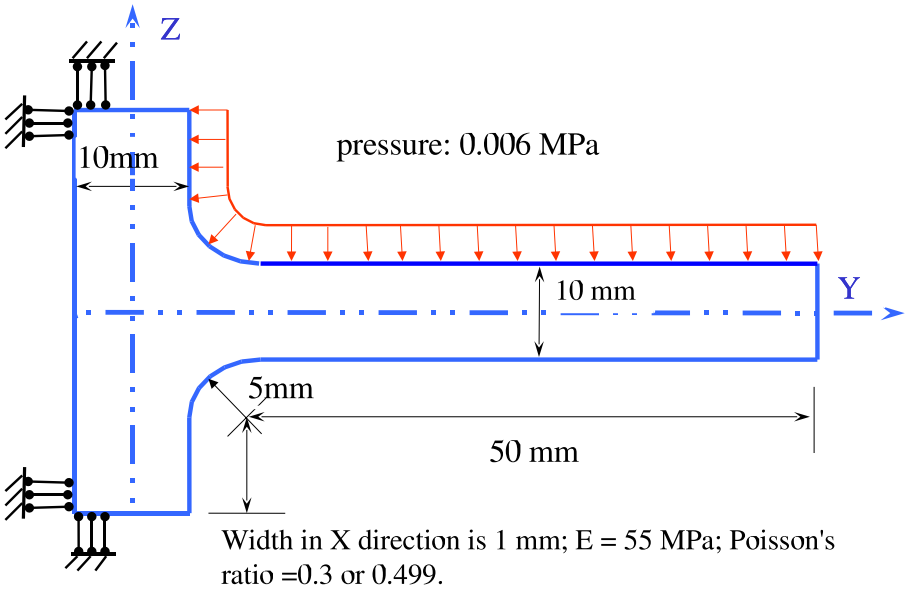

Figure 2.6: A Bracket Problem

a continuous Galerkin method. This problem is shown in Figure 2.6. The bracket in Figure 2.6 is fixed at the left corners and is loaded by a uniform pressure on the top surface. We study two cases, Poisson's ratio $\nu = 0.3$ and $\nu = 0.499$.

This problem has been solved by using four DG formulations given above. In all of our calculations we used 170 isoparametric trilinear hexahedral

elements. The configuration of the mesh in the $y-z$ plane can be found in Figure 2.7. As this problem is assumed to be plane strain, all the freedoms in the x direction are fixed.

Obviously, a strict analytical solution for this problem is unavailable due to the complexity of the geometry of the bracket. However, an approximated solution based on the elementary beam theory does exist. Based on the plane strain theory of elasticity problems, the two cases with Poisson's ratio 0.3 and 0.499 should have a very close stress solution. As CG and pure displacement finite element methods work very well for the case of Poisson's ratio 0.3, we can obtain a more accurate stress solution using CG with a very fine mesh or with higher-order elements. A reliable and accurate solution based on Poison's ratio 0.3 and CG methods with a 170-element mesh (27-node elements) was obtained below

$$\begin{aligned} \sigma_y &= 0.60\, Mpa \\ \delta_{tip} &= 1.60\, mm \end{aligned} \tag{2.32}$$

where σ_y is the maximum stress in the y-direction and δ_{tip} is the vertical displacement at the tip. These values can be used for validating DG methods.

Figure 2.7 shows the contours of tensile stresses in the $y-$direction above $0.15\, Mpa$ for CG approximation. In particular in Figure 2.7(a) and Figure 2.7(b), we note results obtained with Poisson's ratios of 0.3 and 0.499, respectively. These results demonstrate that the CG method works very well for compressible materials but is oscillatory for nearly incompressible materials. The tip displacement is $1.12\, mm$ for the case of the Poisson's ratio 0.499,

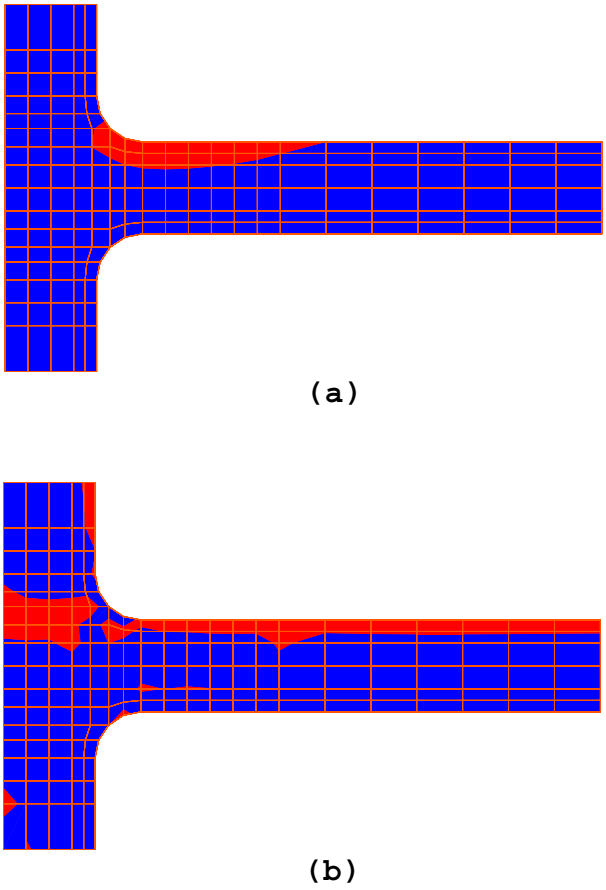

Figure 2.7: Tensile Stress Contours ($\sigma_y > 0.15\,Mpa$) of CG Solutions of Bracket Problem. (a) Poisson Ratio = 0.3; $(\sigma_y)_{max} = 0.51\,Mpa$; Tip Deflection = 1.61 mm. (b) Poisson Ratio = 0.499; $(\sigma_y)_{max} = 0.86\,Mpa$; Tip Deflection = 1.12 mm.

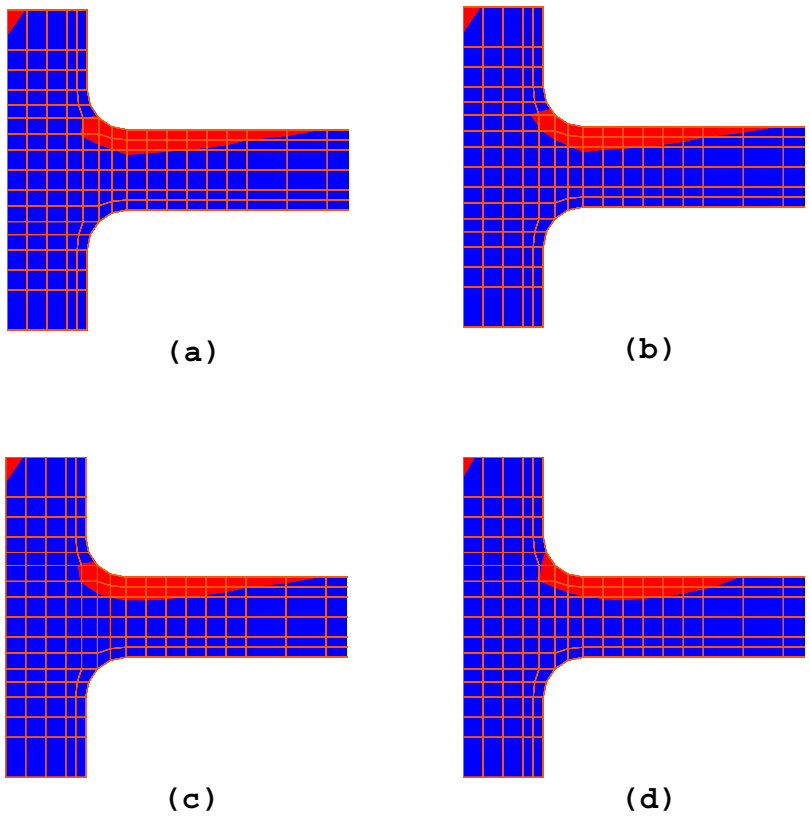

Figure 2.8: Tensile Stress Contours ($\sigma_y > 0.15\,Mpa$) of DG Solutions of Bracket Problem with Poisson's Ratio 0.499. (a) OBB; $(\sigma_y)_{max} = 0.75\,Mpa$; Tip Deflection = 1.62 mm. (b) NIPG; $(\sigma_y)_{max} = 0.68\,Mpa$; Tip Deflection = 1.62 mm. (c) SIPG; $(\sigma_y)_{max} = 0.55\,Mpa$; Tip Deflection = 1.62 mm. (d) IIPG; $(\sigma_y)_{max} = 0.59\,Mpa$; Tip Deflection = 1.62 mm.

which is much smaller than the accurate value of $1.60\,mm$. Also, the shape of the tension zone above $0.15\,Mpa$ predicted by the CG method for the case of the Poisson's ratio 0.499 is unacceptable.

In Figure 2.8 we present the tensile stress contours resulting from four DG formulations applied to the above nearly incompressible case. In particular Figure 2.8(a) shows that the OBB method predicts the shape of tension zone very well. Also, the OBB solutions in displacement and maximum stress are greatly improved over the CG method. Similar improvements in solutions are also found in the SIPG, NIPG, and IIPG methods, which are shown in Figure 2.8(b), (c), and (d). However, NIPG gives a better prediction on the maximum stress than OBB. Another very important observation is that the solution of IIPG is closest to the accurate one. It should be mentioned that the solution of SIPG is very sensitive to the values of the penalty parameter. Also, IIPG has a large range of variation of the penalty parameter. For normal materials all four DG methods work very well and don't have any obvious difference in performance. However, from a programing point of view OBB is the simplest one to implement, and SIPG has a nice matrix structure.

2.7 A Breast Reconstruction Model

The surgery on treating breast cancer often results in a complete removal of all breast tissue. The reconstructive surgery rebuilds the breast mound by using either natural or artificial materials. A successful breast reconstruction depends on many factors such as the surgeon's experience, the

preference of the patient, and the patient's physical conditions. A computer-assisted system that is able to simulate the deformation and predict the shape of assumed reconstruction models will greatly facilitate the operation of the surgeon.

Current research work in biomedical engineering is in making a framework for a breast reconstruction simulator. The first fundamental work for this framework is to establish reliable constitutive models of breast tissues, which are particularly important to improving the accuracy of the models. Breast tissues can be assumed to be isotropic, homogeneous, and incompressible or nearly incompressible. Based on these assumptions, the mechanical behavior of breast tissues can be well defined by a single parameter, Young's modulus E, which is a function of strain ε:

$$E = \frac{d\sigma}{d\varepsilon} = f(\varepsilon) \tag{2.33}$$

where σ is the nominal stress. In general, the function f is of a nonlinear hyperelastic behavior. The function for human breast tissues can be found in [5, 41] as follows:

$$E = \frac{d\sigma}{d\varepsilon} = be^{m\varepsilon} \tag{2.34}$$

where b and m are constants obtained from experimental data. For glandular tissue $b = 15100\,Pa,\ m = 10.0$, and for fatty tissue $b = 4460\,Pa,\ m = 7.4$. The typical Young's modulus for skin is $3.43 \times 10^6\ Pa$ for $\varepsilon \leq 0.54$, $2.89 \times 10^7\ Pa$ for $0.54 < \varepsilon \leq 0.68$, and $1.57 \times 10^8\ Pa$ for $\varepsilon > 0.68$. These nonlinear material properties have been used in a few breast models [121].

In the literature [5, 121], a 2-D membrane model was developed for an initial study to gain an intuition of the constraints and initial conditions of the shape deformation. A 3-D surface model and a 3-D solid finite element model were created using realistic breast geometries obtained by scanning image data. However, there is still a great challenge in developing numerical models to accurately predict the deformation and shape of this soft tissue.

Instead of studying complex models, we use a simple breast reconstruction model to demonstrate the potential for DG applied to solving soft tissue problems. The motivation is that most soft tissues are nearly incompressible, which brings a challenge to most popular commercial software packages. Here, we emphasize that DG is locking-free and still a pure displacement-based method, which might be a good candidate for solving soft tissues with large deformation and highly nonlinearity. A 2-D plane strain model shown in Figure 2.9 is used for the initial study of breast reconstruction. We want to predict the deformation and the shape profile under gravity loading. The following assumptions are made:

•Linear Elasticity;

•Nearly Incompressible; and

•Large Deformation.

Fatty tissue is assumed for the material and the Poisson ratio is set up to 0.499. The left wall is fixed. A rough value of the maximum tensile stress in the y-direction evaluated by elementary beam theory is about

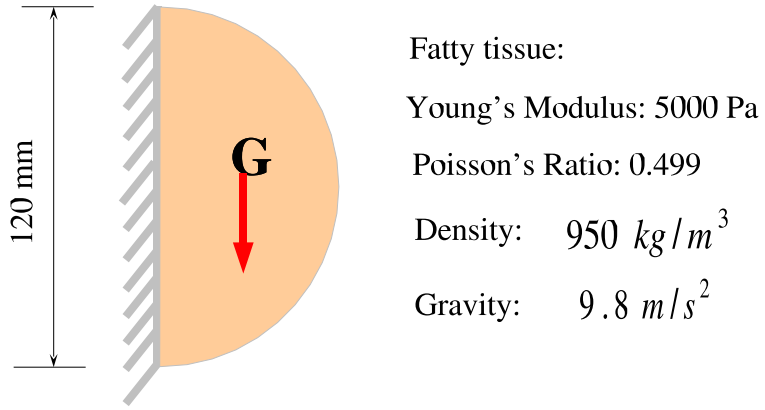

Figure 2.9: A Breast Reconstructive Model Under Gravity Loading

500 Pa. The total gravity loading is divided by 50 steps. In each step, the element geometry is updated by adding the increments of node displacements into their corresponding coordinates. The Cauchy infinitesimal small strain tensor and superposition are used. Figure 2.10 shows the evolution process of the deformation and shape of the breast predicted by the CG finite element simulation.

The normal tensile stress in y-direction is contoured in red. The shape of the lowest element near the fixed wall clearly indicates locking in deformation. What we expect in the stress prediction is that the upper part is in tension and the lower part is in compression. The maximum tensile stress in the y-direction predicted by CG is 1349 Pa. This prediction on stresses is unacceptable. The maximum displacement in the vertical direction predicted

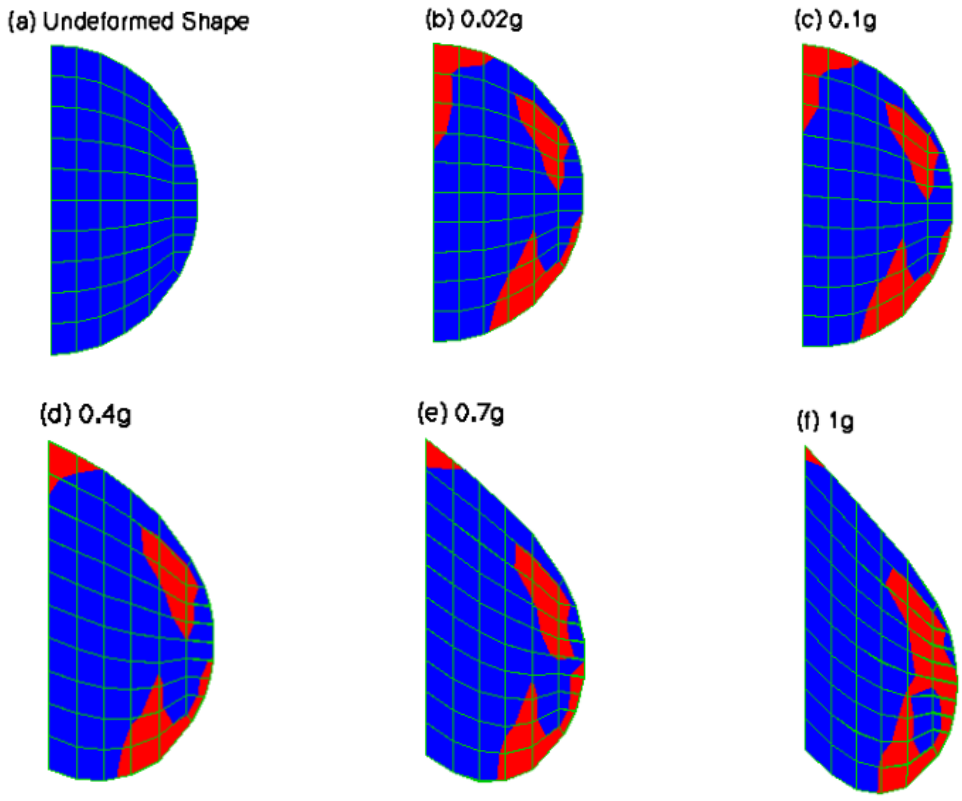

Figure 2.10: Evolution Progress of Deformation and Stress of Reconstructed Breast under Gravity Loading Predicted by CG Method: Tensile Stress in Horizontal Direction Is Contoured in Red Color; $(\sigma_y)_{max} = 1349\,Pa$, $(u_z)_{max} = -34\,mm$.

by CG is $0.34\,mm$. Again, the good performance of DG (IIPG) for this problem is obtained and shown in Figure 2.11. The maximum tensile stress in the y-direction predicted by DG is $484\,Pa$. The maximum displacement in the vertical direction predicted by DG is $0.38\,mm$. Figure 2.12 presents the updating of the geometry following the gravity loading steps.

Some comments have to be addressed here. First, a strict and correct procedure for modeling any finite deformation requires using the Second Piola-Kirchhoff stress tensor and Total Lagrangian or Updated Lagrangian formulation. This is out of the scope of this dissertation but can be found in [8, 76]. Second and obviously, linear elasticity may not be true for soft tissues especially in the large deformation stages. Finally, we remark that any Lagrangian formulation for finite deformation based on pure displacement-based method cannot avoid locking for nearly incompressible materials either. Therefore, DG is potentially a good candidate for modeling soft tissues if we consider that it is a pure displacement-based method and locking free.

2.8 Summary

We have presented a family of DG formulations for elasticity as well as numerical examples that indicate that DG can be applied to nearly incompressible problems. Thus, DG offers an alternative to the mixed or stabilized formulations for treating incompressible elasticity. All four DG methods predict accurate stresses. The non-symmetric formulations such as OBB, NIPG and IIPG apprear to be more robust than the symmetric formulations such as

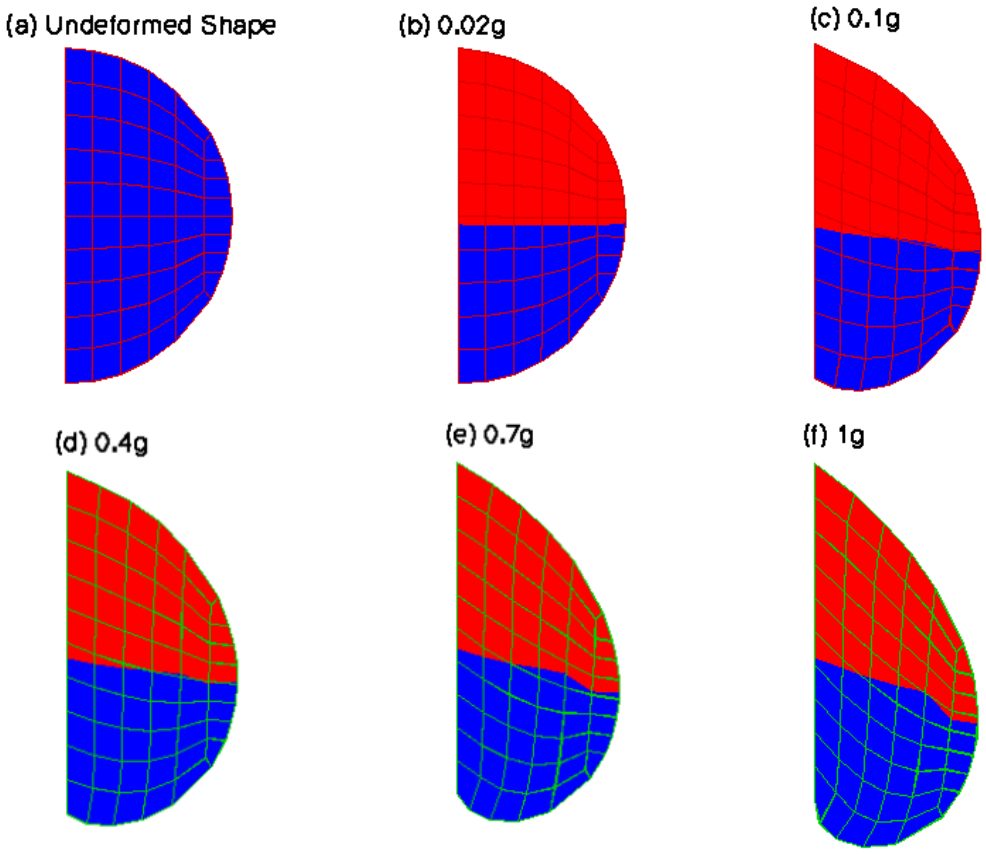

Figure 2.11: Evolution Progress of Deformation and Stress of Reconstructed Breast under Gravity Loading Predicted by DG Method: Tensile Stress in Horizontal Direction Is Contoured in Red Color; $(\sigma_y)_{max} = 484\,Pa$, $(u_z)_{max} = -37\,mm$.

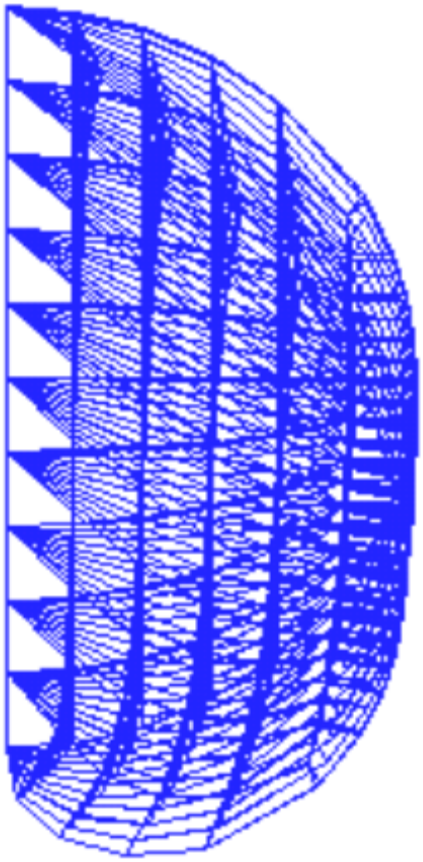

Figure 2.12: Geometry Updating of Reconstructed Breast under Gravity Loading (DG).

SIPG. This study of DG on elasticity is important to modeling the coupling problems of fluid and mechanics, which we will address in Chapter 4.

Chapter 3

Modeling Plasticity

3.1 Objective

Plasticity theory has many important applications. For example, well stability, well failure, and solid production in oil reservoir engineering can be modeled by using rock plasticity theory. In this chapter we incorporate DG theory into plasticity problems. First, we briefly review the fundamentals of plasticity theory and summarize general numerical schemes and procedures for solving plasticity. For more detailed plasticity theory, we refer to Hill [51, 52], Kachanov [60], Lubliner [65], Maugin [69], Green and Naghdi [46]. For more detailed numerical schemes, we refer to Simo and Hughes [101] and Han and Reddy [49]. Second, we present DG formulation for plasticity problems. An extrapolation scheme for obtaining stresses on faces by using interior stresses is proposed. Finally, we present a numerical example to validate the DG formulation and program. We will present numerical examples for Drucker and Prager's model in Chapter 7 where DG methods are proposed for thermo-poroelastoplasticty problems.

3.2 Theory of Plasticity

3.2.1 Governing Equations

Again, let a body occupy a domain $\Omega \in R^3$. Ω has a boundary surface $\partial\Omega$ which is divided into Γ_u and Γ_t with

$$\partial\Omega = \Gamma_u \cup \Gamma_t, \quad \Gamma_u \cap \Gamma_t = \emptyset, \tag{3.1}$$

where the prescribed displacement $\bar{u}(x) \in H^1(\Gamma_u)$ is given on the part Γ_u of the boundary and the surface traction $\bar{t}(x) \in L^2(\Gamma_t)$ is prescribed on the remainder Γ_t. We denote body force by $f(x) \in L^2(\Omega)$. The first function we want to define is a yield function:

$$Y : \ L \times R \to R, \tag{3.2}$$

where L is a tensor space. A constrained admissible state is:

$$\{\sigma, \vartheta\} \in L \times R, \tag{3.3}$$

where σ is the Cauchy stress tensor and ϑ is a hardening parameter. A corresponding set E_σ for elastic and plastic states is defined below:

$$E_\sigma := \{(\sigma, \vartheta) \in L \times R \ \mid \ Y(\sigma, \vartheta) \leq 0\} = E_\sigma^I \cup E_\sigma^B. \tag{3.4}$$

The interior of E_σ:

$$E_\sigma^I := \{(\sigma, \vartheta) \in L \times R \ \mid \ Y(\sigma, \vartheta) < 0\}, \tag{3.5}$$

is an admissible stress space in an elastic state; the boundary of E_σ:

$$E_\sigma^B := \{(\sigma, \vartheta) \in L \times R \ \mid \ Y(\sigma, \vartheta) = 0\}, \tag{3.6}$$

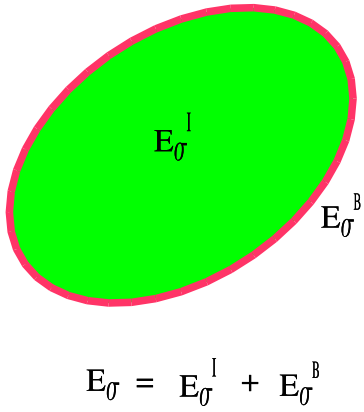

Figure 3.1: Admissible Stress Space and Set

is a stress space in plastic state and is referred as the yield surface. E_σ^B is also called the yield surface.

The second function F we introduce is called the flow function and is defined by:

$$F(\sigma, \vartheta) : L \times \mathcal{R} \rightarrow \mathcal{R}, \forall (\sigma, \vartheta) \in E_\sigma^B. \tag{3.7}$$

The convexity property of yield and flow functions is assumed here. The linear momentum equation for three-dimensional elastoplasticity is

$$\nabla \cdot \sigma(u) + f = 0 \tag{3.8}$$

with kinematic relation

$$\varepsilon = \frac{1}{2}(\nabla u + \nabla u^T). \tag{3.9}$$

We do strain decomposition as follows

$$\varepsilon(u) = \varepsilon^e(u) + \varepsilon^p(u), \tag{3.10}$$

where ε^e and ε^p are the total elastic and plastic strains, respectively. The elastic constitutive law is

$$\sigma(u) = D\varepsilon^e(u) = D(\varepsilon(u) - \varepsilon^p(u)) \tag{3.11}$$

where D is the fourth order elasticity tensor with properties already specified in (2.5) in Chapter 2. The evolutionary (rate of change) plastic strain is given by

$$\dot{\varepsilon}^p(u) = \dot{\gamma}(\sigma(u), \vartheta(\varepsilon^p(u)))\frac{\partial F(\sigma(u), \vartheta(\varepsilon^p(u))}{\partial \sigma(u)} \quad \forall\, (\sigma, \vartheta) \in E_\sigma^B \tag{3.12}$$

where F is the flow function or potential, ϑ is the hardening parameter, and $\dot{\gamma}$ is a nonnegative scalar function, dependent on $\sigma(u)$ and $\vartheta(\varepsilon^p(u))$, called the consistency parameter, which satisfies

$$\begin{cases} \dot{\gamma} = 0 \qquad \forall\, (\sigma, \vartheta) \in E_\sigma^I \;\; (elastic\ state) \\ \\ \dot{\gamma} > 0 \qquad \forall\, (\sigma, \vartheta) \in E_\sigma^B \;\; (plastic\ state). \end{cases} \tag{3.13}$$

The elastic and plastic states are determined by the yield function Y:

$$\begin{cases} Y(\sigma(u), \vartheta(\varepsilon^p(u)) < 0 \qquad \forall\, (\sigma, \vartheta) \in E_\sigma^I \;\; (elastic\ state) \\ \\ Y(\sigma(u), \vartheta(\varepsilon^p(u)) = 0 \qquad \forall\, (\sigma, \vartheta) \in E_\sigma^B \;\; (plastic\ state) \end{cases} . \tag{3.14}$$

The consistency condition satisfies

$$\dot{Y}(\sigma, \vartheta) = 0 \quad \forall (\sigma, \vartheta) \in E_\sigma^B. \tag{3.15}$$

We now have three unknowns from displacement vector u, six unknowns from strain tensor ε, six unknowns from plastic strain ε^p, and six unknowns from stress tensor σ. Total unknowns are twenty-one. Number of equations are:

three linear momentum equations given in by (3.8), six kinematic equations given by (3.9), six from strain decomposition given in (3.10), six from elastic constitutive law regulated by (3.11), and six from the flow rule deduced by (3.12). We now assume for plasticity problems the following boundary conditions:

$$u = \bar{u} \quad on\ \Gamma_u \tag{3.16}$$

$$\sigma n = \bar{t} \quad on\ \Gamma_t. \tag{3.17}$$

An analysis of uniqueness and stability for plasticity problems was performed by [52].

3.2.2 Plastic Behavior

There are a few important terminologies and conditions in plasticity theory. The first one is so called the non-associated plasticity model. In general, the flow function F is not necessarily the same as the yield function Y in a model. If $F \neq Y$, we have a non-associated plasticity model. It is referred to as the associated plasticity model if we use the yield function as the flow function. The use of an associated model leads to a symmetric formulation whereas a non-associated model results in a non-symmetric stiffness matrix. In other words, a non-associated model results in a more complex numerical problem.

In ideal plasticity, yielding materials flow without any increase in stresses. Most materials exhibit some degree of hardening associated with plastic strain. This means that the shape and size of the yielding surface is dynamically

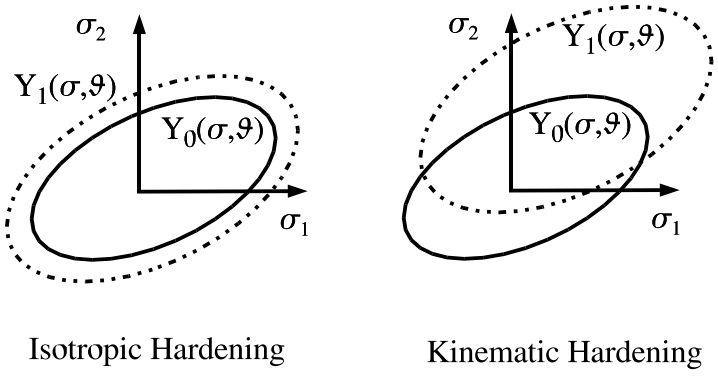

Figure 3.2: Material Hardening

changing with increase in total plastic strain. Two types of idealized hardening are isotropic hardening and kinematic hardening which are illustrated in Figure 3.2 [51]. For isotropic hardening, the initial yielding surface undergoes a homogeneous expansion. Kinematic hardening involves a translation of the initial yield surface. The hardening effect on the yield function $Y(\sigma, \vartheta)$ is most often taken into account by the scalar parameter ϑ.

At any evolutionary state, any point is in either an elastic or a plastic state which can be determined by the Kuhn-Tucker complementarity conditions:

$$\begin{cases} \dot{\gamma} \geq 0,\ Y(\sigma,\vartheta) \leq 0\ and \\ \dot{\gamma} Y(\sigma,\vartheta) = 0, \quad \forall\,(\sigma,\vartheta) \in E_\sigma \end{cases}. \tag{3.18}$$

In addition, the consistency condition (3.15) can be rewritten by:

$$\dot{\gamma}\dot{Y}(\sigma,\vartheta) = 0, \quad \forall\,(\sigma,\vartheta) \in E_\sigma. \tag{3.19}$$

These conditions imply the following loading and unloading cases [101]:

$$\begin{cases} Y<0 \;\Leftrightarrow\; (\sigma,\vartheta)\in E_\sigma^I \;\Rightarrow\quad \dot\gamma=0 \quad\Rightarrow\quad \textit{Elastic State} \\ \\ Y=0 \;\Leftrightarrow\; (\sigma,\vartheta)\in E_\sigma^B \begin{cases} \dot Y<0\Rightarrow\dot\gamma=0\Rightarrow \textit{Elastic Unloading State} \\ \\ \dot Y=0\Rightarrow\dot\gamma=0\Rightarrow \textit{Neutral Loading State} \\ \\ \dot Y=0\Rightarrow\dot\gamma>0\Rightarrow \textit{Plastic Loading State} \end{cases} \end{cases}. \tag{3.20}$$

3.2.3 Evolutionary Modulus

The elastic constitutive equation in (3.11) can be rewritten in an evolutionary form that is particularly useful in deriving numerical formulations. In addition, the consistency parameter $\dot\gamma$ is an unknown function but can be explicitly expressed in terms of the yield function, flow function, and their derivatives [51, 101]. Differentiating the second condition in (3.14) we obtain the consistency condition:

$$\dot Y=\frac{\partial Y}{\partial\sigma}:d\sigma+\frac{\partial Y}{\partial\vartheta}\frac{\partial\vartheta}{\partial\varepsilon^p}:d\varepsilon^p=0,\forall(\sigma,\vartheta)\in E_\sigma^B, \tag{3.21}$$

where ":" denotes the inner product operator of two tensors. Inserting (3.12) into (3.21), we obtain:

$$\frac{\partial Y}{\partial\sigma}:d\sigma=-\dot\gamma\frac{\partial Y}{\partial\vartheta}\frac{\partial\vartheta}{\partial\varepsilon^p}:\frac{\partial F}{\partial\sigma}. \tag{3.22}$$

The additive decomposition of strain tensor can be rewritten as an evolutionary form by differentiating (3.10) and inserting (3.12):

$$\dot\varepsilon=\dot\varepsilon^e+\dot\varepsilon^p=D^{-1}d\sigma+\dot\gamma\frac{\partial F}{\partial\sigma}. \tag{3.23}$$

Multiplying (3.23) by the elasticity tensor D and performing an inner product with $\frac{\partial Y}{\partial \sigma}$, we have:

$$\frac{\partial Y}{\partial \sigma} : D\dot{\varepsilon} = \frac{\partial Y}{\partial \sigma} : d\sigma + \dot{\gamma}\frac{\partial Y}{\partial \sigma} : D\frac{\partial F}{\partial \sigma}. \tag{3.24}$$

Using (3.22), the consistency parameter can be obtained from (3.24) as follows:

$$\dot{\gamma} = \frac{\frac{\partial Y}{\partial \sigma} : D\dot{\varepsilon}}{\frac{\partial Y}{\partial \sigma} : D\frac{\partial F}{\partial \sigma} - \frac{\partial Y}{\partial \vartheta}\frac{\partial \vartheta}{\partial \varepsilon^p} : \frac{\partial F}{\partial \sigma}}. \tag{3.25}$$

Equation (3.23) can be rewritten as follows:

$$D\dot{\varepsilon} = d\sigma + \dot{\gamma}D\frac{\partial F}{\partial \sigma} = \dot{\sigma} + \dot{\gamma}D\frac{\partial F}{\partial \sigma}. \tag{3.26}$$

Finally, we obtain an evolutionary constitutive relationship by inserting (3.25) into (3.26):

$$\dot{\sigma} = \{D - \frac{D\frac{\partial F}{\partial \sigma} \otimes D\frac{\partial Y}{\partial \sigma}}{\frac{\partial Y}{\partial \sigma} : D\frac{\partial F}{\partial \sigma} - \frac{\partial Y}{\partial \vartheta}\frac{\partial \vartheta}{\partial \varepsilon^p} : \frac{\partial F}{\partial \sigma}}\}\dot{\varepsilon}. \tag{3.27}$$

Considering both elastic and plastic states, we may write the evolutionary constitutive relationship in a general form:

$$\dot{\sigma} = D^{ep}\dot{\varepsilon} \quad \forall\, (\sigma, \vartheta) \in E_\sigma, \tag{3.28}$$

where D^{ep} is called evolutionary elastoplastic tensor and is defined by:

$$D^{ep} = \begin{cases} D & \forall\, (\sigma, \vartheta) \in E_\sigma^I \quad (elastic\ state) \\ D - \frac{D\frac{\partial F}{\partial \sigma} \otimes D\frac{\partial Y}{\partial \sigma}}{\frac{\partial Y}{\partial \sigma} : D\frac{\partial F}{\partial \sigma} - \frac{\partial Y}{\partial \vartheta}\frac{\partial \vartheta}{\partial \varepsilon^p} : \frac{\partial F}{\partial \sigma}} & \forall\, (\sigma, \vartheta) \in E_\sigma^B \quad (plastic\ state) \end{cases}.$$

where "$\otimes$" denotes tensor product. For a plastic state, the elastoplastic tensor is symmetric if an associated model ($F = Y$) is used but nonsymmetric if a non-associated model ($F \neq Y$) is assumed. In addition, the elastoplastic tensor will be zero if a material point with ideal plasticity goes yielding [51].

3.2.4 Material Models

Yield and flow functions must be established according to a criterion that will not violate the material difference law in continuous mechanics [48]. This law states that a scalar yield or flow function does not change if the coordinate system is rotated or a new coordinate system is introduced. This implies that yield and flow laws are functions of the invariants of stress and/or the plastic strain tensor. More precisely, these functions should have the following form:

$$Y(\sigma, \vartheta) \equiv Y(\sigma_1, \sigma_2, \sigma_3, \varepsilon_1^p, \varepsilon_2^p, \varepsilon_3^p) \equiv Y(I_1, I_2, I_3, I_1^p, I_2^p, I_3^p) \tag{3.29}$$

or in some models

$$Y(\sigma, \vartheta) = Y(J_2, J_3, I_1^p, I_2^p, I_3^p) \tag{3.30}$$

where σ_i, ε_i^p, I_i, I_i^p, and J_i with $i = 1, 2,$ *and* 3 are the principal stresses of stress tensor σ, the principal plastic strains of plastic strain tensor ε^p, the invariants of stress tensor σ, the invariants of plastic strain tensor ε^p, and the invariants of deviatoric stress tensor S. The deviatoric stress tensor σ is defined by :

$$S = \sigma - \frac{1}{3} I_1 I, \tag{3.31}$$

where I is the identity tensor and the invariants of σ, and S are defined as follows [48]:

$$I_1 = tr(\sigma),$$

$$I_2 = \sigma : \sigma,$$

$$I_3 = det(\sigma),$$

$$J_1 = 0,$$

$$J_2 = \tfrac{1}{2} S : S,$$

$$J_3 = det(S).$$

The Tresca model [51] assumes that yielding occurs when the maximum shear stress reaches a critical value:

$$Y = max\,(\frac{1}{2} \mid \sigma_1 - \sigma_2 \mid, \frac{1}{2} \mid \sigma_1 - \sigma_3 \mid, \frac{1}{2} \mid \sigma_2 - \sigma_3 \mid) - \sigma_0,$$

where σ_0 is a constant or a function of volume plastic strain I_1^p (for Drucker-Prager's model). It should be noticed that the surface of Tresca's yield function is not smooth and has six corners. Mises [51] proposed a smooth yield function that considers all three shear stresses:

$$Y = \sqrt{J_2} - \sigma_0 \tag{3.32}$$

Tresca and von Mises theories are often applied to modeling metal plasticity problems. These models imply that no matter how large the hydrostatic pressure is, it will not affect the yielding of materials. However, this is not true for soil and rock materials. The Drucker-Prager model [58] was established for soils and rocks by adding a mean stress term into von Mises's yield function.

Also, the corresponding flow function was derived in a similar fashion. This model has the yield function

$$Y = \sqrt{J_2} - \alpha_Y I_1 - \sigma_Y \tag{3.33}$$

and flow function

$$F = \sqrt{J_2} - \alpha_F I_1 - \sigma_F, \tag{3.34}$$

where

$$\begin{aligned} \alpha_Y &= -\tfrac{2\sin\phi_1}{\sqrt{3}(3-\sin\phi_1)}, \\ \sigma_Y &= \tfrac{6c\cos\phi_1}{\sqrt{3}(3-\sin\phi_1)}, \\ \alpha_F &= -\tfrac{2\sin\phi_2}{\sqrt{3}(3-\sin\phi_2)}, \\ \sigma_F &= \tfrac{6c\cos\phi_2}{\sqrt{3}(3-\sin\phi_2)}. \end{aligned} \tag{3.35}$$

A standard sign convention is that compressive stresses are negative. In (3.35), ϕ_1 and ϕ_2 are friction angles. The parameter c is the cohesion. Figure 3.3 shows the shape of this model in 3-D, which is, more precisely, called Drucker-Prager's model without cap.

To make Drucker-Prager's model more practical, a cap was added in order to close the opened cone [87], which is shown in Figure 3.4. The yield function for the cap portion can be designed by satisfying an elliptic equation [97]:

$$\begin{aligned} Y_{cap} &= \tfrac{(I_1-X-a)^2+R^2J_2}{a^2} - 1, \\ a &= \alpha_Y\sigma_Y R^2 + \alpha_Y^2 R^2 X + \sqrt{R^2(\alpha_Y X+\sigma_Y)^2(1+\alpha_Y^2R^2)}, \\ I_{1-transition} &= \tfrac{X+a-\sigma_Y R^2 J_2}{1+\alpha_Y^2R^2}. \end{aligned} \tag{3.36}$$

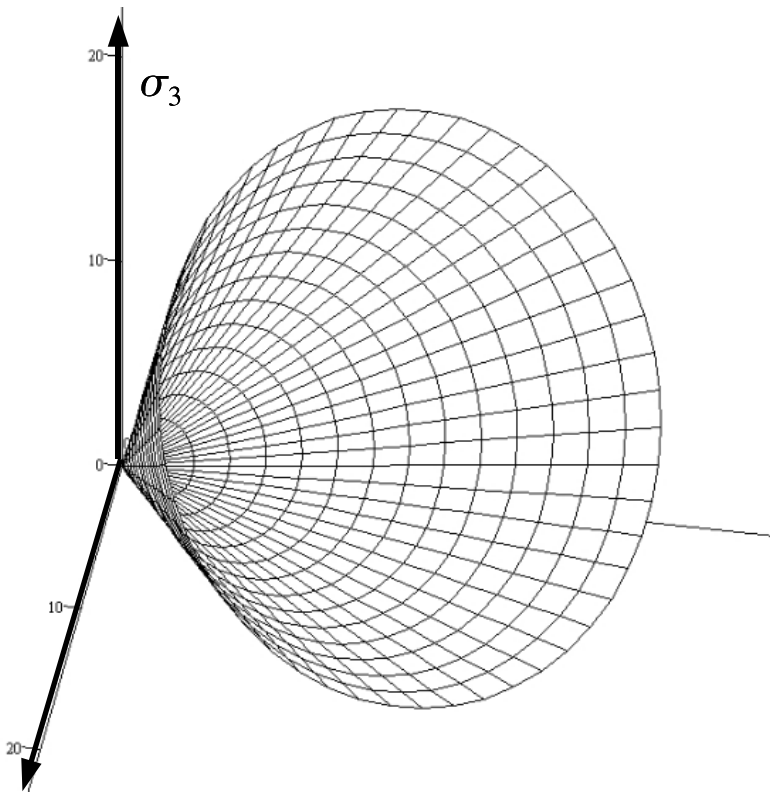

Figure 3.3: The Drucker-Prager Model without Cap

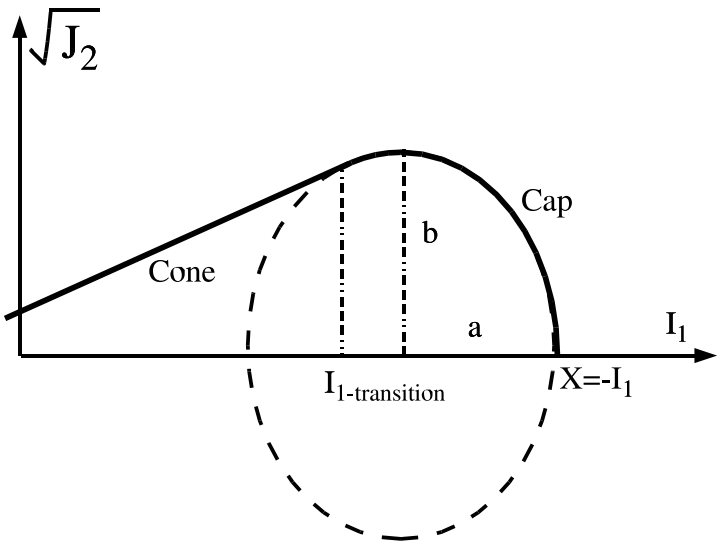

Figure 3.4: Elliptic Cap in the Drucker-Prager Model

In Figure 3.4, a and b is the shorter and longer principal axes of the ellipsoid, respectively. R is the ratio of a and b. X is the initial intersection of the cap with I_1 axis. $I_{1-transition}$ determines the transition point at which the cone portion and cap portion are connected by matching their tangent directions. Figure 3.5 shows a configuration of cap model of Drucker-Prager in 3-D. Replacing σ_Y and α_Y with σ_F and α_F in (3.36), one may build the corresponding flow function with cap for Drucker-Prager's models. For cap models, a user may also define a hardening rule for the cap by inputting a curve describing a relationship between volumetric plastic strain and mean stress.

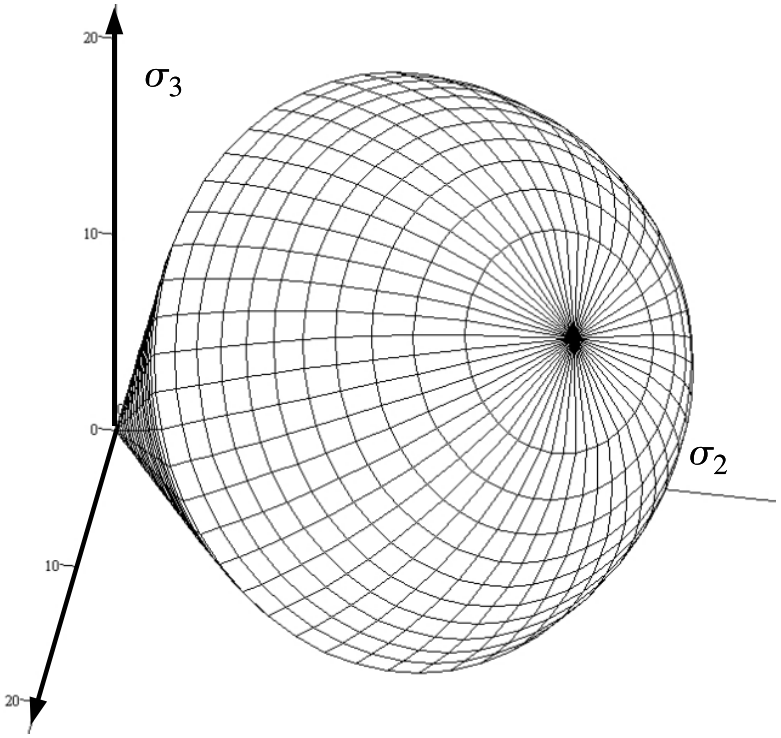

Figure 3.5: Drucker-Prager's Model with Cap

3.3 DG Variational Formulation

In this section, we use the evolutionary linear momentum equation to derive DG formulation for plasticity problems. We here follow the DG notations introduced in Chapter 2 for solving elasticity problems and the variational principles described in [47, 81]. The evolutionary momentum equation has the form:

$$\nabla \cdot \dot{\sigma}(u) + \dot{f} = 0. \tag{3.37}$$

Let $E \in \chi$. Multiplying (3.37) by $\dot{v} \in V$ and doing integration by parts, we obtain

$$\int_E \dot{\sigma}(u) : \nabla \dot{v} dV - \int_{\partial E} (\dot{\sigma}(u) n^s) \cdot \dot{v} dS = \int_E \dot{f} \cdot \dot{v} dV. \tag{3.38}$$

Noting that $\dot{\sigma}{:}\nabla\dot{v} = \dot{\sigma}{:}\nabla\dot{v}^T = \dot{\sigma}{:}\dot{\varepsilon}$, we have

$$\int_E \dot{\sigma}(u) : \dot{\varepsilon}(v) dV - \int_{\partial E} (\dot{\sigma}(u) n^s) \cdot \dot{v} dS = \int_E \dot{f} \cdot \dot{v} dV. \tag{3.39}$$

Then, summing over all elements over χ, we obtain

$$\sum_{E \in \chi} \int_E \dot{\sigma}(u) : \dot{\varepsilon}(v) dV - \sum_{\partial E \in S} \int_{\partial E} (\dot{\sigma}(u) n^s) \cdot \dot{v} dS = \sum_{E \in \chi} \int_E \dot{f} \cdot \dot{v} dV. \tag{3.40}$$

Applying the definitions of average and jump terms defined in (2.10)-(2.15) and using the fact

$$[\phi\varphi] = \{\phi\}[\varphi] + [\phi]\{\varphi\}, \tag{3.41}$$

we have

$$\begin{aligned} &\textstyle\sum_{E \in \chi} \int_E \dot{\sigma}(u) : \dot{\varepsilon}(v) dV - \sum_{\partial E \in S - \Gamma_t} \int_{\partial E} \{(\dot{\sigma}(u) n^s)\} \cdot [\dot{v}] dS \\ &\qquad = \textstyle\sum_{E \in \chi} \int_E \dot{f} \cdot \dot{v} dV + \int_{\Gamma_t} \dot{\bar{t}} \cdot \dot{v} dS. \end{aligned} \tag{3.42}$$

Adding face integrals $\int_{\partial E}\{(\dot{\sigma}(v)n^s)\}\cdot[\dot{u}]dS$ and $\frac{\delta}{|s|}\int_{\partial E}[\dot{u}]\cdot[\dot{v}]dS$ to (3.42), we have

$$\begin{aligned} a(\dot{u},\dot{v}) &= \textstyle\sum_{E\in\chi}\int_E \dot{\sigma}(u){:}\dot{\varepsilon}(v)dV - \sum_{\partial E\in S_i+\Gamma_u}\int_{\partial E}\{(\dot{\sigma}(u)n^s)\}\cdot[\dot{v}]dS \\ &+ \textstyle\sum_{\partial E\in S_i+\Gamma_u}\theta_{DG}\int_{\partial E}\{(\dot{\sigma}(v)n^s)\}\cdot[\dot{u}]dS + \sum_{\partial E\in S_i+\Gamma_u}\frac{\delta}{|s|}\int_{\partial E}[\dot{u}]\cdot[\dot{v}]dS \end{aligned} \tag{3.43}$$

and

$$\begin{aligned} L(\dot{v}) &= \textstyle\sum_{E\in\chi}\int_E \dot{f}\cdot\dot{v}dV + \int_{\Gamma_t}\dot{\bar{t}}\cdot\dot{v}dS \\ &+ \textstyle\sum_{\partial E\in\Gamma_u}\theta_{DG}\int_{\partial E}(\dot{\sigma}(v)n^s)\cdot\dot{\bar{u}}dS + \sum_{\partial E\in\Gamma_u}\frac{\delta}{|s|}\int_{\partial E}\dot{\bar{u}}\cdot\dot{\bar{v}}dS, \end{aligned} \tag{3.44}$$

where δ is the penalty parameter. Again, θ_{DG} forms a family of DG methods addressed in Chapter 2. It should be mentioned that the evolutionary constitutive relationship has already been given in (3.27). Therefore, by inserting (3.27) into (3.43) and (3.44), we are able to derive a displacement-based finite element formulation for plasticity problems.

The DG variational formulation for plasticity can be stated: *find* $\dot{u}\in V$ *such that:*

$$a(\dot{u},\dot{v}) = L(\dot{v}) \qquad \forall\,\dot{v}\in V. \tag{3.45}$$

3.4 DG Implementation

Most work for DG implementation for plasticity problems follows the same approach as for CG. Two different levels of implementations are required, i.e., global level and material level. On the global level the equilibrium equation

must be satisfied. As an admissible solution in stress (σ, ϑ) must belong to E_σ defined by (3.4), some special schemes such as stress return algorithms also involving nonlinear iterations have to be implemented on the material level.

3.4.1 Integration of Constitutive Law

In Section 3.3, a detailed DG formulation has been derived. However, because the evolutionary constitutive law is described in a form of infinitesimal stress and strain variation as follows:

$$\dot{\sigma} = D^{ep}(\sigma)\dot{\varepsilon} \tag{3.46}$$

or

$$d\sigma = D^{ep}(\sigma)d\varepsilon, \tag{3.47}$$

we have to do integration on (3.47) over a given load step in order to obtain finite increments $\delta\sigma$ and $\delta\varepsilon$ as follows:

$$\int_{\sigma_j}^{\sigma_j+\delta\sigma} d\sigma = \delta\sigma = \int_{\varepsilon_j}^{\varepsilon_j+\delta\varepsilon} D^{ep}(\sigma)d\varepsilon, \tag{3.48}$$

where the index j refers as to an initial state. As D^{ep} depends on current stress which is unkown, an approximation has to be performed. Several numerical integration schemes [82, 83] can be employed to (3.48). However, the most popular and simplest one is the Euler forward scheme that gives

$$\delta\sigma = D^{ep}(\sigma_j)\delta\varepsilon \tag{3.49}$$

Using (3.49) we are now able to do an incremental finite element formulation for plasticity problems. Replacing $\dot{\sigma}$, $\dot{\varepsilon}$, $\dot{u}$, and $\dot{v}$ with $\delta\sigma$, $\delta\varepsilon$, δu, and δv in

(3.43) and (3.44), we have the following incremental bilinear and linear forms:

$$\begin{aligned} a(\delta u, \delta v) &= \textstyle\sum_{E\in\chi} \int_E D^{ep}(\sigma_j)\delta\varepsilon(u){:}\delta\varepsilon(v)dV \\ &- \textstyle\sum_{\partial E\in S_i+\Gamma_u} \int_{\partial E}\{(D^{ep}(\sigma_j)\delta\varepsilon(u)n^s)\}\cdot[\delta v]dS \\ &+ \textstyle\sum_{\partial E\in S_i+\Gamma_u} \theta_{DG}\int_{\partial E}\{D^{ep}(\sigma_j)\delta\varepsilon(v)n^s)\}\cdot[\delta u]dS \\ &+ \textstyle\sum_{\partial E\in S_i+\Gamma_u} \frac{\delta}{|s|}\int_{\partial E}[\delta u]\cdot[\delta v]dS \end{aligned} \tag{3.50}$$

and

$$\begin{aligned} L(\delta v) &= \textstyle\sum_{E\in\chi}\int_E \delta f\cdot\delta v dV + \int_{\Gamma_t}\delta\bar{t}\cdot\delta v dS \\ &+ \textstyle\sum_{\partial E\in\Gamma_u}\theta_{DG}\int_{\partial E}(D^{ep}(\sigma_j)\delta\varepsilon(v)n^s)\cdot\delta\bar{u}dS \\ &+ \textstyle\sum_{\partial E\in\Gamma_u}\frac{\delta}{|s|}\int_{\partial E}\delta\bar{u}\cdot\delta\bar{v}dS. \end{aligned} \tag{3.51}$$

Following the same procedures in Chapter 2 for linear elasticity, we obtain interpolations

$$\begin{aligned} \delta u &= N\delta U \\ \delta\varepsilon &= B\delta U \\ \delta\sigma &= D^{ep}B\delta U. \end{aligned} \tag{3.52}$$

Inserting (3.52) into (3.50) and (3.51), we obtain the following algebraic system:

$$K\delta U = \delta F^E, \tag{3.53}$$

where

$$\begin{aligned} K &= \textstyle\sum_E k_V^E + \sum_S k_S^S, \\ k_V^E &= \textstyle\sum_{i=1}^{n_{gip}}[B_i, D_i^{ep}], \\ k_S^S &= \textstyle\sum_{j=1}^{m_{gip}}[B_j^L, D_j^{ep^L}, B_j^R, D_j^{ep^L}, n^s], \\ \delta F^E &= \textstyle\sum_{j=1}^{m_{gip}}[\bar{t}_j, N_j], \end{aligned} \tag{3.54}$$

where δU are the incremental displacements at nodes.

3.4.2 Stresses on Faces

The stiffness matrix K_V^E in (3.54) is computed by doing summation of stiffnesses over interior GIP. These computations involve computing the derivatives of flow and yield functions with respective to stresses. Moreover, much considerable work is needed to constrain stresses to be on the yield surface, which we will address in the next section. In general, as shown in Figure 3.6, both CG and DG methods need to perform computations at 8 interior GIP points if trilinear elements are used. However, DG methods need to do additional work on faces. For each trilinear element there are total 24 GIP on its 6 faces. Therefore, compared to CG, three times the work is, at least, needed for computing face stiffness for DG methods. To greatly reduce the work for faces, we propose an extrapolation scheme for DG methods, which is illustrated in Figure 3.6.

Using this scheme we don't need to store stresses on any face. First, we notice that the elastoplastic tensors D^{ep} at interior GIP may be stored at the time when we carry out volume integrations for K_V^E. These elastoplastic tensors can be used to obtain an approximation of D^{ep} at a GIP on a face. This can be done by extrapolation below:

$$D^{ep}_{k,face} = \sum_{i=1}^{n_{gip}} N_i D^{ep}_{i,body}, \tag{3.55}$$

where the subscript k indicates a GIP on element surfaces and the subscript i indicates an interior GIP. N_i is the extrapolation function contributed from the ith interior GIP. Second, if the elastoplastic tensors are not stored, an

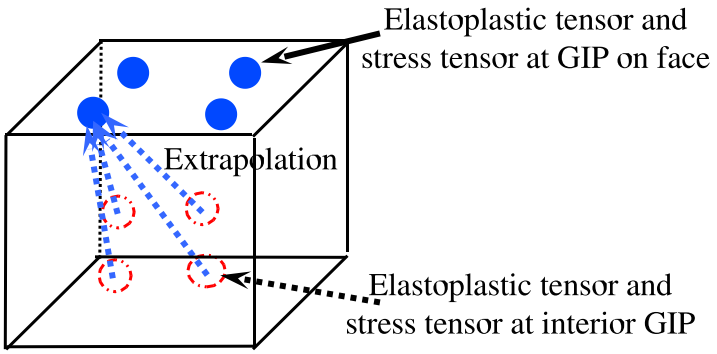

Figure 3.6: Extrapolation of Elastoplastic and Stress Tensors at Interior GIP for GIP on Surfaces

alternative is to extrapolate stress tensors other than elastoplastic tensors. Thus, using extrapolated stress tensors, we can compute elastoplastic tensors and finish computation for face stiffnesses. Stress tensors at surfaces can be extrapolated in the same way as elastoplastic tensors:

$$\sigma_{k,face} = \sum_{i=1}^{n_{gip}} N_i \sigma_{i,body}. \tag{3.56}$$

It should be noted that the errors of surface stresses will not be accumulated by this extrapolation scheme during nonlinear iterations. This is because stresses at interior GIP are always checked at each nonlinear iteration and constrained to an admissible stress state.

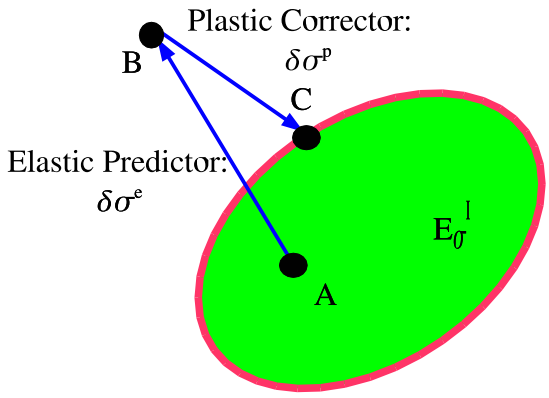

Figure 3.7: Radial Stress Return

3.4.3 Iteration on Material Level

After (3.53) is solved, the incremental stresses can be computed from the incremental displacements, and current stresses are then updated as

$$\sigma_{j+1} = \sigma_j + \delta\sigma. \tag{3.57}$$

However, $(\sigma_{j+1}, \vartheta_{j+1})$ is not guaranteed to be on the admissible spaces E_σ as the incremental constitutive law given in (3.49) is approximated by numerical integration. One could further divide each load step by many subincrementals to alleviate errors. However, errors may still accumulate and stresses may still drift away from admissible spaces. To avoid violating the consistency condition and resolving the system equation, the stress return algorithms have been developed in the literature [54, 55, 100–102] to constrain stresses on the yield surface. We review the Euler forward radial return algorithm.

This method assumes that solutions for incremental displacement and total incremental strain don't change during correction on stresses. An evolutionary relationship between stress and strain tensor can be deduced from the elastic constitutive law given in (3.11) and flow rule given in (3.12).

$$\dot{\sigma} = D(\dot{\varepsilon} - \dot{\varepsilon}^p) = D\dot{\varepsilon} - \dot{\gamma} D \frac{\partial F}{\partial \sigma}. \tag{3.58}$$

Considering that the consistency parameter $\dot{\gamma}$ actually indicates a flow path, the stress increment $\delta\sigma$ is obtained by integrating (3.58)

$$\delta\sigma = D\delta\varepsilon - \int_{\gamma_0}^{\gamma_0+\dot{\gamma}} D \frac{\partial F}{\partial \sigma} d\gamma. \tag{3.59}$$

We define an elastic predictor and a plastic corrector as follows

$$\delta\sigma^e = D\delta\varepsilon \tag{3.60}$$

and

$$\delta\sigma^p = \int_{\gamma_0}^{\gamma_0+\dot{\gamma}} D \frac{\partial F}{\partial \sigma} d\gamma. \tag{3.61}$$

Again, as the integration path from γ_0 to $\gamma_0 + \dot{\gamma}$ in the plastic prediction is unknown, an approximation must be made for this integration. As shown in Figure 3.7, the initial point A inside yield surface is projected into point B out of yield surface by the elastic predictor. As point B is known, we may use this point to approximate the plastic correction integration as follows

$$\delta\sigma^p = \dot{\gamma} D (\frac{\partial F}{\partial \sigma})_B. \tag{3.62}$$

Now, point B is corrected into point C as follows:

$$\sigma_C = \sigma_B - \delta\sigma^p = \sigma_B - \dot{\gamma} D (\frac{\partial F}{\partial \sigma})_B. \tag{3.63}$$

Point C should be expected to be on the yield surface

$$Y(\sigma_C) = Y(\sigma_B - \dot{\gamma} D(\frac{\partial F}{\partial \sigma})_B) = 0. \tag{3.64}$$

Considering a Taylor expansion of yield function around point B and taking the first two terms in the series we obtain

$$Y(\sigma_B - \dot{\gamma} D(\frac{\partial F}{\partial \sigma})_B) = Y(\sigma_B) - \dot{\gamma}(\frac{\partial Y}{\partial \sigma})_B : D(\frac{\partial F}{\partial \sigma})_B = 0. \tag{3.65}$$

The parameter $\dot{\gamma}$ can be solved by using (3.65) as follows

$$\dot{\gamma} = \frac{Y(\sigma_B)}{(\frac{\partial Y}{\partial \sigma})_B : D(\frac{\partial F}{\partial \sigma})_B}. \tag{3.66}$$

The total stress at $j+1$ is corrected by

$$\sigma_{j+1} = \sigma_j + \delta\sigma = \sigma_C = D\delta\varepsilon - \dot{\gamma} D(\frac{\partial F}{\partial \sigma})_B. \tag{3.67}$$

As σ_C may not be on the yield surface due to both integration approximation and Taylor expansion, iterations should be further performed until the error is small enough. The iteration procedures for this stress return scheme are summarized in Figure 3.8

For hardening cases yield surfaces are not static during stress return process but can be easily incorporated into the above iteration procedures by simply updating hardening parameters in functions in each iteration. More accurate return schemes can be found in [101]. Also, some convergence analysis for stress return algorithms using predictor and corrector was given in [49].

$$
\begin{array}{c}
\hline\hline
\textit{Initial point } \sigma_{j+1}^{0} \\
\textit{Iterations } k = 0, \ldots, m \\
\dot{\gamma} = \frac{Y(\sigma_{j+1}^{k})_B}{(\frac{\partial Y}{\partial \sigma_{j+1}})_B^k : D(\frac{\partial F}{\partial \sigma_{j+1}})_B^k} \\
\delta\sigma^p = \dot{\gamma} D(\frac{\partial F}{\partial \sigma_{j+1}})_B^k \\
(\sigma_{j+1}^{k+1})_C = (\sigma_{j+1}^{k})_B - \delta\sigma^p \\
B = C \\
\textit{Until } Y(\sigma_{j+1}^{k+1}) < tol \\
\hline\hline
\end{array}
$$

Figure 3.8: Radial Stress Return Scheme

3.4.4 Iteration on Global Level

On the global level the equilibrium equation must be satisfied, i.e., the balance between the force resultant of internal stresses and external loads must be achieved [101]. Newton's method is the most popular technique to do this work. To apply this method we divide total external load vector F^E into n steps denoted by

$$F_1^E,\ F_2^E, \ldots,\ F_n^E \tag{3.68}$$

and incremental loads

$$\Delta F_1^E,\ \Delta F_2^E, \ldots,\ \Delta F_n^E. \tag{3.69}$$

The force balance means

$$\Delta R_j = \Delta Q_j^I - \Delta F_j^E = 0, \tag{3.70}$$

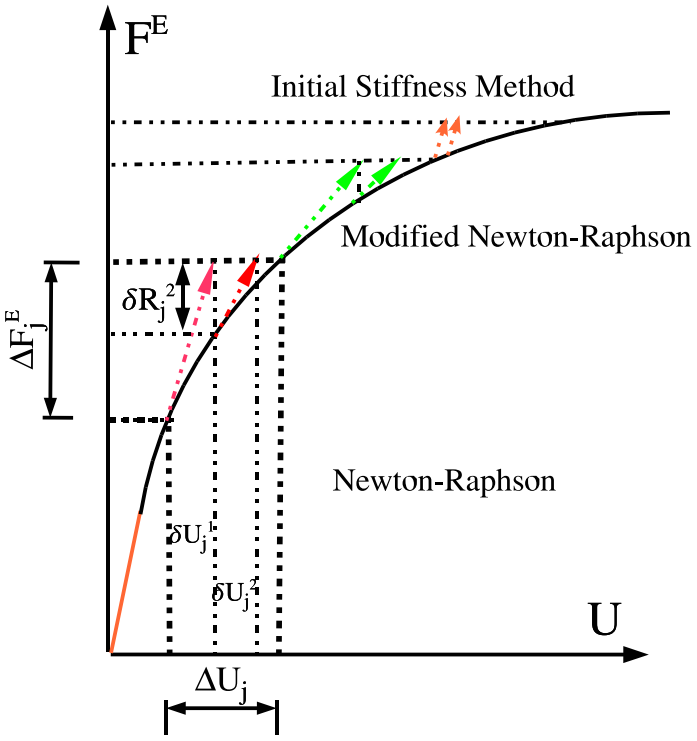

Figure 3.9: Nonlinear Iteration Methods

where ΔQ_j^I is the incremental resultant of internal stresses at load step j and given by

$$\Delta Q_j^I = \sum_E \int_E B^T \delta\sigma_j dV - \sum_{\partial E \in S_i + \Gamma_u} \int_{\partial E} [N^T]\{n\delta\sigma_j\} dS$$

$$+\theta_{DG} \sum_{\partial E \in S_i + \Gamma_u} \int_{\partial E} \{B^T (D_j{}^{ep})^T n^T\}[\delta u_j] dS + \sum_{\partial E \in S_i + \Gamma_u} \frac{\delta}{|s|} \int_{\partial E} [N^T][\delta u_j] dS \tag{3.71}$$

and ΔR_j and n are the residue vector and a matrix related to the normal vector n_s.

Newton-Raphson's method is described in Figure 3.9. We obtain total

$$
\begin{array}{l}
\text{==========} \\
\quad Initialize: \ U_0, F_0^E \\
\quad Load\ steps: \ j = 1, \ldots, n \\
\quad External\ force\ increment: \ \Delta F_j^E \\
\qquad\quad Initialize: \ \Delta U_j^0 \\
\qquad\quad Global\ iterations\ k = 1, 2, ... \\
\qquad\quad Check: \ Y = \left\{ \begin{array}{c} Y < 0 \Rightarrow D^{ep} = D \\ Y = 0 \Rightarrow D^{ep} \end{array} \right. \\
\qquad\quad Compute: \ K_{t,j}^k = K_{V,j}^k + K_{S,j}^k \\
\qquad\quad Form: \ \delta R_j^k = \Delta Q_j^{I,k} - \Delta F_j^E \\
\qquad\quad Solve: \ K_{t,j}^k \delta U_j^k = -\delta R_j^k \\
\qquad\quad Update: \ \Delta U_j = \Delta U_j + \delta U_j^k \\
\qquad\qquad\qquad\quad \Delta \varepsilon_j = \Delta \varepsilon_j + B \delta U_j^k \\
\qquad\qquad Material\ point\ iterations\ m = 1, 2, ... \\
\qquad\qquad Return\ stress: \ (\sigma_j, \vartheta_j) \notin E_\sigma \Rightarrow (\sigma_j, \vartheta_j) \in E_\sigma \\
\qquad\qquad Until\ Y(\sigma_j, \vartheta_j) < tol \\
\qquad\quad Until\ \left\| \delta R_j^k \right\|_2 < tol \cdot \|\Delta F\|_2 \\
\qquad\quad Update\ U_j = U_{j-1} + \Delta U_j \\
\qquad\qquad\qquad\quad \varepsilon_j = \varepsilon_{j-1} + \Delta \varepsilon_j \\
End\ load\ step \\
\text{==========}
\end{array}
$$

Figure 3.10: Newton-Raphson Method for Plasticity

incremental displacement vector ΔU_j at step j by another inner loop denoted by index k :

$$\Delta U_j = \delta U_j^1 + \delta U_j^2 + \cdots + \delta U_j^k + \cdots \tag{3.72}$$

The most inner loop is at the material level which we have already addressed in Section 3.3.2. We denote this loop by index m. The iterative procedures of Newton-Raphson's (NR) method applied to solving plasticity are summarized in Figure 3.10.

Besides NR method, the Modified Newton-Raphson (MNR) and Initial Stiffness methods have also been implemented in the dissertation. They are also illustrated in Figure 3.9. In MNR, the elastoplastic matrix is only updated at the beginning of each load step and keeps no change during iterations in a load step. Thus, it may greatly save CPU time. The work may be further saved by just using the initial elastic stiffness matrix for the whole iterative process. However, MNR and initial stiffness methods have less robustness than NR method.

3.5 A Beam in Bending

In this section we use a beam problem in bending to validate the formulation and program of DG methods when applied to plasticity. It is known that iterations for solutions often break down especially for cases when materials are close to ideal plasticity. This is because stiffness matrices are very singular when materials undergo large plastic deformation. This unstable process has been illustrated by this beam problem solved by CG method. We demonstrate that unstable iterative processes can be stabilized by using DG methods.

Figure 3.11 shows this beam problem. The beam is fixed at its left end and loaded by a moment M at its right end. The central portion of the beam has much lower yielding strength than other portions. From beam theory we know that the central portion will be in a pure bending state and will yield first. We now use material model with ideal plasticity with von Mises's properties. Also, beam height, beam thickness, Young's modulus, and yielding strength

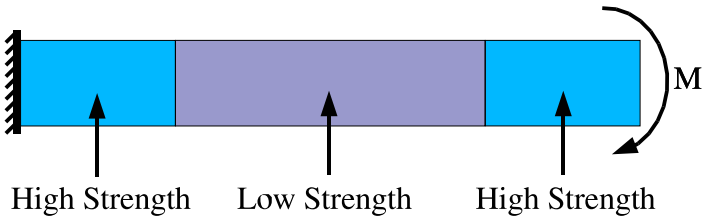

Figure 3.11: A Beam in Pure Bending

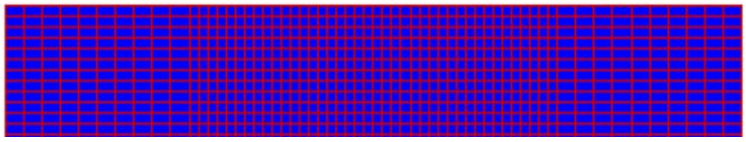

Figure 3.12: Meshing Profile of Beam Problem Solved by CG

σ_0 are all set to 1. Poisson's ratio is set to zero. The application of moment M is carried out by simply applying a uniform tension at the upper portion and an equal uniform compression at the lower portion of cross-section at the right end. The maximum value of uniform tension or compression is 1.

A three-dimensional mesh has been generated and used in computation but only a two-dimensional mesh is shown in Figure 3.12. In CG method we have total 1680 elements and 3630 nodes. Figure 3.13 shows beam yielding propagation from the top and bottom edges into the central line. The zone in red indicates yielding. As expected, plastic development simulated by CG method performs very well except at the last loading step. At the last load step, CG predicts that a few zones in the central portion are elastic or in

unloading states indicated by yellow and green. At the last stage, the whole central portion should be all in a uniform red. This demonstrates that CG method is not able to simulate a complete process of plastic development in the structure.

We now apply DG elements coupled with CG elements to solving this problem. Only the central line in the horizontal direction in the middle portion of the beam is needed to break. Therefore, DG still has the same number of elements but only 158 more nodes than CG.

Figure 3.14 shows the breaking line for DG. Figure 3.15 presents the evolutionary yielding process predicted by the DG method (OBB). This time, with DG method we are able to see a complete and perfect process of plastic development along whole cross-section.

3.6 Summary

DG methods for plasticity problems have been formulated. Coupled with CG, DG methods can be used to model plasticity problem efficiently. For example, CG can be used for zones in elasticity while DG is applied to areas where plasticity occurs, and refinement is necessary. In addition, CG methods are not able to model nearly incompressible plasticity.DG methods have potentials to handle plasticity problems with nearly incompressible materials as they are locking-free methods.

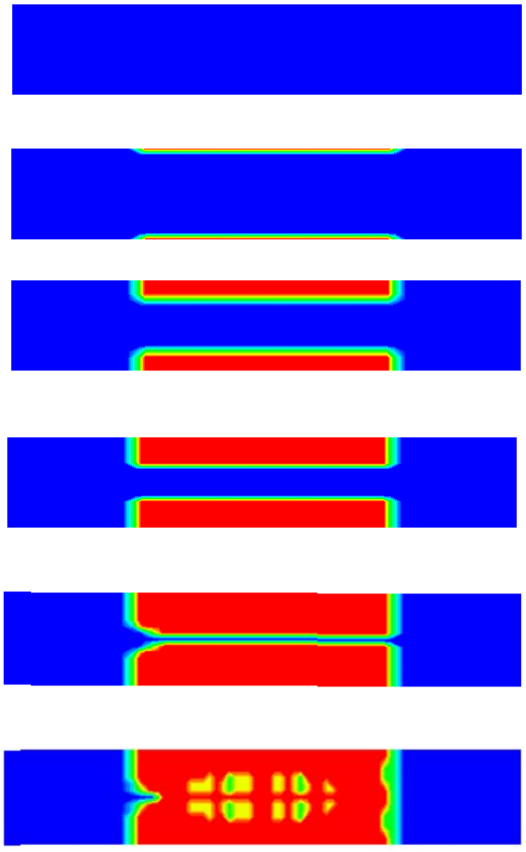

Figure 3.13: Plastic Development and Propagation of Beam Predicted by CG Simulation

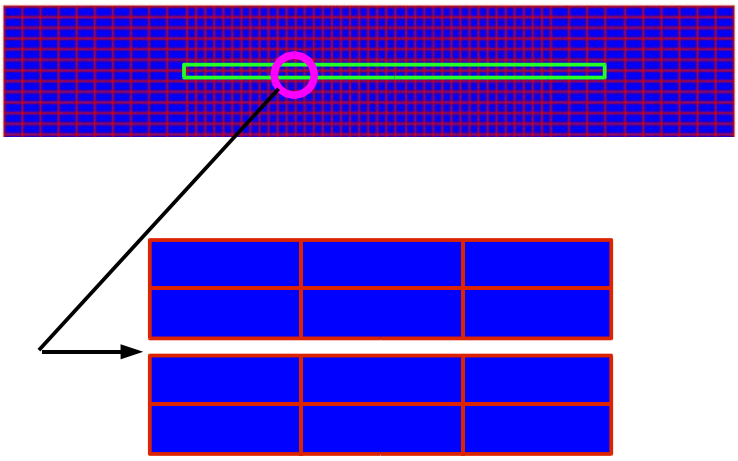

Figure 3.14: Broken Elements for DG Methods

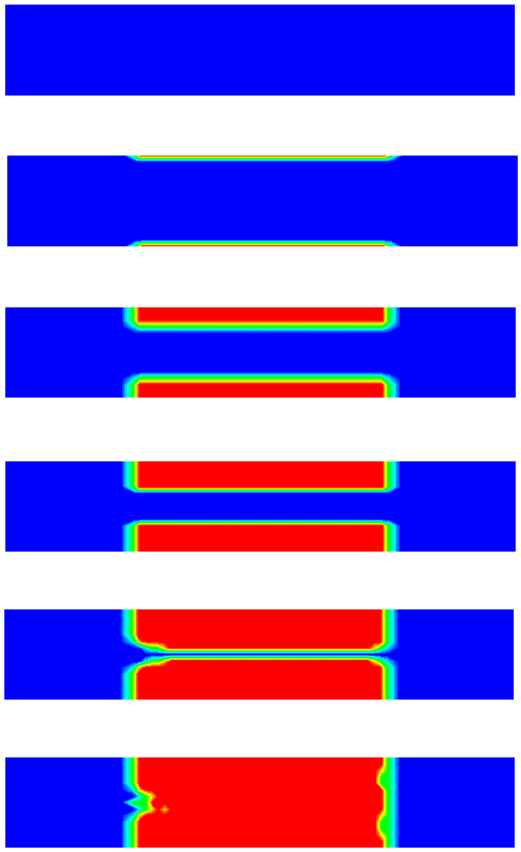

Figure 3.15: Plastic Development and Propagation of Beam Predicted by DG Simulation

Chapter 4

Modeling Poroelasticity-I

4.1 Objective

In this chapter we review mathematical theories and traditional CG finite element methods for poroelasticity problems. Detailed studies of the behavior of nonphysical pressure oscillations obtained from CG solutions are presented by solving the Mandel problem. Moreover, we demonstrate that the performance of unstable methods (linear elements for both solid and flow equations) for the cases of compressible models is much better than that for incompressible models. More importantly, we found that the magnitudes of oscillations obtained from stable methods are independent of permeabilities, but their decay rates do depend on permeabilities.

4.2 Governing Equations

Before proceeding with governing equations we introduce some key notations used throughout this chapter.

4.2.1 Notations

u: displacement field of solid phase (vector);

p: pore pressure of fluid (scalar);

σ: total Cauchy stress tensor;

σ'': effective Cauchy stress tensor;

$\bar{\sigma}$: mean effective stress (scalar);

ϵ: strain tensor;

ζ: variation of fluid content per unit reference volume (scalar);

f: body force of the porous mixture (vector);

s: source of fluid flow (scalar);

E: Young's modulus (scalar);

G: Shear modulus (scalar);

λ: Lame's constant (scalar);

υ: drained Poisson's ratio (scalar);

υ_u: undrained Poisson's ratio (scalar);

K: drained bulk modulus (scalar);

K_u: undrained bulk modulus (scalar);

K_s: bulk modulus of solid grain (scalar);

K_f: bulk modulus of fluid phase (scalar);

ϕ: porosity (scalar);

B: Skempton's pore pressure coefficient (scalar);

α: Biot's coefficient of effective stress (scalar);

M: Biot's modulus (scalar);

κ: permeability tensor;

q: flow rate (vector);

η: viscosity of fluid (scalar); and

c: generalized consolidation coefficient (scalar).

4.2.2 Material Constants

For isotropic porous media, Biot's constant α and Biot's modulus M, Skempton's constant B, and the generalized consolidation coefficient c can be expressed by [14, 23, 88]

$$\alpha = 1 - \frac{K}{K_s} = \frac{3(\nu_u - \nu)}{B(1-2\nu)(1+\nu_u)}, \tag{4.1}$$

$$B = \frac{(1-2\nu)(1+\nu_u)}{(\nu_u - \nu)}(\frac{K_s - K}{K_s}), \tag{4.2}$$

$$M = \frac{2GB^2(1-2\nu)(1+\nu_u)^2}{9(\nu_u - \nu)(1-2\nu_u)}, \tag{4.3}$$

$$c = \frac{2\frac{\kappa}{\eta}B^2G(1-\nu)(1+\nu_u)^2}{9(1-\nu_u)(\nu_u - \nu)}. \tag{4.4}$$

The range of the variation of B is $0 \sim 1$; for α, $0 \sim 1$; for M, $K \sim \infty$, and for ν_u, $\nu \sim 0.5$. The case of both incompressible fluid and incompressible solid constituents is reached when B, α, and M approach their upper bounds. This is corresponding to consolidation theories most often described in classic soil mechanics, in which governing equations are substantially simplified.

4.2.3 Governing Equations

The theory of poroelasticity is based on the following assumptions

(a) quasi-static state;

(b) linear elasticity of solid phase;

(c) isothermal process;

(d) compressible solid and fluid constituents;

(e) fully saturated media; and

(f) positive definite permeability tensor.

To simplify the process of derivation we also assume that solid skeletons are isotropic.

1. Constitutive Law

The constitutive law for porous media can be written in terms of five material constants G, ν, ν_u, B, and α as follows

$$\sigma = \frac{2G\nu}{1-2\nu}\nabla \cdot uI + 2G\epsilon - \alpha p \tag{4.5}$$

and

$$p = -\frac{2GB(1+\nu_u)}{3(1-2\nu)}\nabla \cdot u + \frac{2GB^2(1-2\nu)(1+\nu_u)^2}{9(\nu_u-\nu)(1-2\nu)}\zeta, \tag{4.6}$$

where I is the identity tensor. The relation between pore pressure and flow rate is given by Darcy's law

$$q = -\frac{\kappa}{\eta}\nabla p. \tag{4.7}$$

2. Kinematics

The relation of strain and displacement for solid skeletons is given by

$$\epsilon = \frac{1}{2}(\nabla u + \nabla u^T), \tag{4.8}$$

which is based on small deformation assumption.

3. Equilibrium Equations

$$\nabla \cdot \sigma + f = 0. \tag{4.9}$$

4. Continuity Equations

The continuity or mass conservation equation can be written in terms of ζ and c by

$$\dot{\zeta} - c\nabla^2\zeta = s. \tag{4.10}$$

5. Boundary Conditions

We denote Ω, the physical domain of a problem, and $\partial\Omega$, the boundary of the domain Ω. Then, we have

$$\partial\Omega = \partial\Gamma_u + \partial\Gamma_t = \partial\Gamma_p + \partial\Gamma_f, \tag{4.11}$$

where is $\partial\Gamma_u$ is the displacement boundary, $\partial\Gamma_t$ is the total stress or traction boundary, $\partial\Gamma_p$ is the pore pressure boundary, and $\partial\Gamma_f$ is the fluid flux boundary. The displacement boundary condition is

$$u = \bar{u} \qquad \text{on} \quad \partial\Gamma_u, \tag{4.12}$$

where $\bar{u}$ is the prescribed displacement on surface . The total stress or traction boundary condition on $\partial\Gamma_t$ is

$$\sigma n = \bar{t} \qquad \text{on} \quad \partial\Gamma_t, \tag{4.13}$$

where $\bar{t}$ denotes the prescribed tractions on surface and n denotes the unit normal vector. The pore pressure boundary condition is

$$p = \bar{p} \qquad \text{on} \quad \partial\Gamma_p, \tag{4.14}$$

where $\bar{p}$ denotes the prescribed pore pressure on surfaces. The fluid flux boundary condition is

$$-(\frac{\kappa}{\eta}\nabla p)\cdot n = \bar{q} \qquad \text{on} \quad \partial\Gamma_f, \tag{4.15}$$

where $\bar{q}$ denotes the prescribed flow normal to surface $\partial\Gamma_f$.

6. Initial Conditions

Initial conditions are given in terms of pressure and effective stress by

$$p = p_0 \qquad \text{on} \quad \Omega \quad at \quad t = 0 \tag{4.16}$$

and

$$\sigma'' = \sigma_0 \qquad \text{on} \quad \Omega \quad at \quad t = 0. \tag{4.17}$$

Based on (4.5)-(4.10), the governing equations for poroelasticity problems can be written in terms of two primary variables p and u only as follows, which are commonly used in finite element formulations:

$$\alpha\nabla\dot{u} + \frac{1}{M}\dot{p} - \nabla\cdot(\frac{\kappa}{\eta}\nabla p) = s, \tag{4.18}$$

$$(\lambda + G)\nabla(\nabla\cdot u) + G\nabla^2 u - \alpha\nabla p + f = 0 \tag{4.19}$$

with boundary conditions and initial conditions (4.12)- (4.17).

4.3 CG Solutions

4.3.1 Abstract Spaces and Bilinear Forms

We define some function spaces and bilinear forms for variational and finite element formulations in this chapter [71, 117, 118].

$L^2(\Omega)$: Hilbert space of square integrable scalar valued functions defined on Ω. Its inner product is defined as

$$(f_1,\ f_2) = \int_\Omega f_1 \cdot f_2 d\Omega \qquad \forall f_1,\, f_2 \in L^2(\Omega) \tag{4.20}$$

and the corresponding norm is

$$\parallel f \parallel_{L^2} = (f,\ f\ )^{\frac{1}{2}}. \tag{4.21}$$

$D^{|\zeta|}(\Omega)$: partial derivatives of function f with order ζ=$(\zeta_1,\ \zeta_2, \ldots, \zeta_2)$. It is defined by

$$D^{|\zeta|} = \frac{\partial^{|\zeta|}}{\partial_{x_1}^{\zeta_1} \partial_{x_2}^{\zeta_2} \cdots \partial_{x_n}^{\zeta_n}} \tag{4.22}$$

with

$$|\ \zeta\ | = \zeta_1 + \zeta_2 + \cdots + \zeta_n, \tag{4.23}$$

where $n = 2$ or 3.

$H^m(\Omega)$: Hilbert space of order m, with definition

$$H^m(\Omega) = \{f \in L^2(\Omega), \quad \forall\ |\ \zeta\ | \leq m,\ D^{|\zeta|} f \in L^2(\Omega)\} \tag{4.24}$$

with norm

$$\|f\|_m = (\sum_{|\zeta| \leq m} \left\| D^{|\zeta|} f \right\|^2_{L^2(\Omega)})^{\frac{1}{2}}, \tag{4.25}$$

and with seminorm

$$| f |_m = \|\partial^m f\|_{L^2(\Omega)}. \tag{4.26}$$

$H_0^1(\Omega)$: Hilbert space of order 1, with definition

$$H_0^1(\Omega) = \{f \in H^1(\Omega), \quad f = 0 \quad on\ \partial\Omega\}. \tag{4.27}$$

V : function space of displacement field, defined by

$$V = \{f \in H^1(\Omega), \quad f = u_D \quad on\ \partial\Omega_1\}. \tag{4.28}$$

W : function space of pore pressure field, defined by

$$W = \{f \in H^1(\Omega), \quad f = p_D \quad on\ \partial\Omega_3\}. \tag{4.29}$$

$V_h^{r_1}$: continuous piecewise polynomial finite element space of V with degree r_1.

$W_h^{r_2}$: continuous piecewise polynomial finite element space of W with degree r_2.

$a(u, v)$: bilinear form on V corresponding to the elasticity equation defined by

$$a(u, v) = \int_\Omega \{\lambda(\nabla \cdot u)(\nabla \cdot v) + 2G\epsilon(u) : \epsilon(v)\} d\Omega. \tag{4.30}$$

$b(u, v)$: bilinear form on W corresponding to the fluid equation defined by

$$b(u, v) = \int_\Omega \frac{\kappa}{\eta} \nabla u \cdot \nabla v d\Omega. \tag{4.31}$$

$\| u \|_{E_a}$: energy norm related to elasticity defined by

$$\| u \|_{E_a} = \{a(u,u)\}^{\frac{1}{2}}. \tag{4.32}$$

$\| p \|_{E_b}$: energy norm related to fluid flow defined by

$$\| p \|_{E_a} = \{b(p,p)\}^{\frac{1}{2}}. \tag{4.33}$$

4.3.2 Variational Formulation

The statement of variation formulation for poroelasticity problems described by (4.18) and (4.19) is given as follows

Find $\{u(x,t), p(x,t)\} \in V \times W$ such that

$$\alpha(\nabla \cdot u_t, w) + \frac{1}{M}(p_t, w) + b(p, w) = \hat{q}(w) \quad \forall w \in W, \tag{4.34}$$

$$a(u, v) - \alpha(p, \nabla \cdot v) = \hat{f}(v) \quad \forall v \in V, \tag{4.35}$$

where

$$\hat{q}(w) = \int_{\partial\Gamma_f} \bar{q} w d\Gamma + (s, w), \tag{4.36}$$

$$\hat{f}(v) = \int_{\partial\Gamma_t} \bar{t} \cdot v d\Gamma + (f, v), \tag{4.37}$$

with initial conditions

$$p = p_0 \qquad \text{on} \quad \Omega \quad at \quad t = 0 \tag{4.38}$$

and

$$\sigma'' = \sigma_0 \qquad \text{on} \quad \Omega \quad at \quad t = 0\,. \tag{4.39}$$

4.3.3 Discretization in Spatial Domain

Based on the statement of variational formulation given in (4.34) and (4.35), the semidiscrete Galerkin finite element approximation for poroelasticity problems is given as follows

Find $\{u_h(x,t), p_h(x,t)\} \in V_h^{r_1} \times W_h^{r_2}$ such that

$$\alpha(\nabla \cdot u_{ht}, w_h) + \frac{1}{M}(p_{ht}, w_h) + b(p_h, w_h) = \hat{q}(w_h) \quad \forall w_h \in W_h^{r_2}, \tag{4.40}$$

$$a(u_h, v_h) - \alpha(p_h, \nabla \cdot v_h) = \hat{f}(v_h) \quad \forall v_h \in V_h^{r_1}, \tag{4.41}$$

where

$$\hat{q}(w_h) = \int_{\partial\Gamma_f} \bar{q} w_h d\Gamma + (q, w_h), \tag{4.42}$$

$$\hat{f}(v_h) = \int_{\partial\Gamma_t} \bar{t} \cdot v_h d\Gamma - (f, v_h), \tag{4.43}$$

with initial conditions

$$p_h = p_0 \qquad \text{on} \quad \Omega \quad at \quad t = 0, \tag{4.44}$$

and

$$\sigma_h'' = \sigma_0 \qquad \text{on} \quad \Omega \quad at \quad t = 0. \tag{4.45}$$

We now introduce shape functions for primary variables u_h, and p_h interpolated by node values U and P as follows

$$u_h = N_u U, \tag{4.46}$$

$$\epsilon_h = B_u U \tag{4.47}$$

$$p_h = N_p P, \tag{4.48}$$

where N_u, B_u, and N_p are interpolation matrices or vectors for displacement, strain, and pore pressure, respectively. Inserting (4.46) - (4.48) into (4.40) and (4.41), we obtain ordinary differential equations in terms of time variable [63] as follows

$$K\frac{dU}{dt} + L\frac{dP}{dt} - \frac{d\hat{f}}{dt} = 0, \tag{4.49}$$

$$HP + S\frac{dP}{dt} + L^T\frac{dP}{dt} - \frac{d\hat{q}}{dt} = 0, \tag{4.50}$$

where

$$K = -\int_\Omega B_u^T D B_u d\Omega, \tag{4.51}$$

$$L = \int_\Omega B_u^T D\vec{\alpha} N_p d\Omega, \tag{4.52}$$

$$S = \int_\Omega \frac{1}{M} N_p^T N_p d\Omega, \tag{4.53}$$

$$H = \int_\Omega \nabla N_p^T \frac{\kappa}{\eta} \nabla N_p d\Omega, \tag{4.54}$$

$$\hat{f} = -\int_\Omega N_u^T f d\Omega - \int_{\partial\Omega_2} N_u^T \bar{t} d\Omega, \tag{4.55}$$

$$\hat{q} = \int_\Omega N_p^T s d\Omega - \int_{\partial\Omega_2} N_p^T \bar{q} d\Omega, \tag{4.56}$$

where $\vec{\alpha} = (\alpha, \alpha, \alpha, 0, 0, 0)$.

4.3.4 Discretization in Temporal Domain

Time discretizations may be treated as a one-dimensional finite element problem. The first-order time derivatives in (4.49) and (4.50) are approximated by assuming a linear variation of $\overline{u}$ and $\overline{p}$ within each time step. A detailed

derivation can be found in [63]. Here, we directly give algebraic equations after discretization in time:

$$\begin{bmatrix} K & L \\ L^T & S+\theta\Delta t_k H \end{bmatrix} \begin{Bmatrix} U \\ P \end{Bmatrix}_{t_k+\Delta t_k} = \begin{bmatrix} K & L \\ L^T & S-(1-\theta)\Delta t_k H \end{bmatrix} \begin{Bmatrix} \overline{u} \\ \overline{p} \end{Bmatrix}_{t_k} + \begin{Bmatrix} \frac{d\hat{f}}{dt} \\ \hat{q} \end{Bmatrix} \triangle t_k \tag{4.57}$$

where θ is a constant related to time schemes, $\triangle t_k$ is the length of the k-th time step. The time schemes are summarized in terms of different values of θ as follows

$\theta = 0$: Euler forward finite difference method;

$\theta = 1$: backward finite difference method;

$\theta = \frac{1}{2}$: Crank-Nicholson finite difference method;

$\theta = 0.6667$: Zienkiewicz Galerkin method;

$\theta = 1 + (\frac{1}{\triangle t} - \frac{1}{ln(1+\triangle t)})$: Sanhu logarithmic method ; and

$\theta = 1 + \frac{t_k}{t_{k+1}-t_k} - \frac{1}{ln(1+\frac{t_{k-1}-t_k}{t_k})})$: Hwang logarithmic method.

The stability analysis in time was discussed by Book and Small [15], in which they proved that $\theta \geq \frac{1}{2}$ is corresponding to unconditionally stable methods in time.

4.3.5 Stable and Unstable Methods

In mixed finite element methods for solving incompressible elasticity, primary variables are displacement u and p. The variable p is the mean stress

in solid. These two primary variables have to satisfy the LBB inf-sup [19] condition in order to obtain accurate results. Schemes that satisfy the inf-sup condition are called stable methods [19, 20]. Schemes that don't satisfy the inf-sup condition are called unstable methods. In this dissertation, all stable and unstable methods refer to schemes in the spatial other than in the temporal as we always use stable time schemes. These terminologies are also used in the field of coupled problems of fluid and solid because two primary variables are also involved in (4.57) [126]. However, mixed finite element methods are derived from a single equation, while (4.57) directly comes from two different equations and does not involve any idea of mixed finite element theories. It should be pointed out that unstable methods can still be used for solving coupled problems without serious stability problems in most cases (compressible models or large time steps). In fact, the most popular finite element scheme used in practice for coupled problems employs linear elements for both displacement and fluid pore pressure, which is unstable from a point view of mixed finite element theories. However, stable methods have better performance in solving poroelasticity problems, which will be shown in this chapter. In addition, mixed finite element theories for Stokesian flow problems [40, 79, 80] are very helpful for the stability study of poroelasticity solved by CG methods. It is necessary to point out that stable methods are not absolutely stable for poroelasticity problems as there is a time issue involved, which will be shown in the next section.

Trilinear isoparametric hexahedral elements are the most popular 3-

D elements used in practice. 27-node isoparametric hexahedral elements are also frequently employed. The configurations of these two elements and their combinations of displacement and pressure have already been shown in Figure 2.3. The use of 27-node element for displacements and 8-node element for pressures (red nodes in Figure 2.3) is stable from the point view of mixed theories and called Taylor-Hood's element. 8-node elements for both displacement and pressure is an unstable method. It should be mentioned that the use of 8-node elements is much cheaper than Taylor-Hood's elements, but the use of Taylor-Hood's element is necessary to address problems having complex curved boundaries (like injection well problems).

There are a few error estimates for poroelasticity in the literature. A key technique used to derive these error estimate is the elliptic projection method for parabolic problems introduced by Wheeler [117] and exploited in [59, 110]. Murad etc. [71–73] have applied this elliptic projection method for problems with incompressible fluid and solid constituents. Using the elliptic projection method, Wheeler and Phillips [85] have performed the convergence analysis of mixed finite element methods for poroelasticity problems. These error estimates have provided an important theoretical basis for finite element methods as applied to poromechanics. In this chapter we present some numerical experiments to show more detailed behaviors of performance of CG methods including stable and unstable schemes.

4.4 Nonphysical Pressure Oscillation

Step functions are of some interest in many practical applications. Pore pressures remain zero at free drainage surfaces but jump, over an extremely short distance into media, to a value comparable with applied stress, and in a very short time. These initial pressure responses near boundaries are of a high gradient. Traditional CG finite elements with regular mesh are not able to handle this locally high pressure gradient. The initial behavior of poroelastic media is similar to that of an incompressible solid [44]. Therefore, a strict procedure to obtain initial responses should require a scheme to model this incompressibility, which could be very complex and totally different from schemes we have just discussed in this chapter. In practical applications, an approximation to initial responses for coupled systems is obtained by taking a very small time step, which may induce oscillations in solutions. We use the Mandel problem to demonstrate such nonphysical oscillations.

4.4.1 Mandel Problem

4.4.1.1 Problem Statement

A poroelastic body is compressed between two rigid plates under a constant vertical force of 2F as shown in Figure 4.1. The plane strain condition is assumed. The impervious flow boundary is shown by two purple lines. The pressure at the line of $x = \pm a$ is zero. The load is applied instantaneously and is then held constant over time. We are interested in the solution of pressure, stress, and displacement based on Biot's consolidation theory.

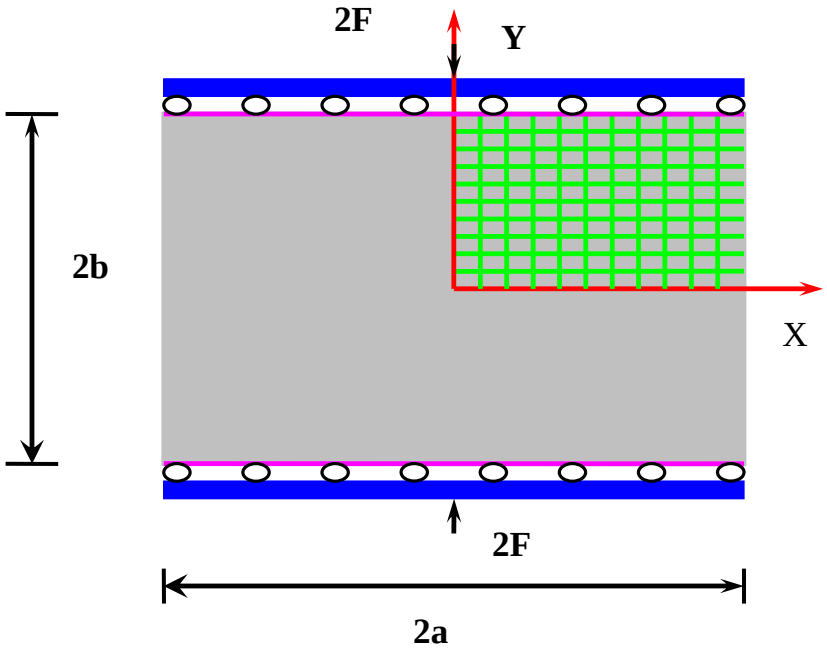

Figure 4.1: Mandel Problem

This problem was first given and solved analytically by Mandel in 1950 [68]. Using this problem, Mandel was the first who demonstrated the critical difference between Biot's consolidation theory and the earlier theory of Terzaghi in prediction of fluid pore pressure [23, 32]. The pressure solution based on Terzaghi theory always diffuses monotonically. The solution given by Biot's theory exhibits a non-monotonic variation with time, i.e., the pressure goes up in the central region of the body at its early evolution stages. This effect is now known as Mandel-Cryer's effect. This effect is physically realistic and was confirmed experimentally by Verruijt [112]. The original Mandel problem assumes the incompressibility of both fluid and solid constituents. Here, we study an extended Mandel problem given by Cheng and Detournay [23], in which both constituents of fluids and solids are compressible. This problem is a key benchmark for validation of numerical schemes for poroelasticity with compressible solid and fluid constituents. It should be mentioned that the Mandel problem seems very simple in its statement, but the procedures based on numerical schemes are very complex because the constraint equations, which describe the rigid plate condition, must be carefully implemented.

4.4.2 Analytical Solution

Complete analytical solutions for general cases to all field quantities including displacement, stress, pore pressure, and fluid flux, were given by Cheng and Detournay [23]. For completeness we give their solutions as follows

$$u_x = \left[\frac{F\nu}{2Ga} - \frac{F\nu_u}{2Ga} \sum_{i=1}^{\infty} \frac{\sin\alpha_i \cos\alpha_i}{\alpha_i - \sin\alpha_i \cos\alpha_i} e^{(-\alpha_i^2 ct/a^2)} \right] x$$

$$+\frac{F}{G}\sum_{i}^{\infty}\frac{\cos\alpha_i}{\alpha_i-\sin\alpha cos\alpha_i}\sin\frac{\alpha_i x}{a}e^{(-\alpha_i^2 ct/a^2)}, \tag{4.58}$$

$$u_y=\left[\frac{F(1-\nu)}{2Ga}+\frac{F(1-\nu_u)}{Ga}\sum_{i=1}^{\infty}\frac{\sin\alpha_i\cos\alpha_i}{\alpha_i-\sin\alpha_i\cos\alpha_i}e^{(-\alpha_i^2 ct/a^2)}\right]y, \tag{4.59}$$

$$\sigma_{xx}=0 \tag{4.60}$$

$$\sigma_{yy}=-\frac{F}{a}-\frac{2F(\nu_u-\nu)}{Ga}\sum_{i=1}^{\infty}\frac{\sin\alpha_i}{\alpha_i-\sin\alpha_i\cos\alpha_i}\cos\frac{\alpha_i x}{a}e^{(-\alpha_i^2 ct/a^2)}$$

$$+\frac{2F}{a}\sum_{i}^{\infty}\frac{\sin\alpha\cos\alpha_i}{\alpha_i-\sin\alpha_i\cos\alpha_i}e^{(-\alpha_i^2 ct/a^2)}, \tag{4.61}$$

$$\sigma_{xy}=0 \tag{4.62}$$

$$p=\frac{2FB(1+\nu_u)}{3a}\sum_{i=1}^{\infty}\frac{\sin\alpha_i}{\alpha_i-\sin\alpha_i\cos\alpha_i}(\cos\frac{\alpha_i x}{a}-\cos\alpha_i)e^{(-\alpha_i^2 ct/a^2)}, \tag{4.63}$$

$$q_x=\frac{2FB\frac{\kappa}{\eta}(1+\nu_u)}{3a^2}\sum_{i=1}^{\infty}\frac{\alpha_i\sin\alpha_i}{\alpha_i-\sin\alpha_i\cos\alpha_i}\frac{\sin\alpha_i x}{a}e^{(-\alpha_i^2 ct/a^2)}, \tag{4.64}$$

$$q_y=0, \tag{4.65}$$

where

$$\tan\alpha_i=\frac{1-\nu}{\nu_u-\nu}\alpha_i. \tag{4.66}$$

The key step to obtain analytical solutions for Mandel's problem is to solve an eigenvalue problem based on (4.66). Figure 4.2 draws the analytical solution of pressure following time for the case of compressible solid and fluid constituents. Material constants are $E=1.0e+7$, $\nu=0.2$, $\nu_u=0.4$, $B=0.8$, $\alpha=0.89$, $M=1.75e+7$, and $\frac{\kappa}{\eta}=1.0e-10$. It shows that the pressure solution first goes up in the central region at earlier stages and then drops down and diffuses monotonically in longer time.

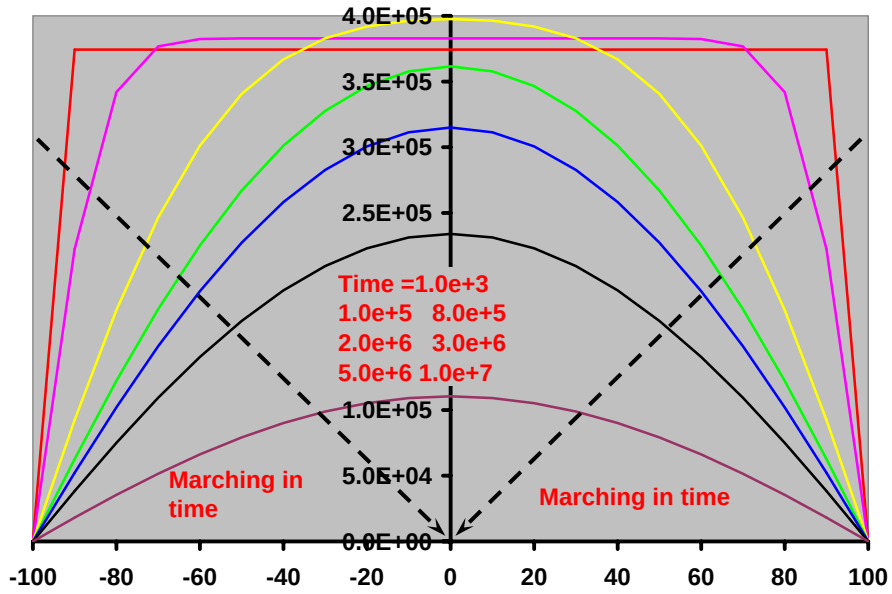

Figure 4.2: Mandel Problem: Analytical Solution of Pore Pressure

4.4.3 CG Solution

Numerical solutions for Mandel's problem based on CG finite element methods are shown in Figure 4.3 through Figure 4.11. Only pressure fields are presented in these figures. For compressible cases, all material constants are the same as those shown in analytical solution. For all cases E and ν don't change. The features of solutions obtained from different finite element schemes and time steps are discussed in this section. Also, the following chart describes factors we test in this numerical example.

$$Models \begin{bmatrix} Incompressible \begin{bmatrix} Talyor-Hood \begin{bmatrix} Large\,Time\,Step \\ Small\,Time\,Step \end{bmatrix} \\ Linear\,Element \begin{bmatrix} Large\,Time\,Step \\ Small\,Time\,Step \end{bmatrix} \end{bmatrix} \\ Compressible \begin{bmatrix} Talyor-Hood \begin{bmatrix} Large\,Time\,Step \\ Small\,Time\,Step \end{bmatrix} \\ Linear\,Element \begin{bmatrix} Large\,Time\,Step \\ Small\,Time\,Step \end{bmatrix} \end{bmatrix} \end{bmatrix} \tag{4.67}$$

4.4.3.1 Time Step Effect

We first study incompressible cases ($M = \infty$, $\alpha = 1$). Figure 4.3 shows a serious oscillation in pressure solutions in the portions close to boundaries. These results are obtained from the use of linear elements for displacements and linear element for fluid pore pressures and the use of a small time step

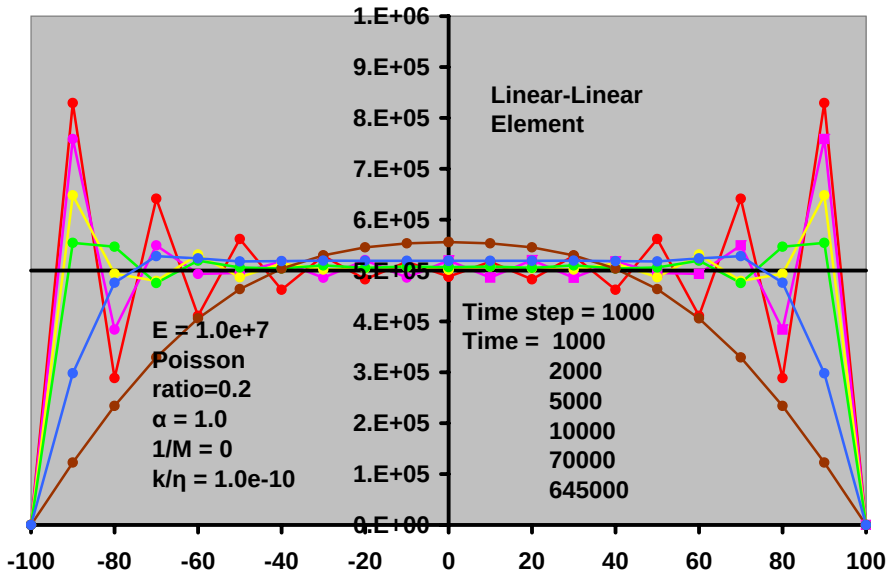

Figure 4.3: Mandel's Problem: CG Solution of Pore Pressure; Incompressible Case; Linear-Linear Element.

$t = 1000$. At the first time step, the pressure is polluted in the whole domain. The oscillation decays following evolution process in time.

Figure 4.4 shows much reduced oscillation in pressure solutions with increase in time steps. The use of time step $>$ 20000 will not induce any obvious oscillation. However, such a large time step is often prohibited in practice applications because of its low accuracy and resolution.

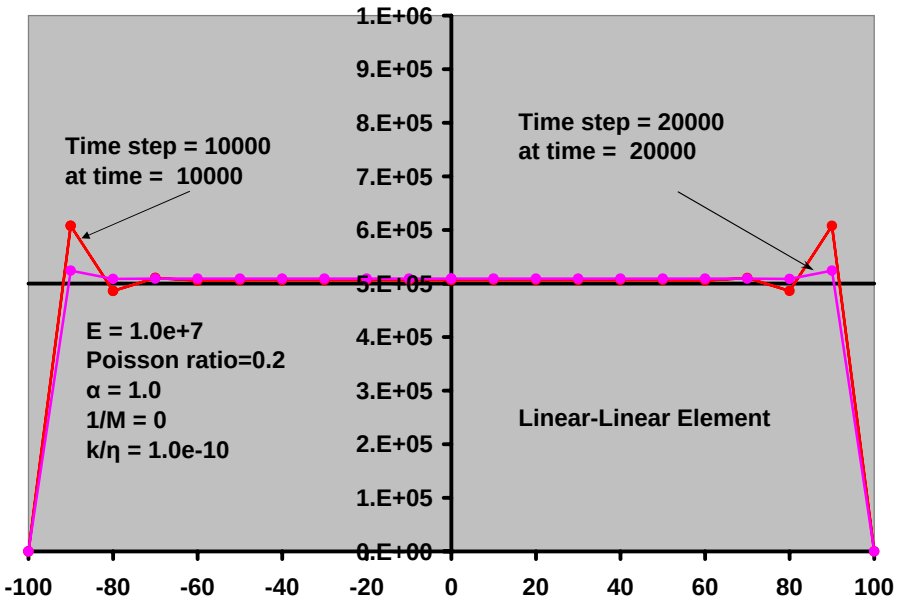

Figure 4.4: Mandel's Problem: CG Solution of Pore Pressure; Incompressible Case; Linear-Linear Element; Much Larger Time Step

4.4.3.2 Element Type Effect

In the cases of incompressible solid and fluid constituents, the pressure results given by stable methods, i.e., Taylor-Hood's elements, are shown in Figure 4.5. These results are much improved if compared with Figure 4.3. The pollution in solutions is local. It should be kept in mind that this improvement is in the price of 27 nodes in each higher order element rather than 8 nodes in each linear element. In addition, there are still nonphysical spikes near boundaries, which indicate that stable elements are not absolutely stable when applied to poroelasticity problems. This is different from the cases where accurate solutions are always achieved when Talyor-Hood's elements are applied to single equation like pure elasticity.

4.4.3.3 Permeability Effect

We now reduce $\frac{\kappa}{\eta}$ by two levels from 1.0×10^{-10} to 1.0×10^{-12} to study permeability effects on pressure oscillations. Figure 4.6 shows that the pressure oscillates in almost equal magnitudes in the whole domain for the case of linear-linear elements. The decay of oscillations needs two orders of magnitude longer time than the cases with relatively high permeability.

When Taylor-Hood's element is used, the magnitude of oscillations in pressure solutions is not affected by change in permeabilities from $1.0e-10$ to $1.0e-12$. This can be concluded from comparing Figure 4.7 with Figure 4.5. However, the decay rate does depend on the magnitude of permeabilities, i.e., stable methods will not improve the decay rate of oscillations.

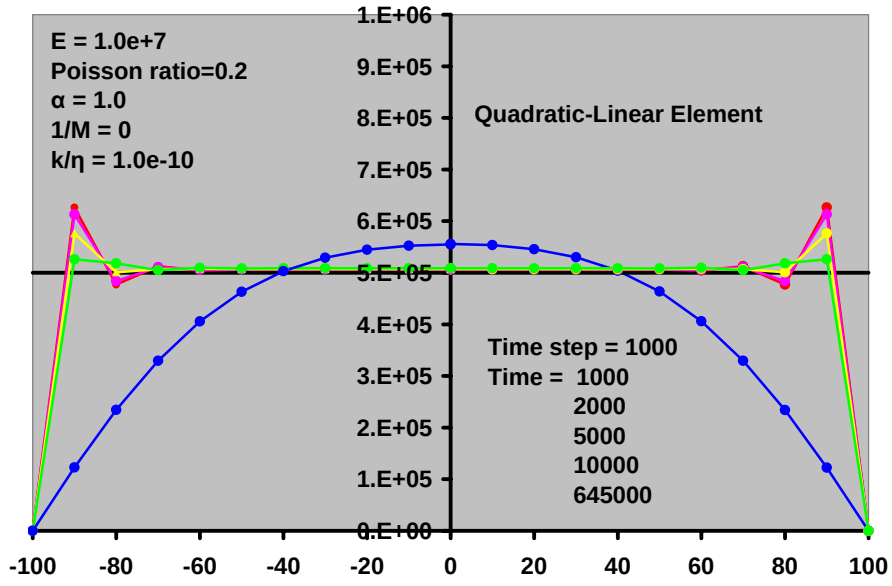

Figure 4.5: Mandel's Problem: CG Solution of Pore Pressure; Incompressible Case; Taylor-Hood's Element.

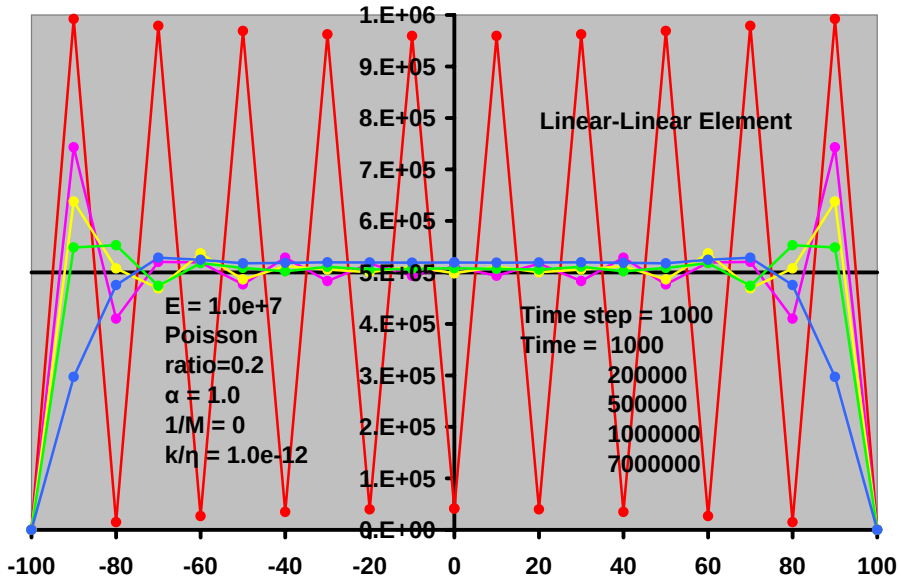

Figure 4.6: Mandel's Problem: CG Solution of Pore Pressure; Incompressible Case; Linear-Linear Element; Relatively Lower Permeability

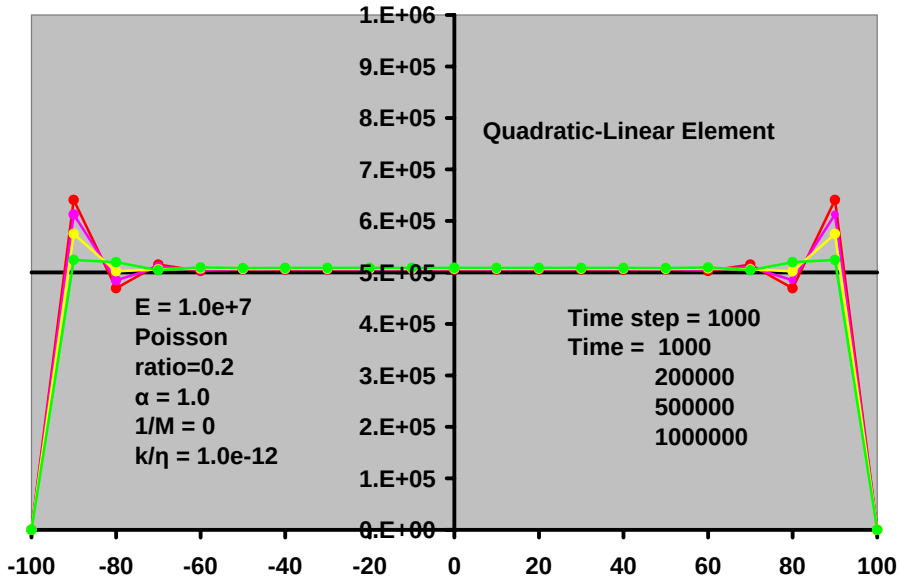

Figure 4.7: Mandel's Problem: CG Solution of Pore Pressure; Incompressible Case; Taylor-Hood's Element; Relatively Lower Permeability

4.4.3.4 Compressibility Effect

We now assume that the constituents of both solid and fluid are compressible. Biot's modulus is set to $M = 1.75e + 7$, which is close to the bulk modulus of solid skeletons. For linear-linear element schemes, the oscillation shown in Figure 4.8 is greatly reduced if compared to the result of incompressible cases shown in Figure 4.3. Also, the magnitude of permeability doesn't affect the behavior of oscillations, which can be seen by comparing Figure 4.8 with Figure 4.9. Similar results are observed in Figures 4.10 and 4.11 for the use of Taylor-Hood's elements. After carefully checking Figure 4.8 through Figure 4.11, we see that there is no obvious difference in the magnitude of oscillations between stable and unstable methods for this compressible model. This observation is very important. In petroleum engineering, the compressibilities of both rock and fluid are not negligible. Expensive Taylor-Hood's elements chosen for rocks may not have better performance in the improvement on pressure oscillations than the cheaper linear-linear elements.

4.4.4 Discussion

1. Oscillations in pressure solutions obtained by using small time steps are also observed in the case of free drainage surface but not loaded.

2. Oscillations decay following the lapse of time and eventually disappear.

3. In the case of incompressible constituents of both solid and fluid, oscillations obtained by stable methods do not depend on permeabilities but

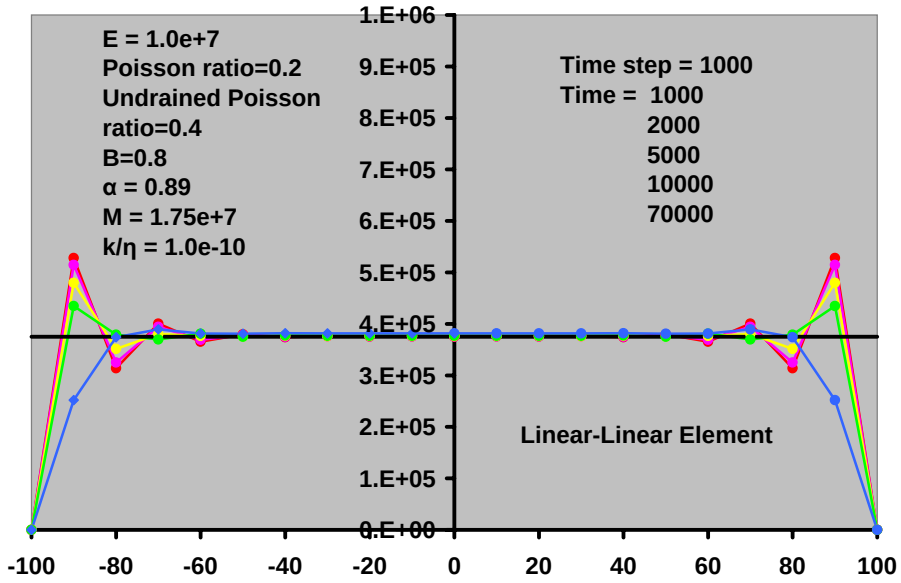

Figure 4.8: Mandel Problem: CG Solution of Pore Pressure; Compressible Case; Linear-Linear Element

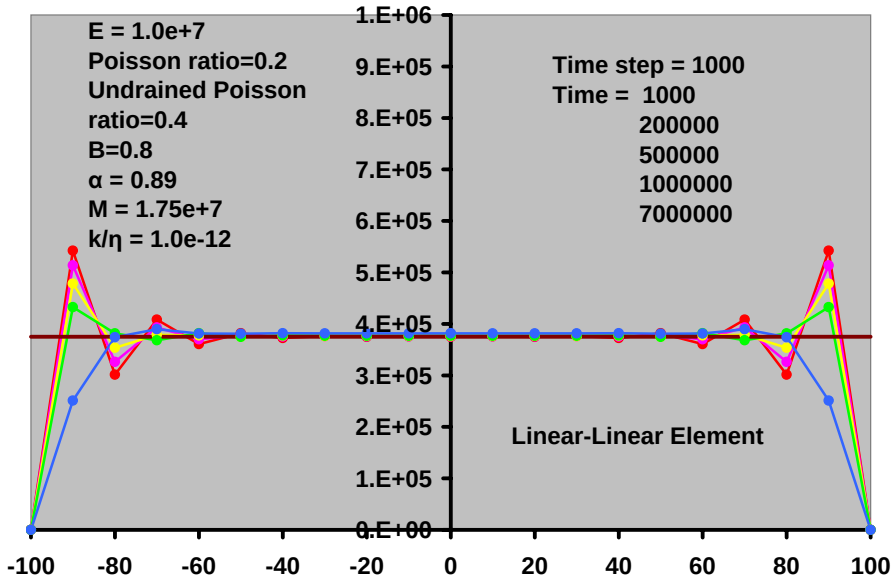

Figure 4.9: CG Solution of Pore Pressure; Compressible Case; Linear-Linear Element; Relatively Lower Permeability

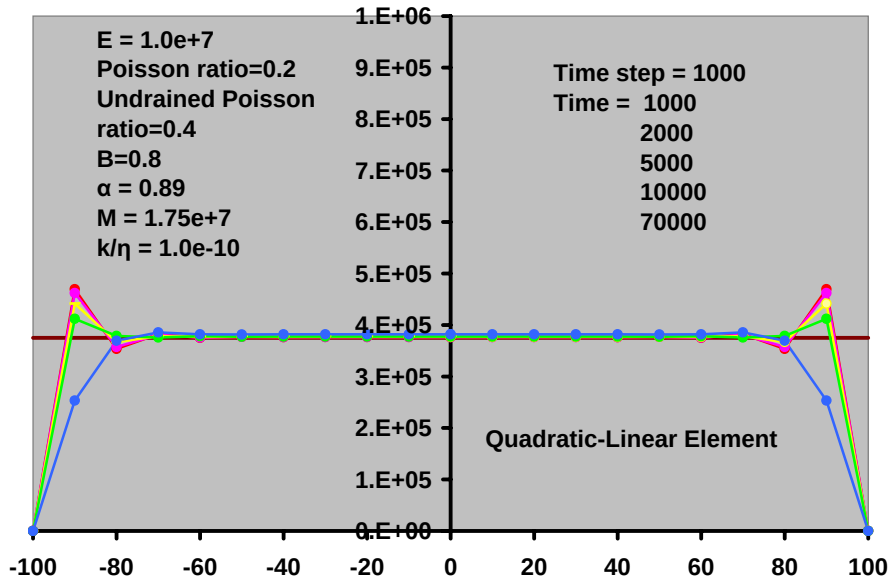

Figure 4.10: CG Solution of Pore Pressure; Compressible Case; Taylor-Hood's Element

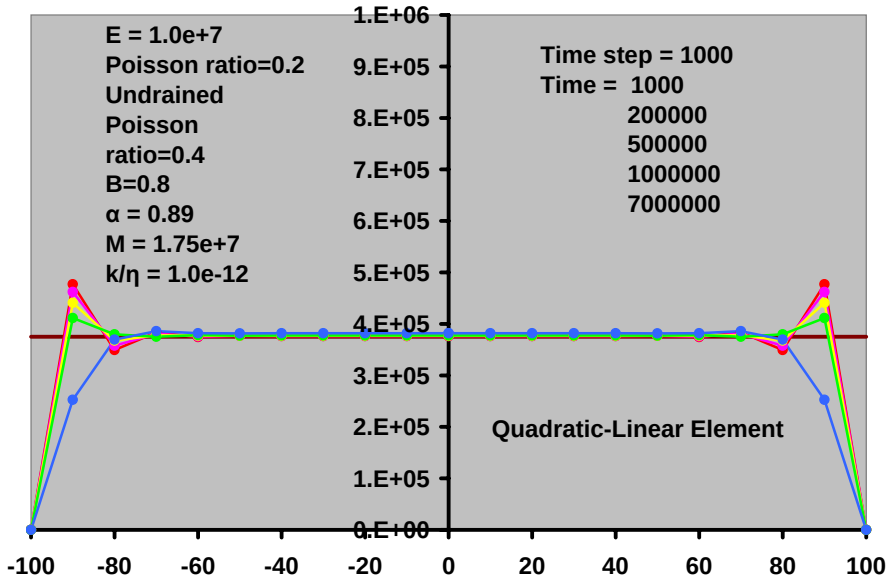

Figure 4.11: CG Solution of Pore Pressure; Compressible Case; Taylor-Hood's Element; Relatively Lower Permeability

they do for unstable methods.

4. For the cases of solid and fluid constituents with larger compressibilities, the element type and permeability do not have obvious effects on the magnitude of oscillations.

5. The decay rate of oscillations depends on permeabilities and not on element types.

4.5 Summary

The performance of popular CG linear-linear finite element method (unstable method) deteriorates whenever a large gradient of pressure or stress exists. CG Taylor-Hood's elements (stable method) also induce nonphysical pressure spikes near boundaries. A similar performance of unstable methods to stable methods is observed for the cases where Biot's modulus is close to the bulk modulus of solid skeletons. More precisely, the term containing Biot's modulus (M) in governing equations for poroelasticity problems is a natural stabilizer to unstable CG finite element schemes. Oscillations in pressure solutions will decay with time. The decay rate of oscillations depends on the magnitude of permeabilities. More precisely, oscillations in problems with high permeability will decay faster than the one with low permeability. Clearly, the decay rate does not depend on finite element schemes.

Chapter 5

Modeling Poroelasticity-II

5.1 Objective

In Chapter 2 and Chapter 3 good performance of DG methods was observed in solving nearly incompressible elasticity and ideal plasticity problems. This motivates us to apply DG theory to poroelasticity problems in order to remove pressure oscillations or at least improve deteriorative CG solutions for cases when zones have low permeability and small time steps are used. In Chapter 4 numerical examples demonstrate that the pressure oscillation does not disappear very fast if zones have very low permeabilities. Thus, it is necessary to remove them at the begining of solutions. In this chapter we present a complete DG finite element formulation for both solid and flow to handle the oscillation problem. The DG formulation for the solid part in poroelasticity systems is easier if the same procedures are followed as those given in Chapter 2. Similar steps to elasticity are also followed for deriving a DG variational formulation for the flow equation. Much effort is, however, required to be invested in coupling terms, which involves physical interpretation on total and effective stresses. After DG formulation, we redo Mandel's problem given and solved by using CG methods in Chapter 4. This time, however, we apply DG methods.

5.2 DG Formulation for Poroelasticity

Here, we assume that a physical subdomain is shared by both solid and fluid. The shared element may have different orders for solid and fluid. Therefore, DG notations defined in Chapter 4 can be fully reused for poroelasticity system. First, let us focus on governing equations for the solid part given in (4.9), which is rewritten here in terms of effective stress and pore pressure as follows

$$\nabla \cdot (\sigma'' - \alpha p I) + f = 0. \tag{5.1}$$

Multiplying (5.1) by v, and integrating by parts, we obtain

$$\int_E (\sigma'' - \alpha p I) : \nabla v dV - \int_{\partial E} ((\sigma'' - \alpha p I) n^s) \cdot v dS = \int_E f \cdot v dV. \tag{5.2}$$

Here, we omit subscript h for both u_h and p_h. Noting that $\sigma''(u){:}\nabla v = \sigma''(u){:}\nabla v^T = \sigma''(u){:}\varepsilon(v)$, we have

$$\begin{gathered} \textstyle\int_E \sigma''(u){:}\varepsilon(v) dV - \int_E (\alpha p I) : \nabla v dV \\ - \textstyle\int_{\partial E} ((\sigma'' - \alpha p) n^s) \cdot v dS = \int_E f \cdot v dV. \end{gathered} \tag{5.3}$$

Also, noting that $(\alpha p I) : \nabla v = \alpha p \nabla \cdot v$, we have

$$\begin{gathered} \textstyle\int_E \sigma''(u){:}\varepsilon(v) dV - \int_E \alpha p \nabla \cdot v dV \\ - \textstyle\int_{\partial E} ((\sigma - \alpha p) n^s) \cdot v dS = \int_E f \cdot v dV. \end{gathered} \tag{5.4}$$

Then, summing over all elements χ, we obtain

$$\begin{gathered} \sum_{E \in \chi} \int_E \sigma''(u){:}\varepsilon(v) dV - \sum_{E \in \chi} \int_E \alpha p \nabla \cdot v dV \\ - \sum \int_{\partial E} ((\sigma'' - \alpha p I) n^s) \cdot v dS = \sum_{E \in \chi} \int_E f \cdot v dV. \end{gathered} \tag{5.5}$$

We now apply the definitions of average and jump terms defined in (2.10)-(2.15)

$$\begin{gathered}\sum_{E\in\chi}\int_E \sigma''(u){:}\varepsilon(v)dV - \sum_{E\in\chi}\int_E \alpha p\nabla\cdot v dV \\ -\sum_{\partial E\in S}\int_{\partial E}\{\sigma'' - \alpha pI\}n^s\cdot[v]dS = \sum_{E\in\chi}\int_E f\cdot v dV + \int_{\Gamma_t} g\cdot v dS.\end{gathered} \tag{5.6}$$

Adding face integrals $\int_{\partial E}\{\sigma''(v)-\alpha PI\}n^s\cdot[u]dS$ and $\frac{\delta_u}{|s|}\int_{\partial E}[u]\cdot[v]dS$ to (5.6), we have

$$\begin{gathered}\sum_{E\in\chi}\int_E \sigma''(u){:}\varepsilon(v)dV - \sum_{E\in\chi}\int_E \alpha p\nabla\cdot v dV \\ -\sum_{\partial E\in S_i+\Gamma_u}\int_{\partial E}\{\sigma''(u) - \alpha pI\}n^s\cdot[v]dS \\ +\sum_{\partial E\in S_i+\Gamma_u}\theta_{DG}\int_{\partial E}\{\sigma''(v) - \alpha PI\}n^s\cdot[u]dS \\ +\sum_{\partial E\in S_i+\Gamma_u}\frac{\delta_u}{|s|}\int_{\partial E}[u]\cdot[v]dS = \sum_{E\in\chi}\int_E f\cdot v dV + \sum_{\partial E\in\Gamma_t}\int_{\partial E}\bar{t}\cdot v dS \\ +\sum_{\partial E\in\Gamma_u}\theta_{DG}\int_{\partial E}\{\sigma''(v) - \alpha PI\}n^s\cdot u_D dS + \sum_{\partial E\in\Gamma_u}\frac{\delta_u}{|s|}\int_{\partial E} u_D\cdot v dS,\end{gathered} \tag{5.7}$$

Where S_i indicates interior faces. Here, the notations S, S_i, Γ_u, and Γ_t imply the interior face and boundary for the elasticity equation. We now limit our attention to a DG formulation for the flow equation given by (4.18). Multiplying (4.18) by w, and integrating by parts

$$\begin{gathered}\alpha\int_E(\nabla\cdot\ \tfrac{\partial u}{\partial t})wdV + \tfrac{1}{M}\int_E\tfrac{\partial p}{\partial t}wdV \\ \int_E(\tfrac{\kappa}{\eta}\nabla p)\cdot\nabla w dV - \int_{\partial E}(\tfrac{\kappa}{\eta}\nabla p)\cdot n^s w dS = \int_E swdV.\end{gathered} \tag{5.8}$$

Then, summing over all elements χ, we obtain

$$\begin{gathered}\sum_{E\in\chi}\alpha\int_E(\nabla\cdot\ \tfrac{\partial u}{\partial t})wdV + \sum_{E\in\chi}\tfrac{1}{M}\int_E\tfrac{\partial p}{\partial t}wdV \\ \sum_{E\in\chi}\int_E(\tfrac{\kappa}{\eta}\nabla p)\cdot\nabla w dV - \sum\int_{\partial E}(\tfrac{\kappa}{\eta}\nabla p)\cdot n^s w dS = \sum_{E\in\chi}\int_E swdV.\end{gathered} \tag{5.9}$$

We now apply the definitions of average and jump terms and have

$$\sum_{E\in\chi}\alpha\int_E(\nabla\cdot\ \tfrac{\partial u}{\partial t})wdV+\sum_{E\in\chi}\tfrac{1}{M}\int_E\tfrac{\partial p}{\partial t}wdV+\sum_{E\in\chi}\int_E(\tfrac{\kappa}{\eta}\nabla p)\cdot\nabla wdV$$
$$-\sum_{\partial E\in S_i+\Gamma_p}\int_{\partial E}\{(\tfrac{\kappa}{\eta}\nabla p)\cdot n^s\}[w]dS=\sum_{E\in\chi}\int_E swdV-\int_{\Gamma_f}\bar{q}wdS. \tag{5.10}$$

Adding fluid boundary integrals $\int_{\partial E}\{(\frac{\kappa}{\eta}\nabla w)\cdot n^s\}[p]dS$ and $\frac{\delta_p}{|s|}\int_{\partial E}[p][w]dS$ to (5.10), we have

$$\begin{aligned}
&\sum_{E\in\chi}\alpha\int_E(\nabla\cdot\ \tfrac{\partial u}{\partial t})wdV+\sum_{E\in\chi}\tfrac{1}{M}\int_E\tfrac{\partial p}{\partial t}wdV\\
&+\sum_{E\in\chi}\int_E(\tfrac{\kappa}{\eta}\nabla p)\cdot\nabla wdV-\sum_{\partial E\in S_i+\Gamma_p}\int_{\partial E}\{(\tfrac{\kappa}{\eta}\nabla p)\cdot n^s\}[w]dS\\
&+\theta_{DG}\sum_{\partial E\in S_i+\Gamma_p}\int_{\partial E}\{(\tfrac{\kappa}{\eta}\nabla w)\cdot n^s\}[p]dS+\sum_{\partial E\in S_i+\Gamma_p}\tfrac{\delta_p}{|s|}\int_{\partial E}[p][w]dS \qquad (5.11)\\
&=\sum_{E\in\chi}\int_E swdV-\sum_{\partial E\in\Gamma_f}\int_{\partial E}\bar{q}wdS\\
&+\theta_{DG}\sum_{\partial E\in\Gamma_p}\int_{\partial E}\{(\tfrac{\kappa}{\eta}\nabla w)\cdot n^s\}[\bar{p}]dS+\sum_{\partial E\in\Gamma_p}\tfrac{\delta_p}{|s|}\int_{\partial E}\bar{p}wdS.
\end{aligned}$$

Here, the notations S, S_i, Γ_p, and Γ_f imply the interior face and pressure and fluid flux boundaries for the flow equation. Introducing shape functions for primary variables u and p interpolated by node values $\bar{u}$ and $\bar{p}$, we have

$$\begin{aligned}
u&=N_u\bar{u},\\
\varepsilon&=B_u\bar{u}\ \ ,\\
p&=N_p\bar{p},
\end{aligned} \tag{5.12}$$

where N_u, B_u, and $N_p$are interpolation matrices and vector for displacement, strain, and pore pressure, respectively. Also, following the same time discretization procedures described in Chapter 4 for (5.11), we obtain algebraic

equations as follows

$$\begin{bmatrix} K_V + K_I & L_V + L_I \\ L_V^T + L_I^T & S_V + \theta\Delta t_k(H_V + H_I) \end{bmatrix} \begin{bmatrix} \bar{u} \\ \bar{p} \end{bmatrix}_{t_k+\Delta t_k} =$$

$$\begin{bmatrix} K_V + K_I & L_V + L_I \\ L_V^T + L_I^T & S_V - (1-\theta)\Delta t_k(H_V + H_I) \end{bmatrix} \begin{bmatrix} \bar{u} \\ \bar{p} \end{bmatrix}_{t_k} + \begin{bmatrix} \frac{dF}{dt} \\ Q \end{bmatrix} \Delta t_k, \tag{5.13}$$

where subscripts V and I indicate the operations of volume and face integration and superscript T means transpose operation. We omit lengthy expressions for submatrices and subvectors in (5.13) in terms of integrals in (5.7) and (5.11). Instead, we give symbolic formats for these matrices as follows

$$K_V = \sum_{E\in\chi}(B_u,\, D)_V, \tag{5.14}$$

$$K_I = \sum_{\partial E\in S}(B_u,\, D,\, n^s,\, \delta_u,\, \theta_{DG})_I, \tag{5.15}$$

$$S_V = \sum_{E\in\chi}(N_p,\, \frac{1}{M})_V, \tag{5.16}$$

$$H_V = \sum_{E\in\chi}(\frac{\kappa}{\eta},\, \nabla N_p)_V, \tag{5.17}$$

$$H_I = \sum_{\partial E\in S}(\frac{\kappa}{\eta},\, \nabla N_p,\, n^s,\, \delta_p,\, \theta_{DG})_I, \tag{5.18}$$

$$L_V = \Sigma_\chi(B_u,\, D,\, \alpha,\, N_p)_V, \tag{5.19}$$

$$L_I = \sum_{\partial E\in S}(N_u,\, N_p,\, \alpha,\, n^s,\, \delta_u,\, \theta_{DG})_I, \tag{5.20}$$

$$\frac{dF}{dt} = \Sigma(f,\, \bar{t},\, N_u,\, n^s,\, \delta_u,\, \theta_{DG})_{V+I}, \tag{5.21}$$

$$Q = \Sigma(s,\, \bar{q},\, N_p,\, n^s,\, \delta_p,\, \theta_{DG})_{V+I}, \tag{5.22}$$

where D is the elasticity tensor. These stiffness matrices and load vectors are functions of the shape function and strain matrix indicated in the brackets in the above equations.

5.3 A Porous Rock Sample in Compression

Following (5.13), we have extended our 3-D nodal-based computer program for elasticity problems to poroelasticity. This has been done by adding code for the flow equation and coupled stiffnesses of flow and solid. In this section we will apply DG to Mandel's problem with rock materials previously solved by CG in Chapter 4. Instead of studying many factors as we did before, we only consider the worst case when the incompressible constituents of fluid and solid are assumed and the media are of very low permeability. The geometry, meshing, and material behavior in this problem are the same. We use linear DG elements for both displacement and pressure. The pressure distribution from the left to the right predicted by the DG method (IIPG) is indicated by the green line in Figure 5.1. Figure 5.1 also shows the corresponding CG solution which is flagged by the red line. We see that a very small error in the pressure field obtained from DG is restricted in portions very close to the two ends. In other words, the pressure is not polluted over the whole domain as the CG solution. The performance of DG method is almost perfect for this problem and even much better than stable CG methods if we carefully compare Figure 5.1 with Figure 4.6.

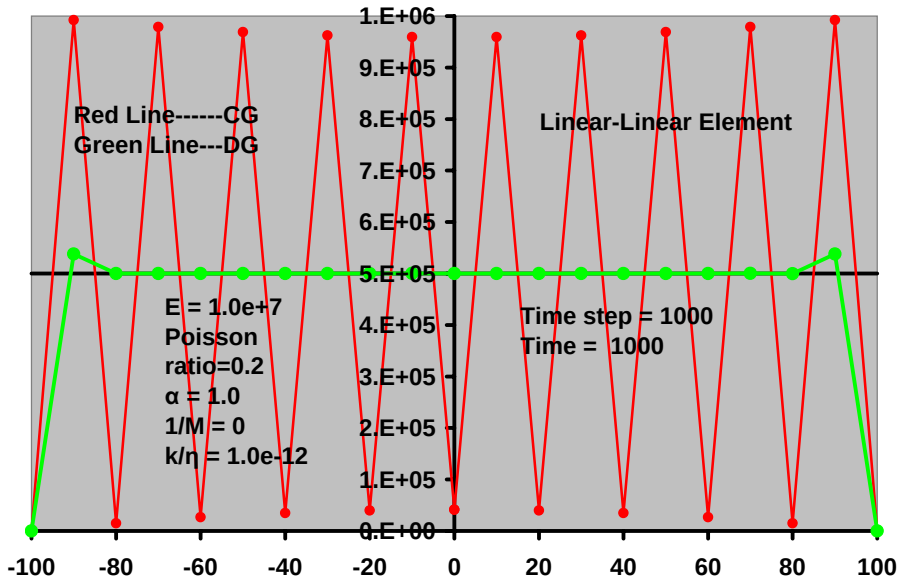

Figure 5.1: Pressure Distributions of DG and CG Solutions of Mandel's Problem

Property	Bone (PLC)	Marble	Granites	Sandstones
shear modulus (Gpa)	5	24	15-19	4.2-13
drained Poisson ratio	0.32	0.25	0.25-0.27	0.12-0.2
undrained Poisson ratio	0.33	0.27	0.30-0.34	0.28-0.33
drained bulk modulus (Gpa)	12	40	24-35	4.6-13
undrained bulk modulus (Gpa	13	44	41-42	1.3-30
compressibility coefficient	0.4	0.51	0.58-0.85	0.5-0.88
bulk modulus of the solid (Gpa)	14	50	45	31-42
Biot's constant (α)	0.14	0.19	0.27-0.47	0.65-0.85
porosity	0.05	0.02	0.01-0.02	0.02-0.26
specific permeability($m^2 \times 10^{-20}$)	1.5	10	10-40	$2\times10^4 - 8 \times 10^7$

Table 5.1: Mechanical Properties of Bone and Rock (S. Cowin, Bone Poroelasticity, J. of Biomechanics, 32 vol., 1999)

5.4 A Lacunar Bone Sample in Compression

Modeling bone problems by using poroelasticity theory is of current interest in biomedical engineering. There are two main types of bones, i.e., vascular and lacunar-canalicular bones. Bones have much lower permeabilities than sandstones. Table 5.1 presents the material behaviors of rocks and lacunar bones.

Contrary to sandstones, bones have extremely low permeability. Lacunar bones (PLC) even have much lower permeability than marble. The low permeability of lacunar bones brings a challenge for CG finite element methods. In this section, we study a lacunar bone sample under compression test also modeled by Mandel's problem. We replace rock materials by lacunar bones. Now, the unit for the size of rock problems given in Chapter 4 changes from m to mm for bone samples. We take shear modulus $G = 13.2$ GPa,

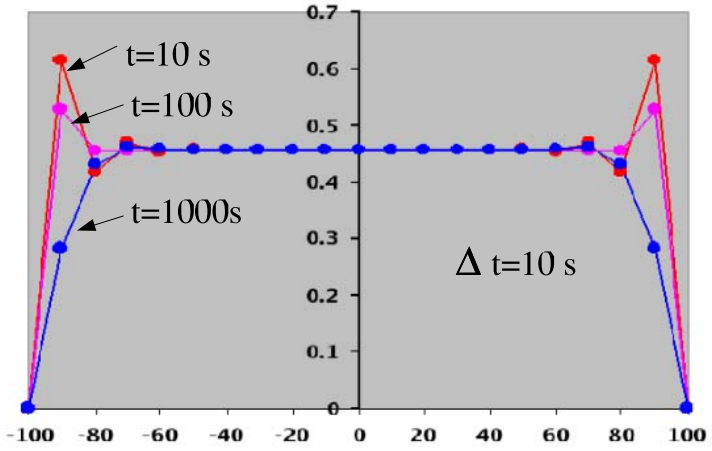

Figure 5.2: Pressure Distributions of DG and CG Solutions of Bone Problem

Biot modulus $M = 50$ Gpa, Biot's constant 0.4, drained Poisson ratio 0.32, undrained Poisson's ratio 0.33, and permeability $1.5 \times 10^{-18} m^2/pa.s$. The time step is taken as 10 seconds. Figure 5.2 shows pressure distributions predicted by the CG method. Again, spikes near the two ends indicate nonphysical oscillations of pressure. These spikes become smaller following the lapse of time. Pressure results predicted by DG simulation is given in Figure 5.3. Only pressure distributions for both DG and CG at first time step are presented and compared. Again, the performance of the DG method (IIPG) is perfect for this bone problem.

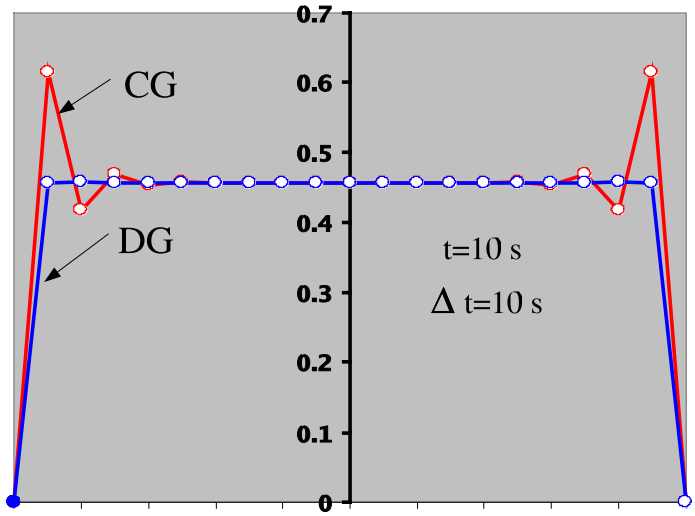

Figure 5.3: Pressure Distributions of DG and CG Solutions of Bone Problem

5.5 Summary

We have presented a formulation of DG for coupled problems of solid and flow. A 3-D nodal-based DG program is implemented. Numerical examples demonstrated that DG methods are able to remove or greatly alleviate pressure oscillations induced by CG methods. More importantly, large errors resulting from DG methods at regions of large gradients of pressure and stress do not freely propagate into the whole domain. The localization of errors is one of the most attractive advantage of DG over CG methods.

Chapter 6

Modeling Poroelasticity-III

6.1 Objective

In previous chapters finite element methods for both solid and flow equations are studied. Noting that in practical applications finite difference methods are widely used for solving fluid flow problems, we choose to solve the flow equation in the poroelasticity system using a finite difference method rather than finite element methods. In fact, IPARS [116], a finite difference based computer software, has been developed at the Center of Subsurface Modeling in the Institute for Computational Engineering and Sciences, the University of Texas at Austin. It is attractive especially for large scale practical applications. However, a similar pressure oscillation to CG methods also happens in finite difference solutions for flow with low permeability, which will be shown in Section 6.3 in this chapter. This motivates us to apply DG methods for solid part but keep finite difference schemes for flow in order to remove pressure oscillations. In this chapter we briefly introduce cell-centered finite difference schemes (CCFD) for a 2-D flow equation. Then, a formulation for coupling terms, which involves DG finite element spaces for displacement and piece-wise constant approximation for pore pressure, is derived. Based on DG theory for solid and cell-centered finite differences for flow, a 2-D computer pro-

gram has been implemented for poroelasticity problems. A beam with porous media is solved using CG and DG for solid and CCFD for flow. Numerical study demonstrates that DG is powerful in removing pressure oscillations.

6.2 CCFD for Flow

First, we limit our attention to a 2-D flow equation given by [106]

$$-\nabla \cdot (\frac{\kappa}{\eta}\nabla p) = s. \tag{6.1}$$

Let a rectangular domain be $(a,b)\times(c,d)$, (x,y)$\in(a,b)\times(c,d)$, and permeability tensor $\frac{\kappa}{\eta}$ be a diagonal matrix

$$\frac{\kappa}{\eta} = \begin{pmatrix} \kappa_{11}(x,y) & 0 \\ 0 & \kappa_{22}(x,y) \end{pmatrix}. \tag{6.2}$$

Using (6.2), (6.1) can be expanded into

$$-\left(\frac{\partial}{\partial x}((\kappa_{11}(x,y)\frac{\partial p}{\partial x} + \frac{\partial}{\partial y}((\kappa_{22}(x,y)\frac{\partial p}{\partial y}\right) = s(x,y), \tag{6.3}$$

with Dirichlet boundary conditions

$$\begin{aligned} p(x,y)\mid_{x=a} &= p_a(y), \\ p(x,y)\mid_{x=b} &= p_b(y), \\ p(x,y)\mid_{y=c} &= p_c(x), \\ p(x,y)\mid_{y=d} &= p_d(x), \end{aligned} \tag{6.4}$$

where $p_a(y)$, $p_b(y)$, $p_c(x)$,and $p_d(x)$ are prescribed pressures, or with Neumann Boundary conditions

$$\begin{aligned}
-\kappa_{11}(x,y)\tfrac{\partial p(x,y)}{\partial x} \mid_{x=a} &= q_a(y),\\
-\kappa_{11}(x,y)\tfrac{\partial p(x,y)}{\partial x} \mid_{x=b} &= q_b(y),\\
-\kappa_{22}(x,y)\tfrac{\partial p(x,y)}{\partial y} \mid_{y=c} &= q_c(x),\\
-\kappa_{22}(x,y)\tfrac{\partial p(x,y)}{\partial y} \mid_{y=d} &= q_d(x),
\end{aligned} \tag{6.5}$$

where $q_a(y)$, $q_b(y)$, $q_c(x)$,and $q_d(x)$ are prescribed fluid fluxes. A non-uniform rectangular mesh $\Delta_x \times \Delta_y$ is given by

$$\begin{aligned}
\Delta_x : &\quad a = x_0 < x_1 < \cdots < x_{n-1} < x_M = b,\\
\Delta_y : &\quad c = y_0 < y_1 < \cdots < y_{n-1} < y_N = d,
\end{aligned} \tag{6.6}$$

and we define

$$\begin{aligned}
x_{i+\frac{1}{2}} = \tfrac{1}{2}(x_i + x_{i+1}); \quad p_{i+\frac{1}{2}} = \tfrac{1}{2}(p_i + p_{i+1}) \quad i = 0, 1, 2, \cdots, M-1,\\
y_{j+\frac{1}{2}} = \tfrac{1}{2}(y_j + y_{j+1}); \quad p_{j+\frac{1}{2}} = \tfrac{1}{2}(p_j + p_{j+1}) \quad j = 0, 1, 2, \cdots, N-1.
\end{aligned} \tag{6.7}$$

Using the above definitions and (6.7), (6.3) can be discretized into

$$\begin{aligned}
&-\tfrac{1}{x_{i+1}-x_i}\left(-\kappa(x_{i+1}, y_{j+\frac{1}{2}})\tfrac{p_{i+1\frac{1}{2},j+\frac{1}{2}} - p_{i+\frac{1}{2},j+\frac{1}{2}}}{x_{i+\frac{3}{2}} - x_{i+\frac{1}{2}}}\right.\\
&\qquad\left.-\kappa_{11}(x_i, y_{j+\frac{1}{2}})\tfrac{p_{i+\frac{3}{2},j+\frac{1}{2}} - p_{i+\frac{1}{2},j+\frac{1}{2}}}{x_{i+\frac{3}{2}} - x_{i+\frac{1}{2}}}\right)\\
&-\tfrac{1}{y_{j+1}-y_j}\left(\kappa_{22}(x_{i+\frac{1}{2}}, y_{j+1})\tfrac{p_{i+\frac{1}{2},j+1\frac{1}{2}} - p_{i+\frac{1}{2},j+1}}{y_{j+1\frac{1}{2}} - y_{j+\frac{1}{2}}}\right.\\
&\left.-\kappa_{22}(x_{i+\frac{1}{2}}, y_j)\tfrac{p_{i+\frac{1}{2},j+\frac{1}{2}} - p_{i+\frac{1}{2},j-\frac{1}{2}}}{y_{j+\frac{1}{2}} - y_{j-\frac{1}{2}}}\right) = s(x_{i+\frac{1}{2}}, y_{j+\frac{1}{2}}),
\end{aligned} \tag{6.8}$$

where $i = 1, 2, \cdots, M-2$ and $j = 1, 2, \cdots, N-2$. For Neumann boundary conditions we have

$$\begin{aligned}
-\kappa_{11}(x_0, y_{j+\frac{1}{2}})\frac{p_{\frac{1}{2},j+\frac{1}{2}} - p_{-\frac{1}{2},j+\frac{1}{2}}}{x_{\frac{1}{2}} - x_{-\frac{1}{2}}} &= q_a(y_{j+\frac{1}{2}}) \quad for\, i = 0, \\
-\kappa_{11}(x_M, y_{j+\frac{1}{2}})\frac{p_{M+\frac{1}{2},j+\frac{1}{2}} - p_{M-\frac{1}{2},j+\frac{1}{2}}}{x_{\frac{1}{2}} - x_{-\frac{1}{2}}} &= q_b(y_{j+\frac{1}{2}}) \quad for\, i = M-1, \\
-\kappa_{22}(x_{i+\frac{1}{2}}, y_0)\frac{p_{i+\frac{1}{2},\frac{1}{2}} - p_{i+\frac{1}{2},-\frac{1}{2}}}{y_{\frac{1}{2}} - y_{-\frac{1}{2}}} &= q_c(x_{i+\frac{1}{2}}) \quad for\, j = 0, \\
-\kappa_{22}(x_{i+\frac{1}{2}}, y_N)\frac{p_{i+\frac{1}{2},N+\frac{1}{2}} - p_{i+\frac{1}{2},N-\frac{1}{2}}}{y_{N+\frac{1}{2}} - y_{N-\frac{1}{2}}} &= q_d(x_{i+\frac{1}{2}}) \quad for\, j = N-1.
\end{aligned} \tag{6.9}$$

For Dirichlet boundary conditions we have

$$\begin{aligned}
&-\frac{1}{x_{i+1} - x_0}\Big(-\kappa_{11}(x_1, y_{j+\frac{1}{2}})\frac{p_{\frac{3}{2},j+\frac{1}{2}} - p_{\frac{1}{2},j+\frac{1}{2}}}{x_{\frac{3}{2}} - x_{\frac{1}{2}}} - \kappa_{11}(x_0, y_{j+\frac{1}{2}})\frac{p_{\frac{1}{2},j+\frac{1}{2}} - p_a(y_{j+\frac{1}{2}})}{x_{\frac{1}{2}} - x_0}\Big) \\
&-\frac{1}{y_{j+1} - y_j}\Big(\kappa_{22}(x_{\frac{1}{2}}, y_{j+1})\frac{p_{\frac{1}{2},j+\frac{3}{2}} - p_{\frac{1}{2},j+\frac{1}{2}}}{y_{j+\frac{3}{2}} - y_{j+\frac{1}{2}}} - \kappa_{22}(x_{\frac{1}{2}}, y_j)\frac{p_{\frac{1}{2},j+\frac{1}{2}} - p_{\frac{1}{2},j-\frac{1}{2}}}{y_{j+\frac{1}{2}} - y_{j-\frac{1}{2}}}\Big) = s(x_{\frac{1}{2}}, y_{j+\frac{1}{2}}),
\end{aligned} \tag{6.10}$$

for $i = 1$ and $j = 1, 2, \cdots, N-2$, and

$$\begin{aligned}
&-\frac{1}{x_{M+1} - x_{M-1}}\Big(-\kappa_{11}(x_M, y_{j+\frac{1}{2}})\frac{p_b(y_{j+\frac{1}{2}}) - p_{M-\frac{1}{2},j+\frac{1}{2}}}{x_M - x_{M-\frac{1}{2}}} - \kappa_{11}(x_{M-1}, y_{j+\frac{1}{2}}) \\
&\frac{p_{M-\frac{1}{2},j+\frac{1}{2}} - p_{M-\frac{3}{2},j+\frac{1}{2}}}{x_{M-\frac{1}{2}} - x_{M-\frac{3}{2}}}\Big) - \frac{1}{y_{j+1} - y_j}\Big(\kappa_{22}(x_{M-\frac{1}{2}}, y_{j+1}) \\
&\frac{p_{M-\frac{1}{2},j+\frac{3}{2}} - p_{M-\frac{1}{2},j+\frac{1}{2}}}{y_{j+\frac{3}{2}} - y_{j+\frac{1}{2}}} - \kappa_{22}(x_{M-\frac{1}{2}}, y_j)\frac{p_{M-\frac{1}{2},j+\frac{1}{2}} - p_{M-\frac{1}{2},j-\frac{1}{2}}}{y_{j+\frac{1}{2}} - y_{j-\frac{1}{2}}}\Big) = s(x_{M-\frac{1}{2}}, y_{j+\frac{1}{2}}),
\end{aligned} \tag{6.11}$$

for $i = M-1$ and $j = 1, 2, \cdots, N-2$. Similarly, we have Dirichlet boundary conditions for $j = 0$ and $j = N-1$. For the term $\frac{1}{M}\frac{\partial p}{\partial t}$ in (4.18) we will have diagonal mass matrices S since piece-wise constant pressure approximation

is used. After discretization in the time domain, we have similar algebraic equations to CG finite element methods given in chapter 4 and chapter 5

$$\begin{bmatrix} K & L \\ L^T & \S + \theta\Delta t_k H \end{bmatrix} \begin{Bmatrix} \overline{u} \\ \overline{p} \end{Bmatrix}_{t_k+\Delta t_k} = \begin{bmatrix} K & L \\ L^T & S - (1-\theta)\Delta t_k H \end{bmatrix} \begin{Bmatrix} \overline{u} \\ \overline{p} \end{Bmatrix}_{t_k+\Delta t_k} + \begin{Bmatrix} \frac{d\hat{f}}{dt} \\ \hat{q} \end{Bmatrix} \Delta t, \tag{6.12}$$

where stiffness K for elasticity obtained from DG formulation is similar to the one given in Chapter 4 . Stiffness H for flow can be easily obtained using those CCFD results given by (6.8)-(6.11). The coupling matrix L is

$$L = \sum_{E\in\chi} \int_E B_u^T D\vec{\alpha} N_p d\Omega + L_I = \sum_{E\in\chi} \int_E B_u^T D\vec{\alpha} d\Omega + L_I, \tag{6.13}$$

where L_I is coupling edge stiffness of solid and fluid. A 2-D computer program has been implemented for DG for solid and CCFD for flow and below we apply this scheme to poroelasticity problems.

6.3 Numerical Study

In this section we study a cantilever bracket problem similar to the one given and solved in previous chapters. The configuration of this bracket is shown in Figure 6.1. Plane strain is assumed. A uniform square mesh is used. The pressures at colored points will be output and visualized. Linear elements are used for the solid part. We study two cases, high and low permeabilities.

First, we study the case with high permeability. Figure 6.2 presents pressure distributions along bracket cross-section from the top to the bottom

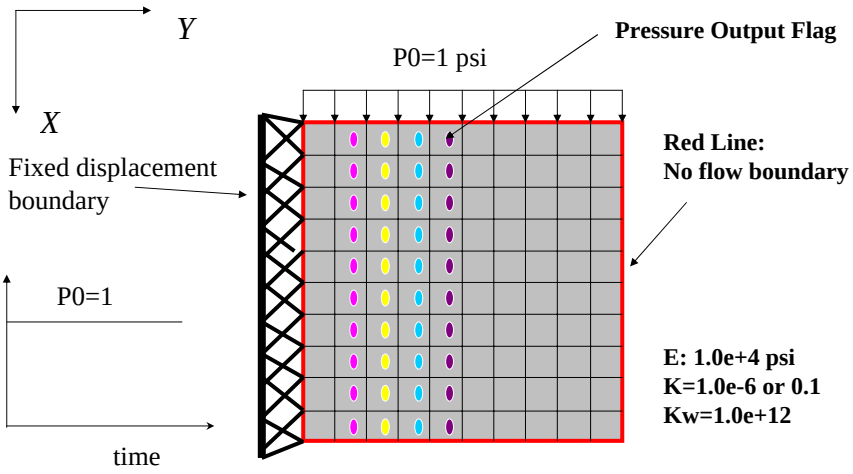

Figure 6.1: A Cantilever Bracket Problem

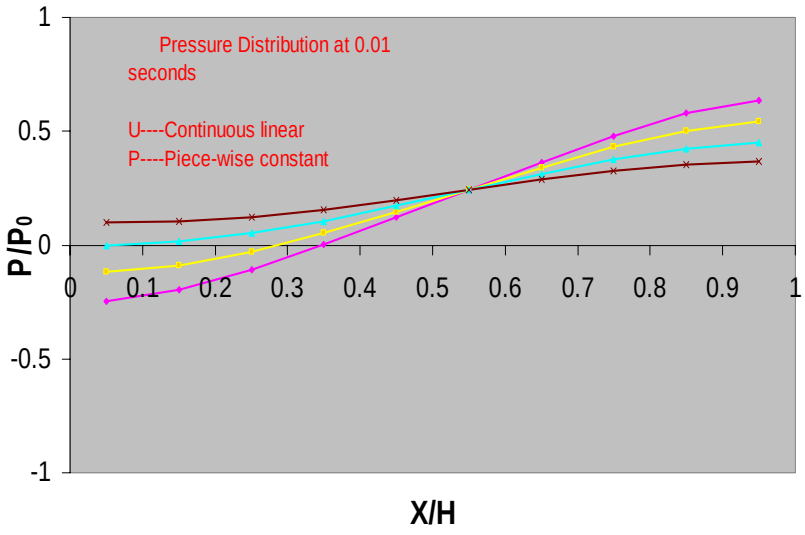

Figure 6.2: Pressure Distribution of CG-CCFD Solution at Earlier Stage for Cantilever Bracket Problem with High Permeability.

at an earlier stage. They are obtained by using CG scheme for solid and CCFD for flow. More precisely, a smooth pressure field is observed. This shows that this CG scheme works very well for problems with high permeability.

We now change permeability from 0.1 to $1.0e-10$ and still apply CG method for solid. The pressure results at an earlier stage are shown in Figure 6.3. We see that a serious pressure oscillation occurs in the whole cross-sections and CG method can not handle problems with low permeability.

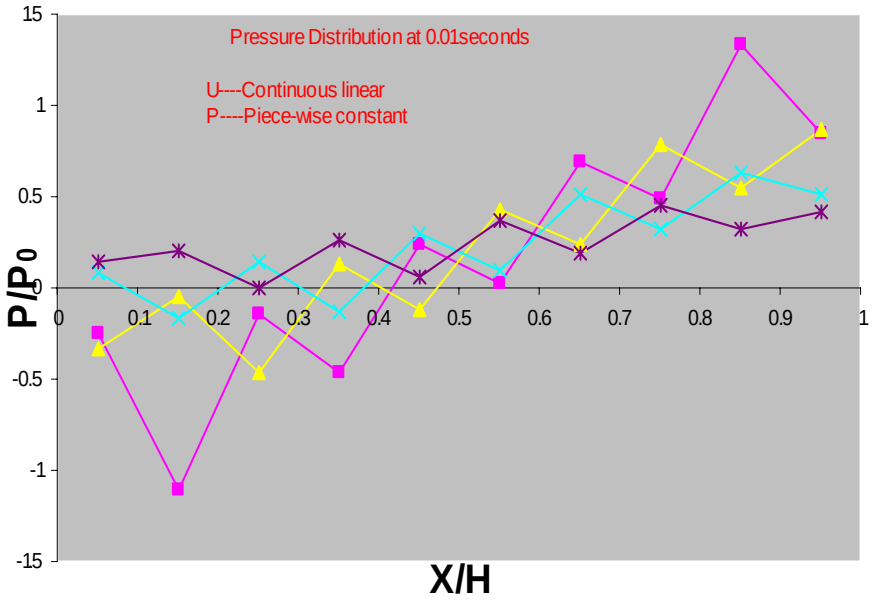

Figure 6.3: Pressure Distribution of CG-CCFD Solution at Earlier Stage for Cantilever Bracket Problem with Low Permeability.

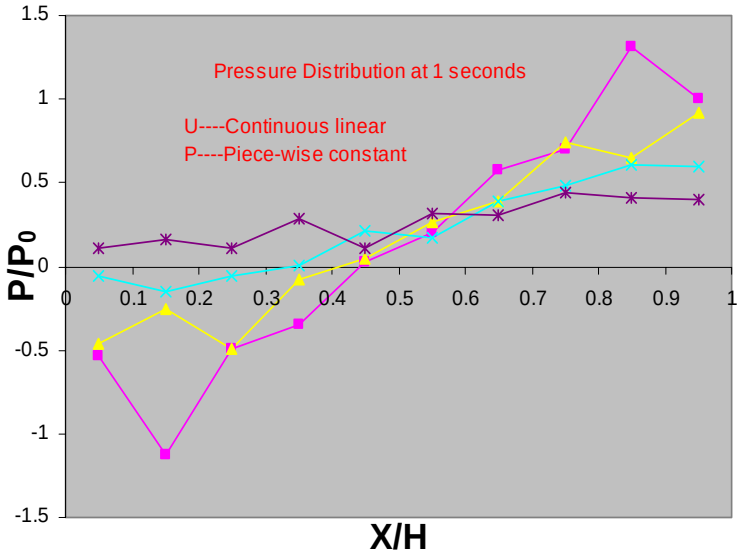

Figure 6.4: Pressure Distribution of CG-CCFD Solution at Longer time for Cantilever Bracket Problem with Low Permeability.

Figure 6.4 shows the pressure distributions at a late stage, which the oscillation tends to decay following the lapse of time.

Figure 6.5 shows a pressure contour over the whole domain. It is clear that the pressure solution from CG oscillates over the whole domain.

We now apply DG methods to this low permeability case. Figure 6.6 shows smooth pressure distributions for DG methods.

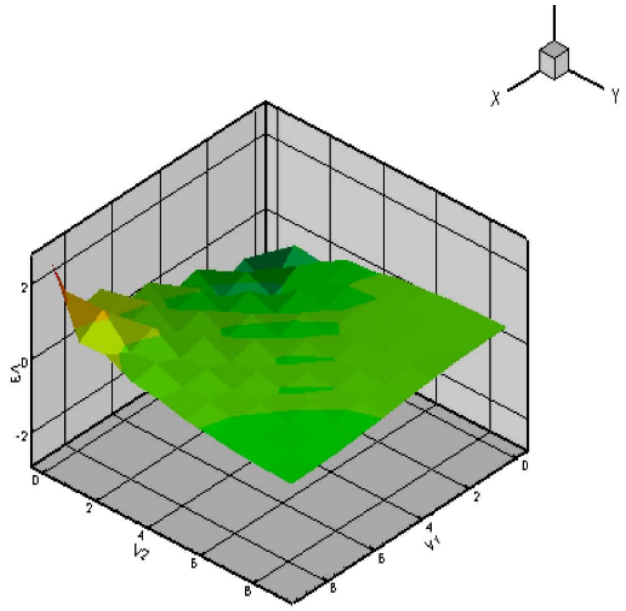

Figure 6.5: Pressure Contour of CG-CCFD Solution at Earlier Stage for Cantilever Bracket Problem with Low Permeability.

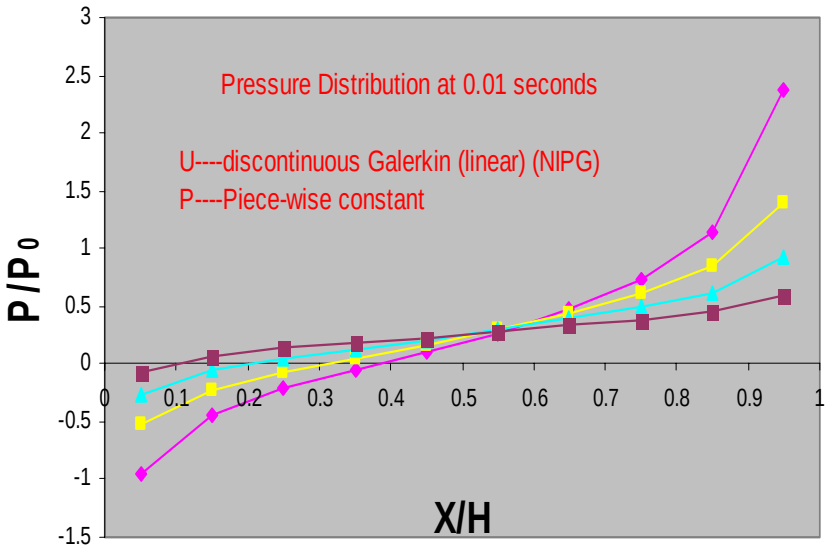

Figure 6.6: Pressure Distribution of DG-CCFD Solution at Earlier Stage for Cantilever Bracket Problem with Low Permeability.

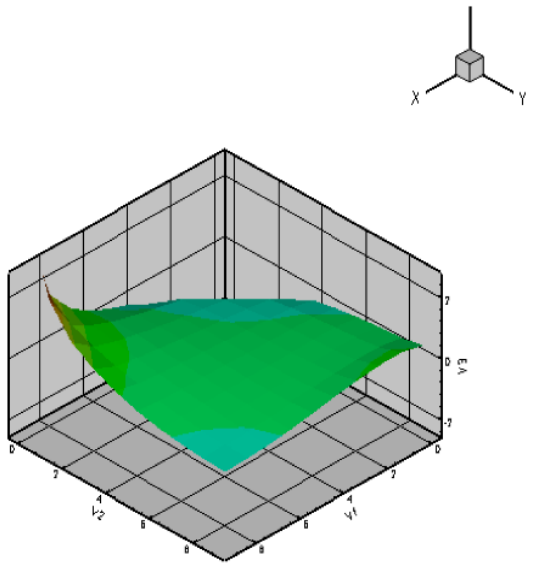

Figure 6.7: Pressure Contour of DG-CCFD Solution at Earlier Stage for Cantilever Bracket Problem with Low Permeability.

Also, a pressure contour for DG over the whole domain is shown in Figure 6.7. A very smooth pressure field over the whole domain is observed. We conclude that DG for solid is robust in dealing with poroelasticity problems with low permeability even when finite difference methods are used for flow.

6.4 Summary

We have presented a scheme of CCFD for flow and DG for elasticity. This scheme is very robust in dealing with problems with low permeability in that it obtains a smooth pressure field and doesn't induce any nonphysical oscillation in pressure solution as CG methods.

Chapter 7

Modeling Thermoporoelastoplasticity

7.1 Objective

In this chapter, we extend DG theory to thermoporoelastoplasticity problems, which are called 3-field problems. This has been done by adding a thermal effect to poroplasticity equations. The thermal effect includes both conduction and convection. It is particularly important to modeling fluid injection problems in petroleum engineering [21, 24]. For example, unlike a production well, a fluid injection well involves a non-isothermal process. The thermal field is mainly controlled by the movement of injected fluids and thus convection dominates the thermal process. This is due to very low thermal conductivities in rocks. The temperature front resulting from this convection dominated effect is considerably sharp. Convection not only brings a nonlinearity but also results in a heterogeneity to temperature field even if the conductivity is homogeneous over the whole domain. It is difficult to solve this dynamic heterogeneity system by CG methods. Small time steps are required in order to obtain convergent solutions for solving the thermal equations when considering the convection effect. However, the use of a small time step in CG methods often induces nonphysical pressure and temperature oscillations for cases with low conductivity. We propose DG to handle these challenges.

7.2 Three-Field Theory

7.2.1 Governing Equations

Thermoporoelastoplasticity involves three fields, i.e. displacement field (u) for solid skeleton, pore pressure field (p) for fluid flow, and temperature field (T) for heat transfer. In poroelasticity theory the total stress consists of effective stress and pore pressure. Therefore, any reduction in fluid pressure will, in general, result in a growth in effective stress, which is the actual stress taken by the solid skeleton. Temperature change results in the expansion and contraction of the solid skeleton. Howerver, Biot's effective stress formula is still valid when considering thermal effects as follows:

$$\sigma = \sigma'' - \alpha p I, \tag{7.1}$$

where σ, σ'', and p are total stress tensor, effective stress tensor, and scalar pore pressure. Using (7.1), we obtain the linear momentum equation as follows:

$$\nabla \cdot \sigma + f = \nabla \cdot (\sigma'' - \alpha p I) + f = \nabla \cdot \sigma'' - \alpha \nabla p + f = 0. \tag{7.2}$$

A thermal effect can be easily obtained for Biot's flow theory (4.18) in the form

$$\alpha \frac{\partial (\nabla \cdot u)}{\partial t} + \frac{1}{M} \frac{\partial p}{\partial t} - \alpha_m \frac{\partial T}{\partial t} - \nabla \cdot (K_p \nabla p) = q_p, \tag{7.3}$$

where α_m is the thermal expansion coefficient of the fluids. Particularly, T is the increase in the temperature over the initial isothermal equilibrium state. The thermal energy transport equation has been formulated and derived in [30, 62]. It can be written as follows

$$\alpha_T \frac{\partial T}{\partial t} + \alpha_p T \frac{\partial p}{\partial t} - \nabla \cdot (K_T \nabla T + \alpha_c T K_p \nabla p) = q_T, \tag{7.4}$$

where the parameter α_T is the heat capacity of porous media, K_T is the thermal conductivity tensor of porous media, α_c is the heat convective capacity of fluids, and v is fluid velocity. More detailed relations among coefficients in the above governing equations can be found in [30, 62]. Here, we assume that the deformation of solid skeletons does not affect the thermal field

7.2.2 Constitutive Equations

In this section we discuss a few associated relations between stress and strain, fluid flux and pressure, and heat flux and temperature. As discussed in previous chapters, the relationship between fluid flux and pressure is described by Darcy's law

$$Q_p = -K_p \nabla p. \tag{7.5}$$

Also, we state Fourier's law which describes the relationship between heat flux and temperature as follows

$$Q_T = -(K_T \nabla T + \alpha_c T K_p \nabla p), \tag{7.6}$$

where both conduction and convection effects are taken into account. Next, we derive the relationship between evolutionary effective stress tensor and evolutionary strain tensor that includes the effect of thermal strain. Again, we have yielding function Y and consistency condition discussed in Chapter 3

$$\dot{Y} = \frac{\partial Y}{\partial \sigma''} : \dot{\sigma''} + \frac{\partial Y}{\partial \vartheta} \frac{\partial \vartheta}{\partial \epsilon^p} : \dot{\epsilon}^p = 0. \tag{7.7}$$

The plastic flow rule is given by

$$\dot{\epsilon}^p = \dot{\gamma} \frac{\partial F}{\partial \sigma''}. \tag{7.8}$$

Inserting (7.8) into (7.7), we have:

$$\frac{\partial Y}{\partial \sigma''} : \dot{\sigma''} = -\dot{\gamma}\frac{\partial Y}{\partial \vartheta}\frac{\partial \vartheta}{\partial \epsilon^p} : \frac{\partial F}{\partial \sigma''}. \tag{7.9}$$

The additive decomposition of strain tensor is:

$$\dot{\epsilon} = \dot{\epsilon}^e + \dot{\epsilon}^p + \alpha_E \dot{T} I, \tag{7.10}$$

where α_E is thermal expansion coefficient and assumed to be constant. I is the identity tensor. $\dot{\epsilon}^e$ is the additive elastic strain tensor that already excludes the thermal part and can be used to compute the rate of change of stress. Thus, we have

$$\dot{\epsilon} = \dot{\epsilon}^e + \dot{\epsilon}^p + \alpha_E \dot{T} I = D^{-1}\dot{\sigma''} + \dot{\gamma}\frac{\partial F}{\partial \sigma''} + \alpha_E \dot{T} I. \tag{7.11}$$

Multiplying (7.11) by the elasticity tensor D and taking an inner product with $\frac{\partial Y}{\partial \sigma''}$, we have:

$$\frac{\partial Y}{\partial \sigma''} : D\dot{\epsilon} = \frac{\partial Y}{\partial \sigma''} : \dot{\sigma''} + \dot{\gamma}\frac{\partial Y}{\partial \sigma''} : D\frac{\partial F}{\partial \sigma''} + \alpha_E \dot{T}\frac{\partial Y}{\partial \sigma''} : DI \tag{7.12}$$

Inserting (7.9) into (7.12), we have

$$\frac{\partial Y}{\partial \sigma''} : D\dot{\epsilon} = -\dot{\gamma}\frac{\partial Y}{\partial \vartheta}\frac{\partial \vartheta}{\partial \epsilon^p} : \frac{\partial F}{\partial \sigma''} + \dot{\gamma}\frac{\partial Y}{\partial \sigma''} : D\frac{\partial F}{\partial \sigma''} + \alpha_E \dot{T}\frac{\partial Y}{\partial \sigma''} : DI \tag{7.13}$$

Therefore, the flow scalar parameter $\dot{\gamma}$ can be derived from (7.13):

$$\dot{\gamma} = \frac{\frac{\partial Y}{\partial \sigma''} : D\dot{\epsilon} - \alpha_E \dot{T}\frac{\partial Y}{\partial \sigma''} : DI}{\frac{\partial Y}{\partial \sigma''} : D\frac{\partial F}{\partial \sigma''} - \frac{\partial Y}{\partial \vartheta}\frac{\partial \vartheta}{\partial \epsilon^p} : \frac{\partial F}{\partial \sigma''}}. \tag{7.14}$$

(7.11) can be rewritten as follows:

$$D\dot{\epsilon} = \dot{\sigma''} + \dot{\gamma} D\frac{\partial F}{\partial \sigma''} + \alpha_E \dot{T} DI. \tag{7.15}$$

Inserting (7.14) into (7.15) we have:

$$D\dot{\epsilon} = \dot{\sigma''} + \frac{\frac{\partial Y}{\partial \sigma''} : D\dot{\epsilon} - \alpha_E \dot{T} \frac{\partial Y}{\partial \sigma''} : DI}{\frac{\partial Y}{\partial \sigma''} : D\frac{\partial F}{\partial \sigma''} - \frac{\partial Y}{\partial \vartheta}\frac{\partial \vartheta}{\partial \epsilon^p} : \frac{\partial F}{\partial \sigma''}} D\frac{\partial F}{\partial \sigma''} + \alpha_E \dot{T} DI. \tag{7.16}$$

Reorganizing (7.16), we obtain

$$\dot{\sigma''} = \{D - \frac{D\frac{\partial F}{\partial \sigma''} \bigotimes D\frac{\partial Y}{\partial \sigma''}}{\frac{\partial Y}{\partial \sigma''} : D\frac{\partial F}{\partial \sigma''} - \frac{\partial Y}{\partial \vartheta}\frac{\partial \vartheta}{\partial \epsilon^p} : \frac{\partial F}{\partial \sigma''}}\}(\dot{\epsilon} - \alpha_E \dot{T} I) \tag{7.17}$$

or

$$\dot{\sigma''} = \dot{\sigma'} - D_T \dot{T}, \tag{7.18}$$

where

$$\dot{\sigma'} = D^{ep}\dot{\epsilon}, \tag{7.19}$$

$$D^{ep} = D - \frac{D\frac{\partial F}{\partial \sigma''} \bigotimes D\frac{\partial Y}{\partial \sigma''}}{\frac{\partial Y}{\partial \sigma''} : D\frac{\partial F}{\partial \sigma''} - \frac{\partial Y}{\partial \vartheta}\frac{\partial \vartheta}{\partial \epsilon^p} : \frac{\partial F}{\partial \sigma''}}, \tag{7.20}$$

$$D_T = \alpha_E D^{ep} I. \tag{7.21}$$

We call σ' nominal effective stress.

7.2.3 Boundary and Initial Conditions

For 3-field problems, boundary conditions are relatively complex. Figure 7.1 (a) indicates boundary conditions for the solid equation, Figure 7.1 (b) for fluid flow equation , and Figure 7.1 (c) for thermal equation. For a given domain Ω and its whole boundary $\partial\Omega$ we have

$$\begin{gathered}\Gamma_u + \Gamma_t = \partial\Omega,\ \Gamma_u \cap \Gamma_t = \emptyset, \\ \Gamma_p + \Gamma_f = \partial\Omega,\ \Gamma_p \cap \Gamma_f = \emptyset, \\ \Gamma_T + \Gamma_h = \partial\Omega,\ \Gamma_T \cap \Gamma_h = \emptyset.\end{gathered} \tag{7.22}$$

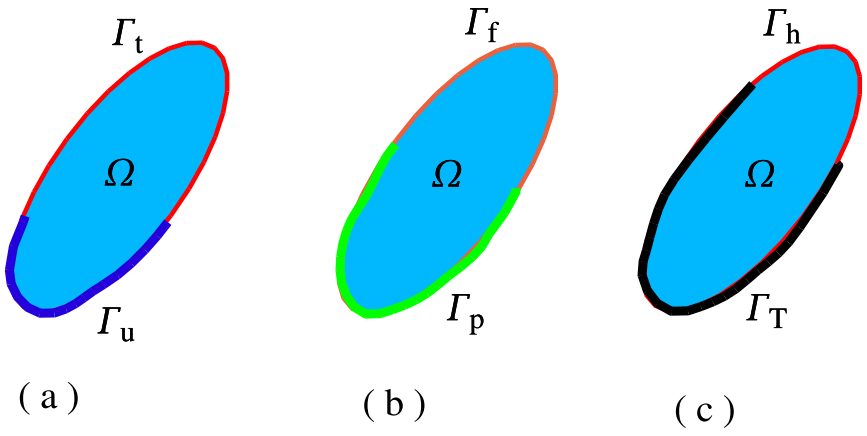

Figure 7.1: Dirichlet and Neumann Boundaries of the 3-Field Problems

Boundary conditions for solid skeleton are

$$\begin{aligned} u(x,t) &= \bar{u}(x,t),\ (x,t) \in \Gamma_u \times (0,\infty), \\ (\sigma'' - \alpha p I)n &= \bar{t}(x,t),\ (x,t) \in \Gamma_{t_1} \times (0,\infty), \\ (\sigma'' - \alpha p I)n &= -pn(x,t),\ (x,t) \in \Gamma_{t_2} \times (0,\infty), \end{aligned} \tag{7.23}$$

where n is the normal vector of boundary surfaces, Γ_{t_1} is the traction boundary with given tractions, Γ_{t_2} is the traction boundary with unknown pressure (for well inner boundary). Boundary conditions for fluid flow are

$$\begin{aligned} p(x,t) &= \bar{p}(x,t),\ (x,t) \in \Gamma_p \times (0,\infty), \\ -(K_p \nabla p) \cdot n &= \bar{f}_p(x,t),\ (x,t) \in \Gamma_f \times (0,\infty). \end{aligned} \tag{7.24}$$

Boundary conditions for thermal equation are

$$\begin{aligned} T(x,t) &= \bar{T}(x,t),\ (x,t) \in \Gamma_T \times (0,\infty), \\ -(K_T \nabla T + \alpha_c T K_p \nabla p) \cdot n &= \bar{f}_T(x,t),\ (x,t) \in \Gamma_h \times (0,\infty). \end{aligned} \tag{7.25}$$

Initial conditions for 3-field systems are

$$\begin{aligned} u(x,0) &= u_0(x),\ x \in \Omega, \\ \sigma''(x,0) &= \sigma_0''(x),\ x \in \Omega, \\ p(x,0) &= p_0(x),\ x \in \Omega, \\ T(x,0) &= T_0(x),\ x \in \Omega. \end{aligned} \tag{7.26}$$

7.2.4 Problem Statement

Based on the above discussion, a mathematical statement for 3-field problems is as follows: *Find* $(u(x,t),\, p(x,t),\, T(x,t)),\ \forall\ (x,t) \in \Omega \times (0,\infty)$ *such that:*

$$\begin{aligned} \nabla \cdot \sigma'' - \alpha \nabla p + f &= 0, \\ \alpha \tfrac{\partial (\nabla \cdot u)}{\partial t} + \tfrac{1}{M} \tfrac{\partial p}{\partial t} - \alpha_m \tfrac{\partial T}{\partial t} - \nabla \cdot (K_p \nabla p) &= q_p, \\ \alpha_T \tfrac{\partial T}{\partial t} + \alpha_p T \tfrac{\partial p}{\partial t} - \nabla \cdot (K_T \nabla T + \alpha_c T K_p \nabla p) &= q_T, \end{aligned} \tag{7.27}$$

with boundary conditions (7.23) – (7.25) and initial condition (7.26).

7.3 DG Weak Formulation

Because the plasticity and convection effects are taken into account, (7.27) is highly nonlinear. Particularly, an explicit constitutive relationship between total effective stress and total strain is unavailable in plasticity theory. Therefore, any weak formulation must be performed in an evolutionary or incremental form. Here, we rewrite (7.27) in terms of evolutionary primary

variables $(\dot{u}, \dot{p}, \dot{T})$ as follows:

$$\begin{gathered}
\nabla \cdot \dot{\sigma}'' - \alpha \nabla \dot{p} + \dot{f} = 0, \\
\alpha \tfrac{\partial (\nabla \cdot \dot{u})}{\partial t} + \tfrac{1}{M} \tfrac{\partial \dot{p}}{\partial t} - \alpha_m \tfrac{\partial \dot{T}}{\partial t} - \nabla \cdot (K_p \nabla \dot{T}) = \dot{q}_p, \\
\alpha_T \tfrac{\partial \dot{T}}{\partial t} + \alpha_p T \tfrac{\partial \dot{p}}{\partial t} - \nabla \cdot (K_T \nabla \dot{T} + \alpha_c \dot{T} K_p \nabla p) = \dot{q}_T.
\end{gathered} \tag{7.28}$$

First, we will focus on the governing equation for the solid part given in the first equation in (7.28). Considering (7.18), multiplying the first equation in (7.28) by test function $\dot{v}$, and integrating it by parts, we obtain

$$\begin{gathered}
\textstyle\int_E (\dot{\sigma}' - \alpha \dot{p} I - \dot{T} D_T) : \nabla \dot{v} dV - \int_{\partial E} ((\dot{\sigma}'' - \alpha \dot{p} I - \dot{T} D_T) n^s) \cdot \dot{v} dS \\
= \textstyle\int_E \dot{f} \cdot \dot{v} dV.
\end{gathered} \tag{7.29}$$

Here, we omit subscript h for all u_h, p_h, and T_h. Noting that $\dot{\sigma}'(u) : \nabla \dot{v} = \dot{\sigma}''(\mathbf{u}) : \nabla \dot{v}^T = \dot{\sigma}''(u) : \dot{\varepsilon}(v)$, we have

$$\begin{gathered}
\textstyle\int_E \dot{\sigma}'(u) : \dot{\varepsilon}(v) dV - \int_E (\alpha \dot{p} I) : \nabla \dot{v} dV - \int_E (\dot{T} D_T) : \nabla \dot{v} dV \\
- \textstyle\int_{\partial E} ((\dot{\sigma}' - \alpha \dot{p} I - \dot{T} D_T) n^s) \cdot \dot{v} dS = \int_E \dot{f} \cdot \dot{v} dV.
\end{gathered} \tag{7.30}$$

Also, noting that $(\alpha \dot{p} I) : \nabla \dot{v} = \alpha \dot{p} \nabla \cdot \dot{v}$ and $(\dot{T} D_T) : \nabla \dot{v} = \dot{T} D_T : \dot{\varepsilon}(v)$, we have

$$\begin{gathered}
\textstyle\int_E \dot{\sigma}'(u) : \dot{\varepsilon}(v) dV - \int_E \alpha \dot{p} \nabla \cdot \dot{v} dV - \int_E \dot{T} D_T : \dot{\varepsilon}(v) dV \\
- \textstyle\int_{\partial E} ((\dot{\sigma}' - \alpha \dot{p} I - \dot{T} D_T) n^s) \cdot \dot{v} dS = \int_E \dot{f} \cdot \dot{v} dV.
\end{gathered} \tag{7.31}$$

Then, summing over all elements χ, we obtain

$$\begin{gathered}
\textstyle\sum_{E \in \chi} \int_E \dot{\sigma}'(u) : \dot{\varepsilon}(v) dV - \sum_{E \in \chi} \int_E \alpha \dot{p} \nabla \cdot \dot{v} dV - \sum_{E \in \chi} \int_E \dot{T} D_T : \dot{\varepsilon}(v) dV \\
- \textstyle\sum_{\partial E \in S} \int_{\partial E} ((\dot{\sigma}' - \alpha \dot{p} I - \dot{T} D_T) n^s) \cdot \dot{v} dS = \sum_{E \in \chi} \int_E \dot{f} \cdot \dot{v} dV.
\end{gathered} \tag{7.32}$$

We now apply the definitions of average and jump terms defined in (2.10)-(2.15):

$$\begin{aligned}
&\textstyle\sum_{E\in\chi}\int_E \dot{\sigma}'(u):\dot{\varepsilon}(v)dV-\sum_{E\in\chi}\int_E \alpha\dot{p}\nabla\cdot\dot{v}dV-\sum_{E\in\chi}\int_E \dot{T}D_T:\dot{\varepsilon}(v)dV\\
&-\textstyle\sum_{\partial E\in S}\int_{\partial E}\{(\dot{\sigma}'-\alpha\dot{p}I-\dot{T}D_T)n^s\}\cdot[\dot{v}]dS=\sum_{E\in\chi}\int_E \dot{f}\cdot\dot{v}dV.
\end{aligned}\tag{7.33}$$

Adding face integrals $\sum\int_{\partial E}\{(\dot{\sigma}'(v)-\alpha\dot{p}I-\dot{T}D_T)n^s\}\cdot[\dot{u}]dS$ and $\frac{\delta_u}{|s|}\int_{\partial E}[\dot{u}]\cdot[\dot{v}]dS$ to (7.33) and considering the special well inner traction boundary condition, we have

$$\begin{aligned}
&\textstyle\sum_{E\in\chi}\int_E \dot{\sigma}'(u):\dot{\varepsilon}(v)dV-\sum_{E\in\chi}\int_E \alpha\dot{p}\nabla\cdot\dot{v}dV-\sum_{E\in\chi}\int_E \dot{T}D_T:\dot{\varepsilon}(v)dV\\
&-\textstyle\sum_{\partial E\in S_i+\Gamma_u}\int_{\partial E}\{(\dot{\sigma}'-\alpha\dot{p}I-\alpha_E\dot{T}I)n^s\}\cdot[\dot{v}]dS\\
&+\textstyle\sum_{\partial E\in\Gamma_{t_2}}\int_{\partial E} pn^s\cdot[\dot{v}]dS\\
&+\textstyle\sum\frac{\delta_u}{|s|}\int_{\partial E\in S_i+\Gamma_u+\Gamma_{t_2}}[\dot{u}]\cdot[\dot{v}]dS\\
&+\theta_{DG}\textstyle\sum\int_{\partial E\in S_i+\Gamma_u}\{(\dot{\sigma}'(v)-\alpha\dot{p}I-\dot{T}D_T)n^s\}\cdot[\dot{u}]dS\\
&-\theta_{DG}\textstyle\sum_{\partial E\in\Gamma t_2}\int_{\partial E} pn^s\cdot[\dot{u}]dS\\
&=\textstyle\sum_{E\in\chi}\int_E \dot{f}\cdot\dot{v}dV+\sum\int_{\partial E\in\Gamma_{t_1}}\bar{t}\cdot\dot{v}dS+\sum\frac{\delta_u}{|s|}\int_{\partial E\in\Gamma_u}\bar{u}\cdot\dot{v}dS\\
&+\theta_{DG}\textstyle\sum\int_{\partial E\in\Gamma_u}\{(\dot{\sigma}'(v)-\alpha\dot{p}I-\dot{T}D_T)n^s\}\cdot\bar{u}dS.
\end{aligned}\tag{7.34}$$

We now consider the fluid flow equation in the second line of (7.28). Following the same procedures for momentum equation, we have

$$\begin{aligned}
&\textstyle\sum_{E\in\chi}\frac{\partial}{\partial t}(\int_E \alpha\nabla\cdot\dot{u}\dot{w}dV+\int_E\frac{1}{M}\dot{p}\dot{w}dV-\int_E\alpha_m\dot{T}\dot{w}dV)\\
&+\textstyle\sum_{E\in\chi}\int_E(K_p\nabla\dot{p})\cdot\nabla\dot{w}dV-\sum\int_{\partial E\in S_i+\Gamma_p}\{(K_p\nabla\dot{p})\cdot n^s\}[\dot{w}]dS\\
&+\theta_{DG}\textstyle\sum\int_{\partial E\in S_i+\Gamma_p}\{(K_p\nabla\dot{w})\cdot n^s\}[\dot{p}]dS+\sum\frac{\delta_p}{|s|}\int_{\partial E\in S_i+\Gamma_p}[\dot{p}][\dot{w}]dS \qquad (7.35)\\
&=\textstyle\sum_{E\in\chi}\int_E\dot{q}_p\dot{w}dV-\sum\int_{\partial E\in\Gamma_f}\bar{f}_p\dot{w}dS.\\
&+\textstyle\sum\frac{\delta_p}{|s|}\int_{\partial E\in\Gamma_p}\bar{p}\dot{w}dS+\theta_{DG}\sum\int_{\partial E\in\Gamma_p}\{(K_p\nabla\dot{w})\cdot n^s\}\bar{p}dS.
\end{aligned}$$

Finally, the variational formulation for thermal equation is given as follows

$$\begin{aligned}
&\textstyle\sum_{E\in\chi}\frac{\partial}{\partial t}(\int_E\alpha_T\dot{T}\dot{z}dV+\int_E\alpha_pT\dot{p}\dot{z}dV)\\
&+\textstyle\sum_{E\in\chi}\int_E(K_T\nabla\dot{T}-\alpha_c\dot{T}V)\cdot\nabla\dot{z}dV\\
&-\textstyle\sum\int_{\partial E\in S_i+\Gamma_T}\{(K_T\nabla\dot{T})\cdot n^s\}[\dot{z}]dS\\
&+\textstyle\sum\int_{\partial E\in S_i+\Gamma_T}\{\alpha_cV\}\dot{T}^{\uparrow}\cdot n^s[\dot{z}]dS\\
&+\theta_{DG}\textstyle\sum\int_{\partial E\in S_i+\Gamma_T}\{(K_T\nabla\dot{z})\cdot n^s\}[\dot{T}]dS \qquad (7.36)\\
&-\theta_{DG}\textstyle\sum\int_{\partial E\in S_i+\Gamma_T}\{\alpha_cV\}\dot{z}^{\uparrow}\cdot n^s[\dot{T}]dS\\
&+\textstyle\sum\frac{\delta_T}{|s|}\int_{\partial E\in S_i+\Gamma_T}[\dot{T}][\dot{z}]dS\\
=&\textstyle\sum_{E\in\chi}\int_E\dot{q}_T\dot{z}dV-\sum\int_{\partial E\in\Gamma_h}\bar{f}_T\dot{z}dS+\sum\frac{\delta_T}{|s|}\int_{\partial E\in\Gamma_T}\bar{T}\dot{w}dS\\
&+\theta_{DG}\textstyle\sum\int_{\partial E\in\Gamma_T}\{(K_T\nabla\dot{z}+\alpha_c\dot{z}K_p\nabla p)\cdot n^s\}\bar{T}dS,
\end{aligned}$$

where the variable V is the velocity of the fluids and the notation " $\uparrow$ " indicates an upwinding scheme. The upwinding scheme is popular in finite difference

methods. This scheme was also applied to handle advection, convection, and transport equations in DG methods [26, 28, 34, 105, 107]. The variable $T^{\uparrow}$ is defined below:

$$T^{\uparrow} = \begin{cases} T_L & \text{if } V \cdot n^s \geq 0 \\ T_R & \text{otherwise} \end{cases} \tag{7.37}$$

where the subscripts L and R denote the left side and the right side of an interface. In the next step we follow similar numerical procedures as we did for plasticity and poroelasticity addressed in Chapter 3 and Chapter 5, which are summarized below:

(1) Integration on evolutionary stress-strain equations:

$$\dot{\sigma'} = D^{ep}(\sigma'')\dot{\varepsilon}, \tag{7.38}$$

$$\int_{\sigma_j''}^{\sigma_j''+\delta\sigma''} d\sigma' = \delta\sigma' = \int_{\varepsilon_j}^{\varepsilon_j+\delta\varepsilon} D^{ep}(\sigma'')d\varepsilon. \tag{7.39}$$

(2) Approximation on above integration using the Euler Forward method:

$$\delta\sigma' = D^{ep}(\sigma_j'')\delta\varepsilon. \tag{7.40}$$

(3) Time discretization using finite difference methods:

$$\int_{t^k}^{t^{k+1}} p dt \cong (p^k + \Theta\delta p)\delta t^k, \tag{7.41}$$

and

$$\int_{t^k}^{t^{k+1}} T dt \cong (T^k + \Theta\delta T)\delta t^k. \tag{7.42}$$

(4) Selection for interpolation functions for displacement, pressure, and temperature:

$$\begin{aligned} \delta u_h &= N_u \delta U, \\ \delta p_h &= N_p \delta P, \\ \delta T_h &= N_T \delta \mathfrak{T}, \end{aligned} \tag{7.43}$$

where U, P, and $\mathfrak{T}$ are nodal values for displacement, pressure, and temperature. Procedures 1 and 2 above carry out a linearized or incremental weak formulation for 3-field problems. Finally, algebraic equations for solving 3-field problems are given by:

$$\begin{aligned} &\left[\begin{array}{ccc} K_b^{uu} + K_s^{uu} & K_b^{up} + K_s^{up} & K_b^{uT} + K_s^{uT} \\ K_b^{pu} & M_b^{pp} + \delta t^k (K_b^{pp} + K_s^{pp}) & K_b^{pT} \\ 0 & K_b^{Tp} & M_b^{TT} + \delta t^k (K_b^{TT} + K_s^{TT}) \end{array} \right]_{t^k} \left\{ \begin{array}{c} \delta U \\ \delta P \\ \delta \mathfrak{T} \end{array} \right\} \\ &= \left[\begin{array}{c} 0 \\ -\delta t_k (K_b^{pp} + K_s^{pp}) P \\ -\delta t_k (K_b^{TT} + K_s^{TT}) \mathfrak{T} \end{array} \right]_{t^k} + \left[\begin{array}{c} \frac{\partial F_u}{\partial t} \\ \bar{Q}_p \\ \bar{Q}_T \end{array} \right] \delta t^k, \end{aligned} \tag{7.44}$$

where superscripts u, p, and T indicate displacement, pressure, and temperature fields, subscripts b and s indicate stiffnesses obtained from volume and surface integration, respectively, and subscript t^k indicates time at the kth step. Also, we list the relations between the stiffness matrices in eq. (7.44) and the integration components in (7.34)-(7.36). The stiffness matrices related

volume integration are

$$K_b^{uu} = K_b^{uu}(D^{ep}, \nabla N_u) \Longleftrightarrow -\sum_{E\in\chi}\int_E \dot{\sigma}'(u) : \dot{\varepsilon}(v)dV, \tag{7.45}$$

$$K_b^{pp} = (K_p, \nabla N_p) \Longleftrightarrow \sum_{E\in\chi}\int_E (K_p\nabla\dot{p})\cdot\nabla\dot{w}dV, \tag{7.46}$$

$$K_b^{TT} = (K_T, \nabla N_T, N_T, V) \Longleftrightarrow \sum_{E\in\chi}\int_E (K_T\nabla\dot{T} - \alpha_c\dot{T}V)\cdot\nabla\dot{z}dV. \tag{7.47}$$

The interface stiffnesses contributing to element stiffness are grouped by

$$\begin{aligned} K_s^{uu} = K_s^{uu}(D^{ep}, \nabla N_u, n^s) \Longleftrightarrow & \textstyle\sum_{\partial E\in S_i+\Gamma_u+\Gamma_{t_2}}\int_{\partial E}\dot{\sigma}'(u)n^s\cdot[\dot{v}]dS \\ & -\theta_{DG}\textstyle\sum_{\partial E\in S_i+\Gamma_u+\Gamma_{t_2}}\int_{\partial E}\{(\dot{\sigma}'(v)n^s\}\cdot[\dot{u}]dS \\ & -\textstyle\sum\frac{\delta_u}{|s|}\int_{\partial E\in S_i+\Gamma_u+\Gamma_{t_2}}[\dot{u}]\cdot[\dot{v}]dS, \end{aligned} \tag{7.48}$$

$$\begin{aligned} K_s^{pp} = K_s^{pp}(K_p, \nabla N_p, N_p, n^s) \Longleftrightarrow & -\textstyle\sum\int_{\partial E\in S_i+\Gamma_p}\{(K_p\nabla\dot{p})\cdot n^s\}[\dot{w}]dS \\ & +\theta_{DG}\textstyle\sum\int_{\partial E\in S_i+\Gamma_p}\{(K_p\nabla\dot{w})\cdot n^s\}[\dot{p}]dS, \\ & +\textstyle\sum\frac{\delta_p}{|s|}\int_{\partial E\in S_i+\Gamma_p}[\dot{p}][\dot{w}]dS, \end{aligned} \tag{7.49}$$

$$\begin{aligned} K_s^{TT} = (K_T, \nabla N_T, N_T, V, n^s) \Longleftrightarrow & -\textstyle\sum\int_{\partial E\in S_i}\{(K_T\nabla\dot{T})\cdot n^s\}[\dot{z}]dS \\ & +\textstyle\sum\int_{\partial E\in S_i}\{\alpha_c V\}\dot{T}^{\uparrow}\cdot n^s[\dot{z}]dS \\ & +\textstyle\sum\frac{\delta_T}{|s|}\int_{\partial E\in S_i+\Gamma_T}[\dot{T}][\dot{z}]dS \\ & +\theta_{DG}\textstyle\sum\int_{\partial E\in S_i}\{(K_T\nabla z\}[\dot{T}]dS \\ & -\theta_{DG}\textstyle\sum\int_{\partial E\in S_i}\{\alpha_c V\}\dot{z}^{\uparrow}\cdot n^s[\dot{T}]dS. \end{aligned} \tag{7.50}$$

The mass stiffness matrices are given by

$$M_b^{pp} = M_b^{pp}(\frac{1}{M}, N_p) \Longleftrightarrow \sum_{E\in\chi}\int_E \frac{1}{M}\dot{p}\dot{w}dV, \tag{7.51}$$

$$M_b^{TT} = M_b^{TT}(\alpha_T, N_T) \Longleftrightarrow \sum_{E\in\chi} \int \alpha_T \dot{T}\dot{z} dV. \tag{7.52}$$

The coupling stiffness matrices involving volume integration are

$$K_b^{up} = K_b^{up}(\alpha, \nabla N_u, N_p) \Longleftrightarrow \sum_{E\in\chi} \int_E \alpha \dot{p} \nabla \cdot \dot{v} dV, \tag{7.53}$$

$$K_b^{ut} = K_b^{ut}(\alpha_E, \nabla N_u, N_T) \Longleftrightarrow \sum_{E\in\chi} \int_E \dot{T} D_T : \dot{\varepsilon}(v) dV, \tag{7.54}$$

$$K_b^{pT} = K_b^{pT}(\alpha_m, N_p, N_T) \Longleftrightarrow -\sum_{E\in\chi} \int \alpha_m \dot{T}\dot{w} dV, \tag{7.55}$$

$$K_b^{pu} = K_b^{pu}(\alpha, \nabla N_u, N_p) \Longleftrightarrow \sum_{E\in\chi} \int_E \alpha \nabla \cdot \dot{u}\dot{w} dV, \tag{7.56}$$

$$K_b^{Tp} = K_b^{Tp}(\alpha_m, N_p, N_T, T) \Longleftrightarrow \sum_{E\in\chi} \int \alpha_m T \dot{p}\dot{z} dV. \tag{7.57}$$

The interface stiffnesses contributing to element stiffnesses are grouped by

$$\begin{aligned} K_s^{up} = K_s^{up}(\alpha, N_u, N_p, n^s) \Longleftrightarrow \textstyle\sum_{\partial E\in S_i+\Gamma_u+\Gamma_{t_2}} \int_{\partial E} \{\alpha \dot{p} n^s\} \cdot [\dot{v}] dS \\ -\theta_{DG} \textstyle\sum_{\partial E\in S_i+\Gamma_u+\Gamma_{t_2}} \int_{\partial E} \{\alpha \dot{p} n^s\} \cdot [\dot{u}] dS, \end{aligned} \tag{7.58}$$

$$\begin{aligned} K_s^{uT} = K_s^{uT}(\alpha_E, N_u, N_T, n^s) \Longleftrightarrow \textstyle\sum_{\partial E\in S_i+\Gamma_u+\Gamma_{t_2}} \int_{\partial E} \{\dot{T} D_T n^s\} \cdot [\dot{v}] dS \\ -\theta_{DG} \textstyle\sum_{\partial E\in S_i+\Gamma_u+\Gamma_{t_2}} \int_{\partial E} \{\dot{T} D_T n^s\} \cdot [\dot{v}] dS. \end{aligned} \tag{7.59}$$

The right hand side load vector F_u is written by

$$\begin{aligned} F_u = F_u(f, \bar{t}, \bar{u}, N_u, N_p, N_T, n^s) \Longleftrightarrow \\ -\textstyle\sum_{E\in\chi} \int_E \dot{f} \cdot \dot{v} dV - \sum \int_{\partial E\in\Gamma_N} \bar{t} \cdot v dS - \sum \frac{\delta_u}{|s|} \int_{\partial E\in\Gamma_u} \bar{u} \cdot \dot{v} dS \\ -\theta_{DG} \textstyle\sum \int_{\partial E\in\Gamma_u} \{(\dot{\sigma}'(v) - \alpha \dot{p} I - \dot{T} D_T) n^s\} \cdot \bar{u} dS. \end{aligned} \tag{7.60}$$

The right hand side fluid flux vector $\bar{Q}_p$ is given by

$$\bar{Q_p} = \bar{Q_p}(\bar{q}_p, \bar{f}_p, K_p, \bar{p}, N_p, \nabla N_p, n^s) \Longleftrightarrow$$

$$\sum_{E\in\chi} \int_E \dot{q}_p \dot{w} dV - \sum \int_{\partial E\in\Gamma_f} \bar{f}_p \dot{w} dS + \sum \frac{\delta_p}{|s|} \int_{\partial E\in\Gamma_p} \bar{p}\dot{w} dS \tag{7.61}$$

$$+\theta_{DG} \sum \int_{\partial E\in\Gamma_P} \{(K_p \nabla \dot{w}) \cdot n^s\} \bar{p} dS.$$

The right hand side heat flux vector $\bar{Q}_T$ is given by

$$\bar{Q_T} = \bar{Q_T}(\bar{q}_T, \bar{f}_T, K_T, \bar{T}, V, N_T, \nabla N_T, n^s) \Longleftrightarrow$$

$$\sum_{E\in\chi} \int_E \dot{q}_T \dot{z} dV - \sum \int_{\partial E\in\Gamma_h} \bar{f}_T \dot{z} dS + \sum \frac{\delta_T}{|s|} \int_{\partial E\in\Gamma_T} \bar{T}\dot{z} dS \tag{7.62}$$

$$+\theta_{DG} \sum \int_{\partial E\in\Gamma_T} \{(K_T \nabla \dot{z} - \alpha_c \dot{z} V) \cdot n^s\} \bar{T} dS.$$

7.4 DG Implementation

DG implementation for solving 3-field problems has been carried out by incorporating the plasticity program and adding new code for the thermal equation into the computer code for poroelasticity. Iteration schemes for solving plasticity discussed and implemented in Chapter 3 can be fully exploited without any modification. There are three levels of loops in the program for 3-field problems. The first level loop is for time marching. The second level is an inner loop for global iteration for force balance. The third level loop is for iteration at the material level, which requires the effective stress to be on an admissible space. The procedures for iterations on material level have been addressed in Chapter 3. In this section we discuss computation on residue load vector for 3-field problems. A total incremental external force vector can

be extracted from (7.44)

$$\delta F^E = \begin{bmatrix} \delta F_u^E \\ \delta F_p^E \\ \delta F_T^E \end{bmatrix} = \begin{bmatrix} 0 \\ -\delta t^k (K_b^{pp} + K_s^{pp}) P \\ -\delta t^k (K_b^{TT} + K_s^{TT}) \mathcal{T} \end{bmatrix}_{t^k} + \begin{bmatrix} \frac{\partial F_u}{\partial t} \\ \bar{Q}_p \\ \bar{Q}_T \end{bmatrix} \delta t^k. \tag{7.63}$$

Total incremental internal force vector is denoted by

$$\delta F^I = \begin{bmatrix} \delta F_u^I \\ \delta F_p^I \\ \delta F_T^I \end{bmatrix}, \tag{7.64}$$

where

$$\delta F_u^I = -\sum_E \int_E {B_u}^T(\delta\sigma' - \alpha\delta pI - \alpha_E\delta T D_T)dV$$

$$+\sum_{\partial E}\int_{S_i+\Gamma_u}[{N_u}^T]n\{\delta\sigma' - \alpha\delta pI - \alpha_E\delta T D_T\}dS$$

$$-\sum_{\partial E}\int_{\Gamma_{t_2}}{N_u}^T\delta p n^s dS - \sum\frac{\delta_u}{|s|}\int_{\partial E\in S_i+\Gamma_u+\Gamma_{t_2}}[{N_u}^T][\delta u]dS$$

$$-\theta_{DG}\sum_{\partial E}\int_{S_i+\Gamma_u}\{{B_u}^T D^{epT}n^T - \alpha N_p^T n^{sT} - \alpha_E {N_T}^T {D_T}^T {n'}^T\}[\delta u]dS$$

$$+\theta_{DG}\sum_{\partial E}\int_{\Gamma_{t_2}}{N_p}^T n^{sT}\delta u dS,$$

$$\delta F_p^I = -\delta t^k\sum_E\int_E B_p^T\delta Q_p dV + \delta t^k\sum_{\partial E}\int_{S_i+\Gamma_p}[{N_p}^T]n^s\{\delta Q_p\}dS$$

$$+\delta t^k\theta_{DG}\int_{\partial E\in S_i+\Gamma_p}\{{B_p}^T{K_p}^T n'\}[\delta p]dS + \delta t^k\sum\frac{\delta_p}{|s|}\int_{\partial E\in S_i+\Gamma_p}[{N_p}^T][\delta p]dS$$

$$+\sum_E\int_E N_p^T(\alpha\nabla\cdot\delta u + \frac{1}{M}\delta p - \alpha_m\delta T)dV,$$

$$\delta F_T^I = -\delta t^k\sum_E\int_E B_T^T(\delta Q_T + \alpha_c V\delta T)dV$$

$$+\delta t^k\int_{\partial E\in S_i+\Gamma_T}[{N_T}^T]n^s\{\delta Q_T\}dS$$

$$+\delta t^k\int_{\partial E\in S_i+\Gamma_T}[{N_T}^T]n^s\{\alpha_c V\}\delta T^{\uparrow}dS$$

$$+\delta t^k\theta_{DG}\int_{\partial E\in S_i+\Gamma_T}\{({B_T}^T K_T\}[\delta T]dS$$

$$-\delta t^k\theta_{DG}\int_{\partial E\in S_i+\Gamma_T}N_T^{\uparrow}\{\alpha_c V\}n^s[\delta T]dS$$

$$+\delta t^k\sum\frac{\delta_T}{|s|}\int_{\partial E\in S_i+\Gamma_T}[{N_T}^T][\delta T]dS + \sum_E\int_E N_p^T(\alpha_T\delta p + \alpha_p T\delta p)dV, \tag{7.65}$$

Residue load vector δF^R for next global iteration is then given by

$$\delta F^R = \delta F^E - \delta F^I. \tag{7.66}$$

A flow diagram for solving thermoporoelastoplasticity problems is presented in Figure 7.2.

7.5 A Single Injection Well

In this section we present a single injection well problem solved by using both CG and DG methods. In this problem we consider a well injecting a fluid that is identical to the fluid contained in porous rock. The geometrical configuration of the well is shown in Figure 7.3(a). Axial symmetry is assumed in this model. A computational model is shown in Figure 7.3(b). Only a thin layer in the z-direction is studied.

In this well computational model boundary conditions for solid skeletons are summarized below:

$$\begin{gathered}
u_x = 0,\ \bar{t}_y = 0,\ \bar{t}_z = 0 \quad at\ x = 0; \\
u_y = 0,\ \bar{t}_x = 0,\ \bar{t}_z = 0 \quad at\ y = 0; \\
\bar{t}_x = \bar{t}_y = \bar{t}_z = 0 \quad at\ r = R^e; \\
\sigma n^s = -p n^s \quad at\ r = R^i; \\
u_z = 0,\ \bar{t}_y = 0,\ \bar{t}_x = 0 \quad at\ z = 0; \\
\bar{t_z} = 0,\ \bar{t}_y = 0,\ \bar{t}_x = 0 \quad at\ z = h.
\end{gathered} \tag{7.67}$$

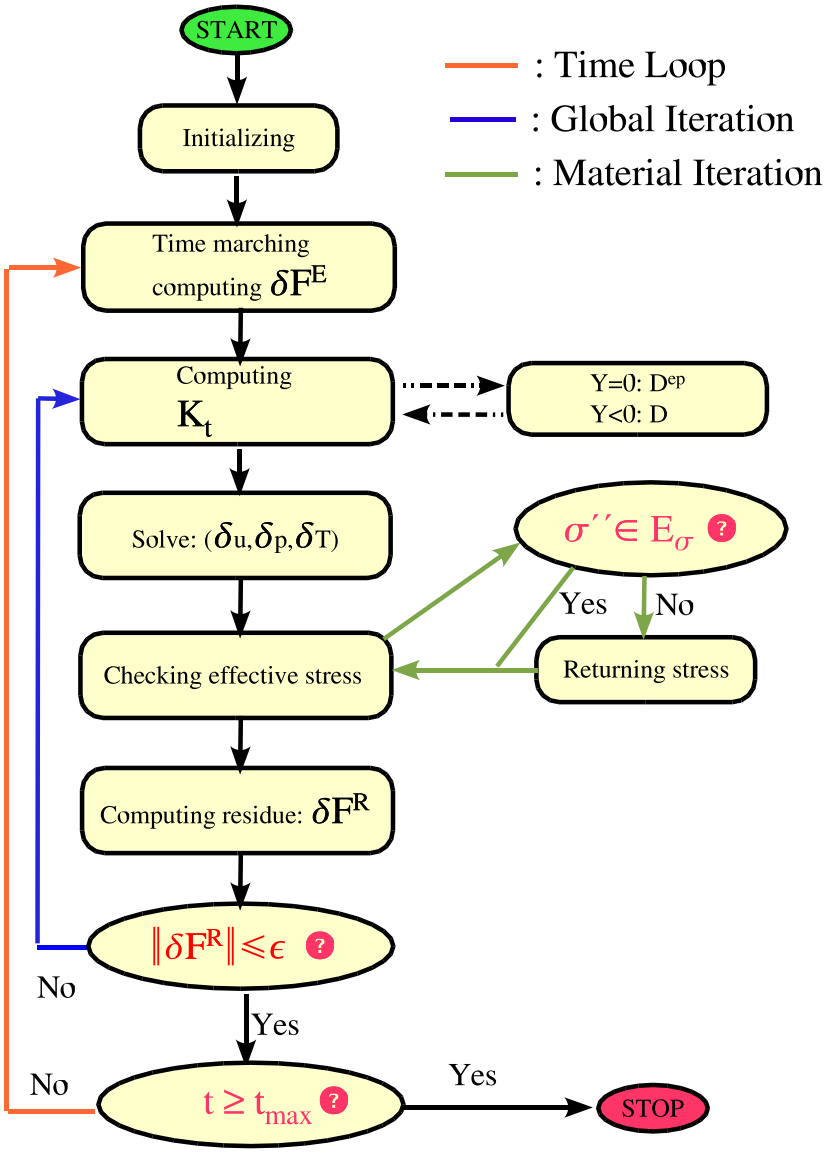

Figure 7.2: Flow Diagram of DG for Thermoporoelastoplasticity Problems

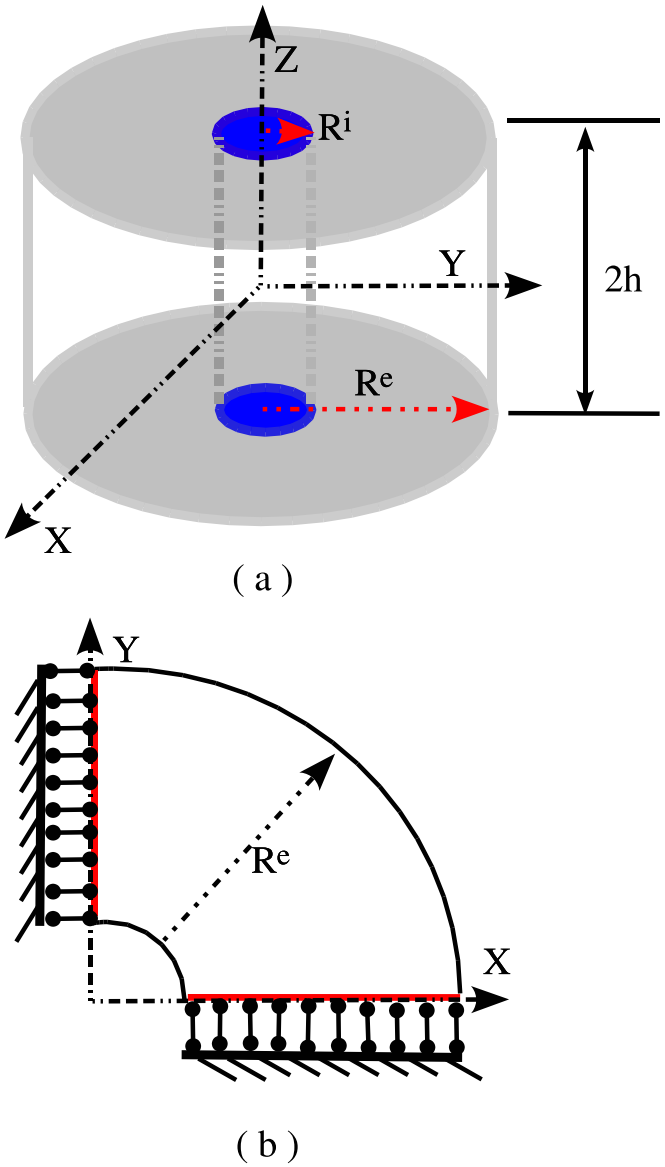

Figure 7.3: (a) Geometric Profile of a Single Well Model and (b) Well Computational Model

The boundary conditions for pressure field is given below:

$$\begin{gathered} -K_p \nabla p \cdot n^s = \bar{f}_p = 0 \quad at\ x = 0; \\ -K_p \nabla p \cdot n^s = \bar{f}_p = 0 \quad at\ y = 0; \\ p = 0 \quad at\ r = R^e; \\ -K_p \nabla p \cdot n^s = \bar{f}_p \neq 0 \quad at\ r = R^i; \\ -K_p \nabla p \cdot n^s = \bar{f}_p = 0 \quad at\ z = 0; \\ -K_p \nabla p \cdot n^s = \bar{f}_p = 0 \quad at\ z = h. \end{gathered} \tag{7.68}$$

The boundary conditions for temperature field is prescribed as follows:

$$\begin{gathered} -(K_T \nabla T - \alpha_c T V) \cdot n^s = \bar{f}_T = 0 \quad at\ x = 0; \\ -(K_T \nabla T - \alpha_c T V) \cdot n^s = \bar{f}_T = 0 \quad at\ y = 0; \\ -(K_T \nabla T - \alpha_c T V) \cdot n^s = 0 \quad at\ r = R^e; \\ T = \bar{T} \neq 0 \quad at\ r = R^i; \\ -(K_T \nabla T - \alpha_c T V) \cdot n^s = \bar{f}_T = 0 \quad at\ z = 0; \\ -(K_T \nabla T - \alpha_c T V) \cdot n^s = \bar{f}_T = 0 \quad at\ z = h. \end{gathered} \tag{7.69}$$

Zero initial conditions are set up for all field variables. The geometry data, material parameters, and coefficients are summarized in Table 7.1. The mesh configuration of the well is shown in Figure 7.4. We use a fine mesh in the area near the well wall and coarse mesh in the area far from the well wall.

7.5.1 Thermoporoelasticity

In this subsection we will solve the above injection well problem using both CG and DG methods. Modified Newton-Raphson method is used for

R^I: 0.1 m	R^E: 1 m	h: 2m	$\bar{T} = -100^0$C
$E = 3.0 \times 10^9$Pa	$\nu = 0.2$	$\alpha = 1.0$	$M = 3.0 \times 10^{10}$
$K_p = 1.0 \times 10^{-5}/m^2/Pa.s$	$\alpha_T = 6.3 \times 10^{-6} J/m^3/^0C$	$\alpha_p = 3.0 \times 10^{-5}/^0C$	$K_T = 2W/m/^0/C$
$\alpha_E = 4.0 \times 10^5 Pa/^0C$	$P_0 = 0$	$\bar{q}_p = 3.0 \times 10^{-2} m^3/s$	$T_0 = 0^0C$
$\alpha_m = 3.0 \times 10^{-5}/^0C$	$\alpha_C = 4.0 \times 10^5 J/m^3/^0C$		

Table 7.1: Data for Injection Well

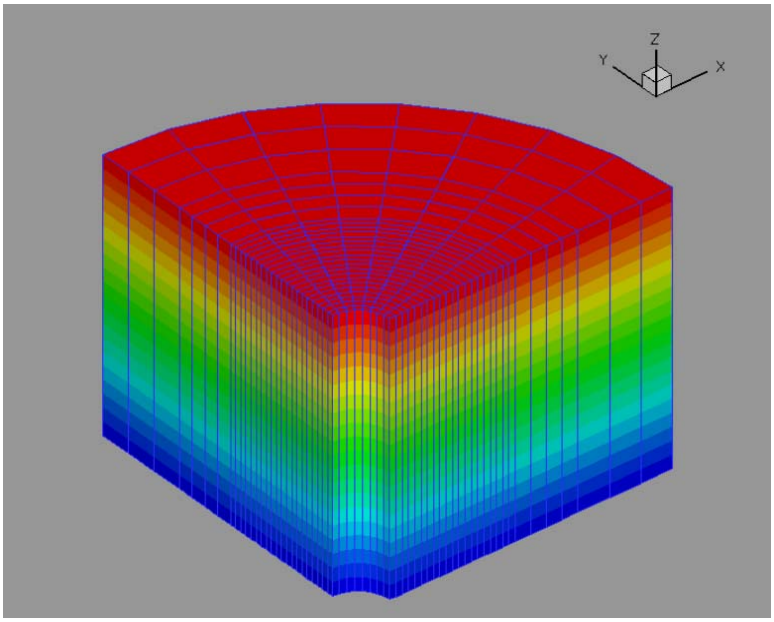

Figure 7.4: Meshing of Injection Well

nonlinear iterations. The solid skeleton is assumed to be elastic during the whole evolutionary process. Particularly, we want to focus on the following questions:

(1) How does the pore pressure diffuse?

(2) How does the temperature diffuse?

(3) What is the effect of the convection?

(4) How does the CG perform?

(5) What are the advantages of the DG methods?

(6) How does the well compact?

It should be mentioned that large time steps cannot be used for this convection dominated problem because they will not reach convergent solutions. For CG methods, time steps less than or equal to 5 seconds are required to obtain convergent solutions for this problem. Time steps less than or equal to 21 seconds can be used in DG methods. The evolution of the pore pressure profiles obtained from DG and analytical method (steady state) for various injection times are presented in Figure 7.5. We use one second time steps in this well problem. It shows that the steady pore pressure state is quickly reached. Also, CG has the same pressure prediction as DG and is not shown in Figure 7.5. There is no oscillation in pressure solution obtained from CG method. The performance of CG for pressure solution is very good. The analytical solution for pressure also shown in this figure is the steady state solution, which is given by the classical logarithmic law.

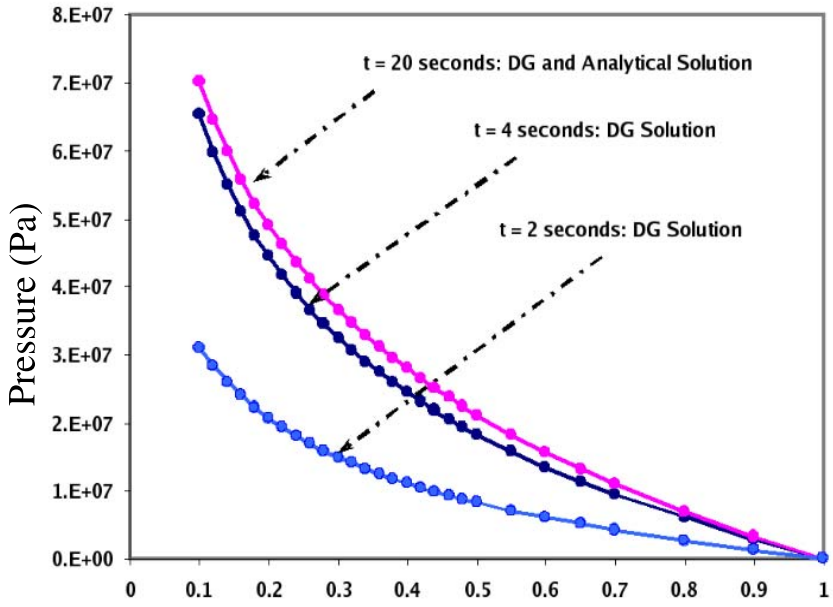

Figure 7.5: Evolution of Pressure Profile for the Injection Well Problem Predicted by DG and Analytical Methods.

The temperature profiles obtained from CG at 500 seconds with and without considering the convection term are shown in Figure 7.6. If the conductive term is negligible with respect to the convection term and the decoupling of temperature from skeleton deformation and fluid flow is assumed, an analytical solution for temperature evolution is available. This analytical solution is a step-wise function. The thermal front is very steep and sharp. This is quite different from the one only considering conduction, which is similar to the logarithmic distribution of pore pressure. As expected, numerical solutions for temperature front are governed by the convective effect. In addition, there is no obvious difference in CG and DG at 500 seconds. A more complete evolution profile of the temperature considering the convection effect can be found in latter figures.

However, these smooth CG solutions for temperature shown above are not at earlier stages. Early CG and DG solutions for temperature profile are presented in Figure 7.7. we see that CG gives a nonphysical oscillatory solution near the vicinity of the well wall. DG solutions avoid any obvious oscillation in early stages.

A whole evolutionary process of CG solution for temperature especially in longer time when the thermal front enters coarse mesh domains is further presented in Figure 7.8. There are some obvious ribbons after 800 seconds. This shows that CG method works very well for fine mesh domains but oscillates over coarse meshes. Moreover, this pollution in the area indicated by these ribbons propagates into the vicinity of the well wall.

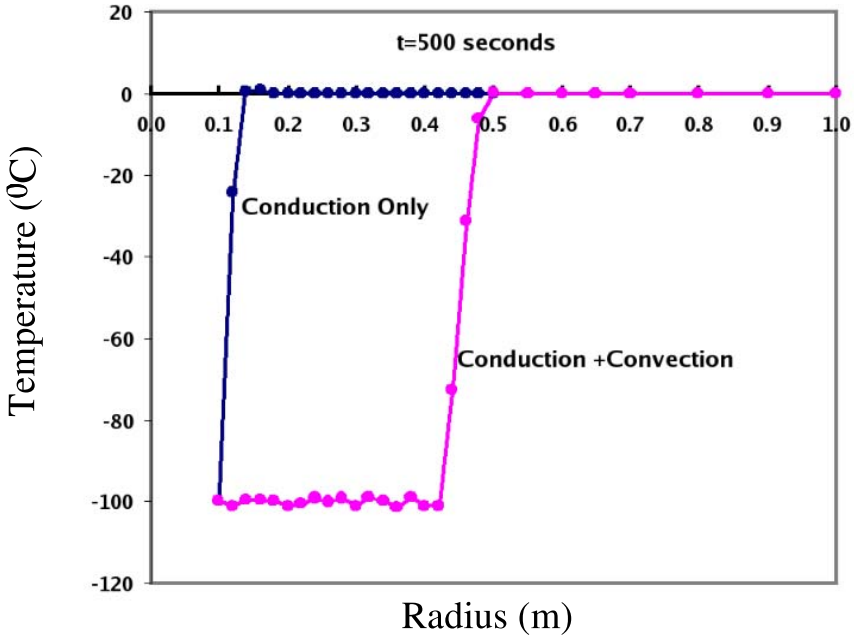

Figure 7.6: Comparison of Conduction and Convection Effects Predicted by CG Methods.

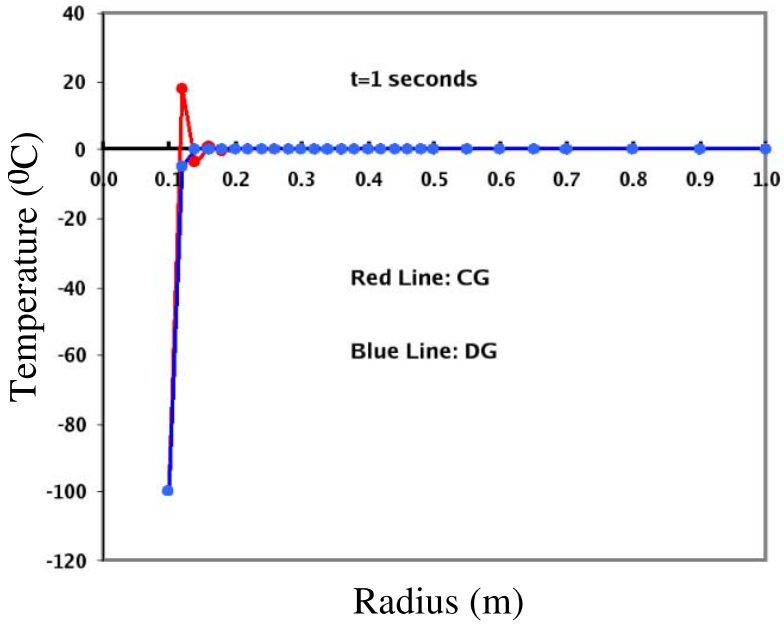

Figure 7.7: Temperature Profile at Early Time Predicted by CG and DG Methods.

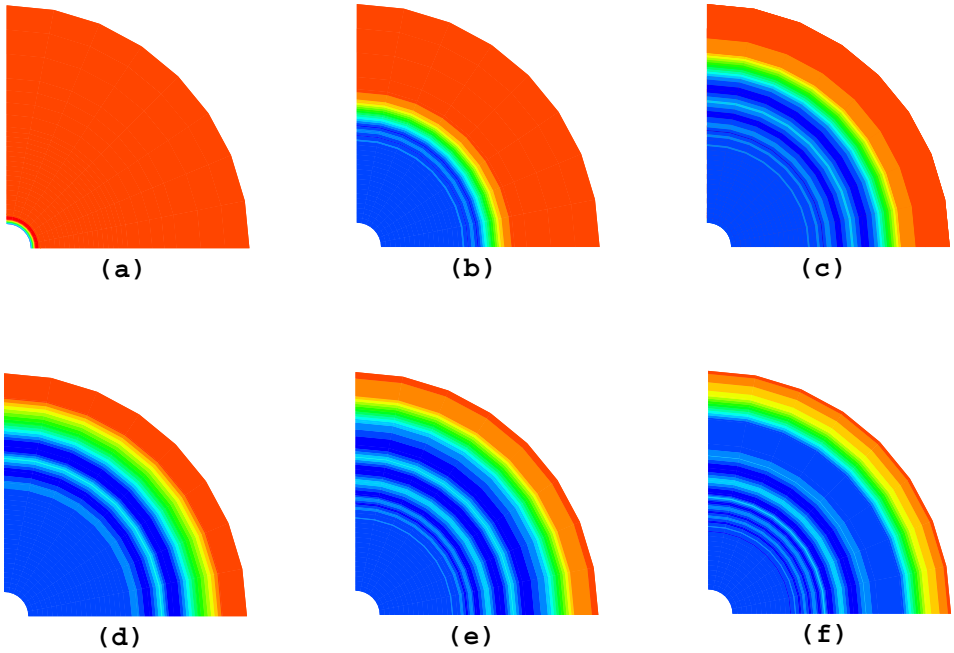

Figure 7.8: Evolution of Temperature Profile Obtained from CG methods (thermoporoelasticity model). (a) t=10 seconds; (b) t=800 seconds; (c) t=1450 seconds; (d) t=1700 seconds; (e) t=1850 seconds; (f) t=1950 seconds.

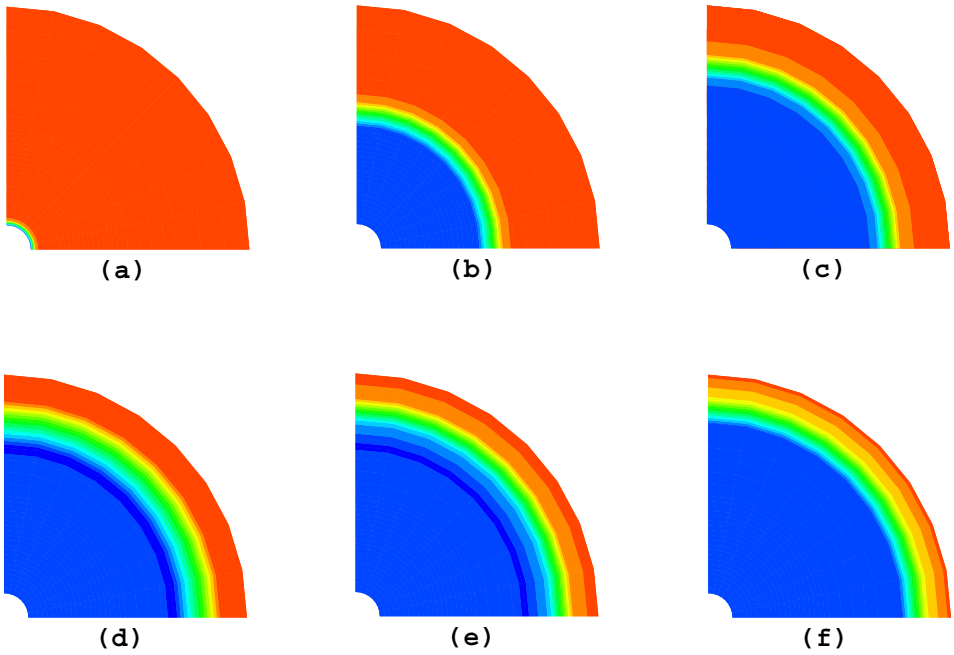

Figure 7.9: Evolution of Temperature Profile Obtained from DG methods (thermoporoelasticity model). (a) t=10 seconds; (b) t=800 seconds; (c) t=1450 seconds; (d) t=1700 seconds; (e) t=1850 seconds; (f) t=1950 seconds.

Figure 7.9 shows the DG (IIPG) results for evolution process of thermal front. We see that there are no obvious ribbons in the contoured temperature field. It is concluded that DG methods can avoid nonphysical temperature oscillation solution in coarse mesh domains. They also restrain errors induced at coarse mesh domains from propagation into fine mesh domains.

Figure 7.10 shows the evolution process of the compaction of the well following injection time predicted by DG methods. At the beginning, the pressure effect dominates the deformation of the well. The well swells as the

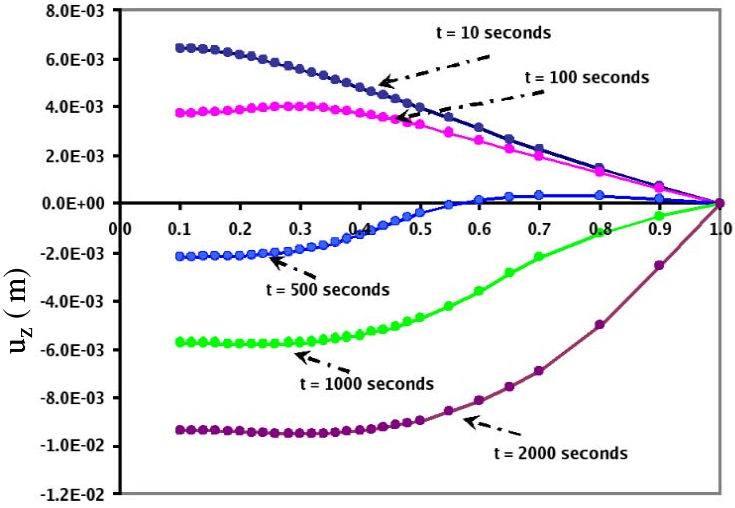

Figure 7.10: Well Compaction Predicted by DG Methods

fluid pours into the medium. As injection time goes longer, the thermal effect dominates the compaction of the well. Instead of swelling the well compacts as the temperature of injected fluid is lower than the virgin temperature field.

7.5.2 Plasticity Effect

In this subsection we study how plastic zones develop and how well compaction is affected when solid skeletons yield. Drucker-Prager's model with a user defined hardening law for the cap is used in the computation. Model parameters related to plasticity are summarized in Table 7.2. The definitions of notations in this table can be found in Chapter 3. Also, a non-associated model is assumed.

The evolution of temperature profile for plasticity model obtained by

C_0 = 20Mpa, ϕ_1 =0.5 rad, ϕ_2 =0.4 rad, X =-40 Mpa, R =0.5
User defined hardening function $(\epsilon_{vp}, \sigma_{mean})$: (0, 16), (0.15, 20), (0.44, 24), (0.73, 28), (1.02, 32)
Note: strain in $10^{-3}$and stress in Mpa

Table 7.2: Plastic Parameters for Injection Well Problem

using CG is shown in Figure 7.11. Again, this shows that temperature is oscillatory over domains with coarse mesh. A nice performance of the DG method (IIPG) for temperature evolution is presented in Figure 7.12. The development of plastic zones predicted by the DG method (IIPG) is shown in Figure 7.13. At very early stages the plastic zone develops at the area very close to the well wall. The plastic domain also propagates outward during a rapid increase in the pore pressure within 50 seconds. After 50 seconds, these plastic zones will not propagate any more until 200 seconds later. At later time, the plastic zones start to propagate again because the yielding process is dominated by thermal convection. The compaction of the well with consideration of plasticity is shown in Figure 7.14.

7.6 Summary

CG methods do not work very well for the prediction of the temperature field at early time stages of fluid injection in the well problem. Moreover, CG solutions in fine mesh domains are polluted by errors induced in coarse mesh domains. Thus, strictly speaking, CG methods can not be used to model poro-plasticity problems at early evolutionary stages. The proposed DG methods can avoid nonphysical temperature oscillations at the beginning and in coarse

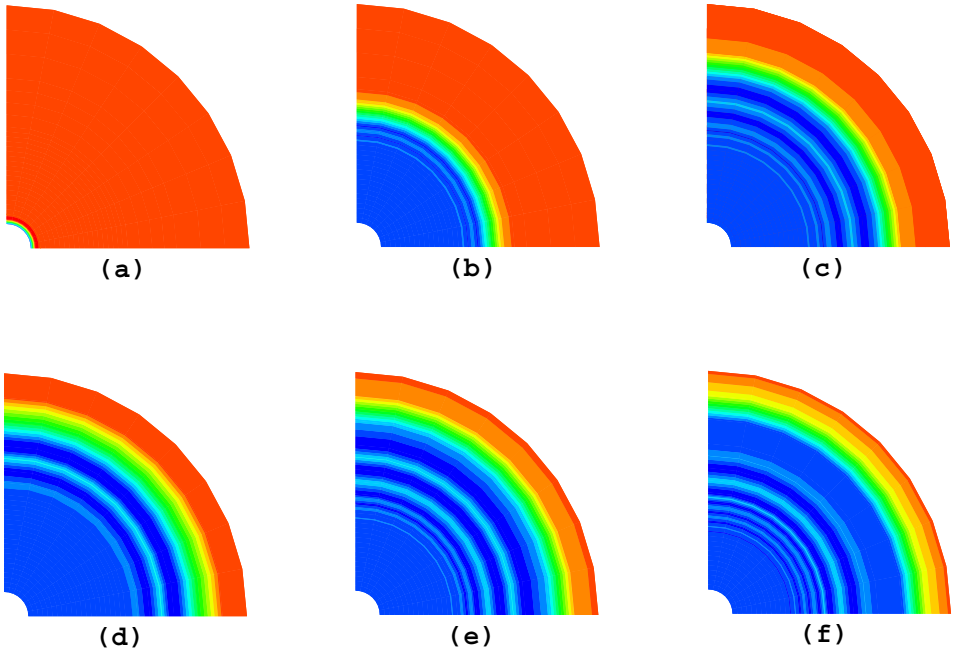

Figure 7.11: Evolution of Temperature Profile Obtained from CG methods (thermoporoelastoplasticity model). (a) t=10 seconds; (b) t=800 seconds; (c) t=1450 seconds; (d) t=1700 seconds; (e) t=1850 seconds; (f) t=1950 seconds.

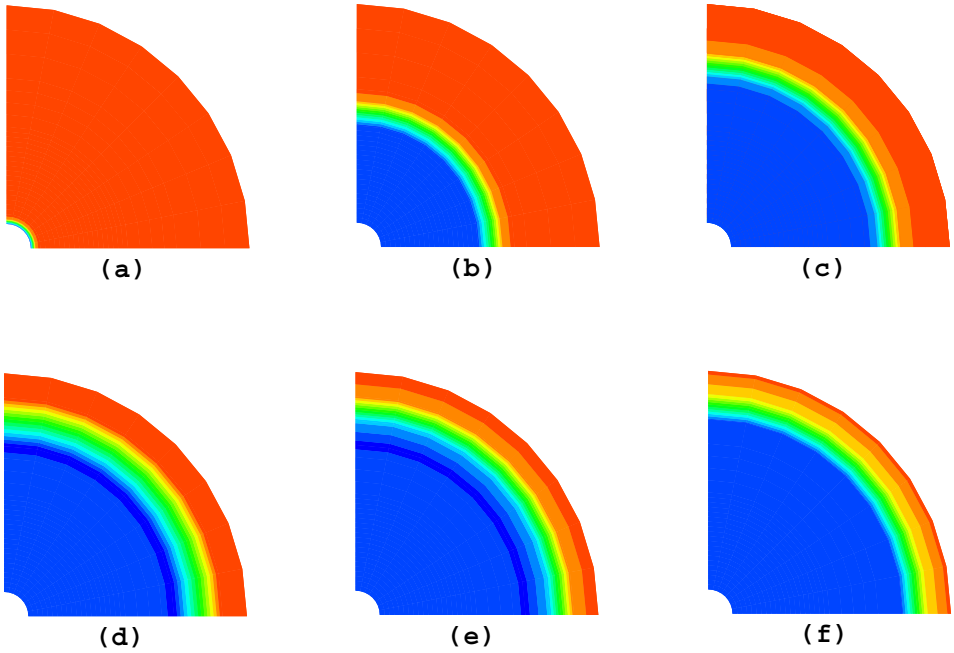

Figure 7.12: Evolution of Temperature Profile Obtained from DG methods (thermoporoelastoplasticity model). (a) t=10 seconds; (b) t=800 seconds; (c) t=1450 seconds; (d) t=1700 seconds; (e) t=1850 seconds; (f) t=1950 seconds.

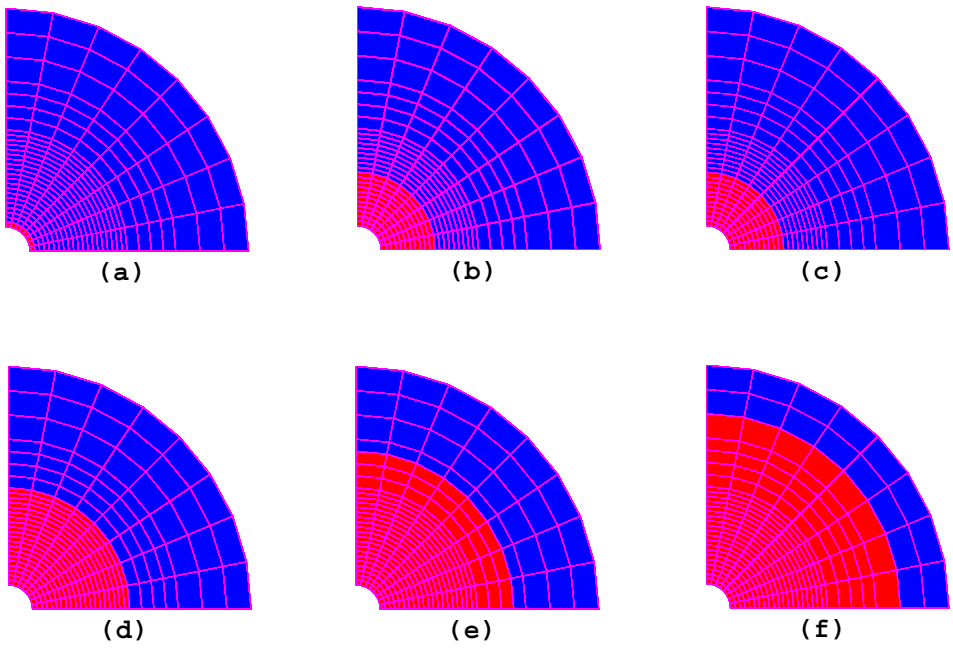

Figure 7.13: Development of Plastic Zone. (a) t=1 second; (b) t=50 seconds; (c) t=200 seconds; (d) t=550 seconds; (e) t=750 seconds; (f) t=950 seconds.

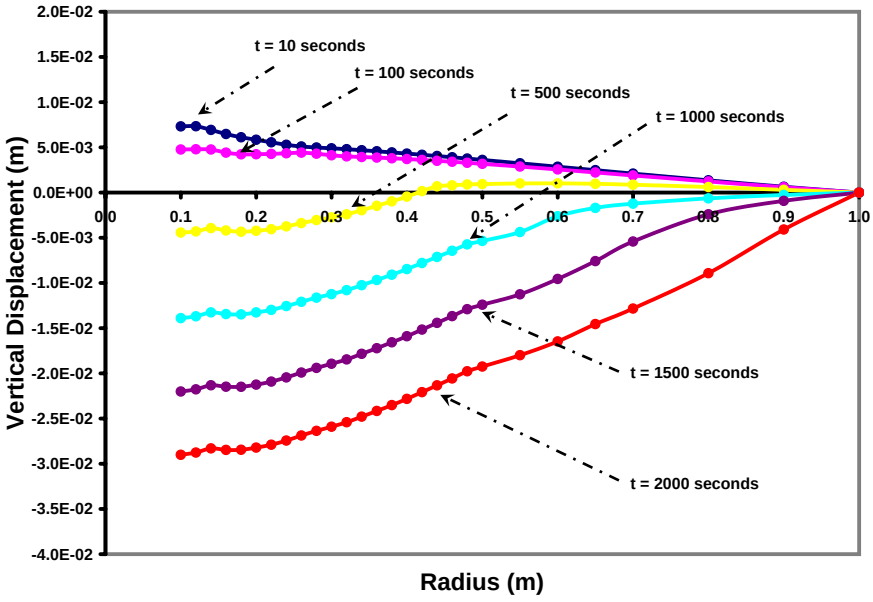

Figure 7.14: Well Compaction Predicted by Plasticity Theory and DG Methods

mesh domain, which are particularly important to thermoporoelastoplasticity problems. The small time step requirement for CG methods can be relaxed for DG methods.

Chapter 8

Conclusions and Future Work

8.1 Conclusions

1. A family of DG methods including SIPG, OBB, NIPG and IIPG has been proposed and formulated to solve linear elasticity problems. A nodal-based DG finite element code has been implemented and tested for three-dimensional linear elasticity problems.

• DG is still a pure displacement-based method, which makes the implementation of computer code much easier than other complex alternatives like mixed finite elements. The well established nodal-based 3D CG finite element programs can be fully reused for developing DG code. The coupled use of CG and DG elements can be easily and naturally carried out in this nodal-based DG program. Therefore, DG methods have potential advantages in practical applications.

• DG is proved to be a simple and robust candidate for solving three-dimensional nearly incompressible elasticity problems.

• An effort has been invested in evaluating the performance of different DG schemes for elasticity problems. This family of DG methods have no obvious difference in solving elasticity with normal materials. In solving nearly

incompressible elasticity, however, the OBB is simplest in implementation and testing. The IIPG is most robust and accurate. The NIPG allows to adjust a penalty parameter to achieve a more accurate result. The SIPG is sensitive to the penalty parameter. This detailed evaluation is quite important to selection on DG schemes for the complex coupled systems of thermal, flow and mechanics problems.

2. The first DG formulation for plasticity problems: a three-dimensional DG code has been implemented for solving elastoplasticity problems. The code can handle the Von-Mises and Drucker-Prager materials with or without hardening behaviors. Nonlinear iteration schemes such as initial stiffness method, modified Newton-Raphson and Newton-Raphson method are implemented.

• A technique has been proposed for obtaining any stress at an interface by extrapolating stresses at interior Gaussian points. This can help to save memory and CPU time to store and compute stress evolution on interfaces.

• CG methods are not able to model nearly incompressible plasticity. DG methods have potentials to handle plasticity problems with nearly incompressible materials as they are locking-free methods.

3. Numerical examples have been presented to show that a smaller M is a natural stabilizer for popular CG schemes. Particularly, this work also shows that the decay rate of the oscillation induced by CG methods is independent of CG schemes.

4. A weak formulation of DG methods has been derived for solving poroelasticity models. Discontinuous spaces are proposed for both displacement and pore pressure. A three-dimensional nodal-based DG code has been implemented to verify the proposed DG formulation. The computer program is written in Fortran 90. Isoparametric elements with 8 , 20 and 27 nodes are used, which are particularly important for handling problems with complex curved boundaries.

- DG performance for poroelasticity with very low permeability has been tested and compared with CG methods. It shows that DG is quite robust and powerful to avoid any obvious nonphysical oscillation in pressure.
- Numerical examples demonstrated that DG is particularly useful to model lacuna bone problems.

5. DG has been also proposed to solve elasticity equation while coupled flow equation is solved by cell-centered finite difference methods. A two-dimensional code has been implemented to verify this scheme. Numerical examples show that DG is powerful in avoiding oscillations. This scheme is particularly useful in modeling oil reservoirs where numerical schemes for solving flow problems are dominated by finite difference methods.

6. A weak formulation for DG methods has also been derived for solving thermoporoelastoplasticity models. Discontinuous spaces are proposed for all three fields. DG code for poroelasticity has been extended for this three-field

problem by incorporating the plasticity code and by adding new code for thermal equation.

• The highly nonlinear behavior resulted from plasticity and convection effects in 3-field problems requires the use of very small time steps for CG methods. This requirement can be relaxed if DG methods are used.

• The temperature profile in fine mesh zones predicted by CG methods for the case when the convection dominates the thermal process can be seriously polluted by large errors induced at coarse mesh zones. DG methods are good candidates for avoiding such pollution.

• When CG methods are applied to solve poroelasticity problems, the pressure oscillation induced at early time stages may decay fast. Therefore, CG solutions at longer time will not be polluted seriously. When plasticity effect is taken into account, however, any nonphysical oscillation induced by CG at early time stages will affect solutions at longer time. Because DG methods are able to avoid nonphysical oscillation at early stages and in coarse mesh domains, and restrain errors from propagation, they are highly recommended for solving thermoporoelastoplasticity.

8.2 Future Work

DG methods proposed and studied in this dissertation are proved to be very robust and highly stable for solving poromechanics problems. Further research efforts should include the following directions.

- Parallel algorithms for large 3-field problems solved by DG methods;
- Coupled use of CG and DG methods;
- Automatic refinement and coarsening for coupled CG and DG algorithms;
- Stability and error estimate for 3-field problems.

Bibliography

[1] T. Arbogast, M.F. Wheeler, and I. Yotov. Mixed finite elements for elliptic problems with tensor coefficients as cell-centered finite differences. *SIAM J. Numer. Anal.*, 34:828–852, 1997.

[2] J.H. Argyris. Elasto-plastic matrix analysis of three dimensional continua. *Joural of the Royal Aeronautical Society*, 69:633–635, 1965.

[3] J.H. Argyris and J.St. Doltsinis. On the large strain inelastic analysis in natural formulation. part i: Quasi-static problems. *Computer Methods in Applied Mechanics and Engineering*, 20:213–251, 1979.

[4] D.N Arnold. An interior penalty finite element method with discontinuous elements. *SIAM, J. Numer. Anal.*, 19:742–760, 1982.

[5] F.S. Azar, D.N. Metaxas, M.D. Mitchell, and D. Schnall. A deformable finite element model of the breast for predicting mechanical deformations under external perturbations. *Academic Radiology*, 8:965–975, 2001.

[6] I. Babuska and M. Suri. Locking effects in the finite element approximation of elasticity problems. *Numer. Math.*, 62:439–463, 1992.

[7] G.A. Baker. Finite element methods for elliptic equations using nonconforming elements. *Math. Comp.*, 31:45–59, 1977.

[8] K.J. Bathe. *Finite element procedures.* Englewood Cliffs, New Jersey, 1996.

[9] C.E. Baumann and J.T. Oden. A discontinuous hp finite element method for the euler and navier-stokes equations. *Int J. Numer. Meth. Fluids*, 31:79–95, 1999.

[10] J. Bear and M. Y. Corapcioglu. A mathematical model for consolidation in a thermoelastic aquifer due to hot water injection or pumping. *Wat. Res. Research*, 17:723–736, 1981.

[11] M. Biot. General theory of 3-d consolidation. *J. Appl. Phys*, 12:155–169, 1941.

[12] M. Biot. Theory of elasticity and consolidation for a porous anisotropic solid. *J. Appl. Phys.*, 26:182–185, 1955.

[13] M. Biot. General solutions of the equations of elasticity and consolidation. *J. Appl. Mech.*, 78:91–96, 1956.

[14] M. Biot and D.G. Willis. The elastic coefficient of the theory of of elasticity consolidation. *J. Appl. Mech.*, 79:594–601, 1957.

[15] J.R. Booker and J.C. Small. An investigation of the stability of numerical solutions of biot's equations of consolidation. *Int. J. Solids Struct.*, 11:907–917, 1975.

[16] S. Bougacha, J.M. Roesset, and J.L. Tassoulas. Dynamic stiffness of foundation on fluid-filled poroelastic stratum. *J. Eng. Mech.*, 119:1649–1662, 1993.

[17] S. Bougacha, J.L. Tassoulas, and J.M. Roesset. Analysis of foundations on fluid-filled poroelastic stratum. *J. Eng. Mech.*, 119:1632–1648, 1993.

[18] S.C. Brenner and L.R. Scott. *The mathematical theory of finite element methods*. Springer, New Yorky, 2002.

[19] F. Brezzi and M. Fortin. *Mixed and Hybrid Finite Element Methods*. Springer, Berlin, 1994.

[20] F. Brezzi and J. Pitkarantan. On the stabilization of finite element approximations of the Stokes equations. In W. Hackbusch, editor, *Efficient Solution of Elliptic Systems*. Vieweg, Braunschweig, 1984.

[21] D.H. Brownell and S.K. Pritchett. Governing equations for geothermal reservoirs. *Wat. Res. Research*, 13:929–934, 1977.

[22] A.R. Carslaw and C.J. Jaegar. *Conduction of Heat in Solids*. Oxford at Clarendon Press, London, 1960.

[23] A. H.-D. Cheng and E. Detournay. A direct boundary element method for plane strain poroelasticity. *Int. J. Numer. Analy. Meth. Geomech.*, 12:551–572, 1988.

[24] L.Y. Chin, R. Raghavan, and L.K. Thomas. Fully-coupled geomechanics and fluid-flow analysis of wells with stress-dependent permeability. In *SPE International Conference and Exhibition*, China, November 1998. SPE. SPE 48857.

[25] P.G. Ciarlet. *The finite element method for elliptic problems*. North-Holland, Amsterdam, 1978.

[26] B. Cockburn and C. Dawson. Some extensions of the local discontinuous Galerkin method for convection-diffusion equations in multidimensions. In J.R. Whiteman, editor, *The mathematics of Finite Elements and Applications*. V. Academic Press, London, 1999.

[27] B. Cockburn, G.E. Karniadakis, and C.-W. Shu. *Discontinuous Galerkin Methods: Theory, computation and applications*. Springer Verlag, 2000.

[28] B. Cockburn and C. Shu. The local discontinuous Galerkin finite element method for convection-diffusion systems. *SIAM J. Numer. Anal.*, 35:2440–2463, 1998.

[29] I.C. Cormeau. Numerical stability in quasi-static elasto/visco-plasticity. *International Journal for Numerical Methods in Engineering*, 9:109–127, 1975.

[30] O. Coussy. A general theory of thermoporoelastoplasticity for saturated porous materials. *Transport in Porous Media*, 4:281–293, 1989.

[31] S.C. Cowin. Bone poroelasticity. *Journal of Biomechanics*, 32:217–238, 1999.

[32] C. W. Cryer. A comparison of the three-dimensional consolidation theories of biot and terzaghi. *Quart. J. Mech. Appl. Math.*, 16:401–412, 1963.

[33] L. Cui, Y. Abousleiman, A.H.-D. Cheng, V.N. Kaliakin, and J.-C. Roegiers. Finte element analysis of anisotropic poroelasticity: a generalized mandel's problem and an inclined borehole problem. *Int. J. Numer. Anal. Meth. Geomech.*, 20:381–401, 1996.

[34] C.N. Dawson, S. Sun, and M.F. Wheeler. Compatible algorithms for coupled flow and transport. *Comput. Methods Appl. Meth. Engrg.*, 193:2565–2580, 2004.

[35] R.H. Dean. A poroelastic multicomponent reservoir simulator. *unpublished*, 2000.

[36] R.H. Dean, X. Gai, C.M. Stone, and S.E. Minkoff. A comparison of techniques for coupling porous flow and geomechanics. In *SPE Reservoir Simulation Symposium*, Houston, February 2003. SPE. SPE 79709.

[37] E. Detournay and A. H.-D. Cheng. Poroelastic response of a borehole in non-hydrostatic stress field. *Int. J. Rock Mech. Min. Sci. Geomech. Abstr.*, 25:171–182, 1988.

[38] J. Douglas and T. Dupont. Interior penalty procedures for elliptic and parabolic Galerkin methods. *Lecture Notes in Physics*, 58:207–216, 1976.

[39] J.H. Ferziger and M. Periu. *Computational Methods for Fluid Dynamics*. Springer, Verlag Berlin Heidelberg, 1999.

[40] L.P. Franca, T.J.R. Hughes, and R. Stenberg. Stabilized finite element methods for the Stokes problem. Technical Report Research Report 11, Laboratory for Strength of Materials, Helsinki University of Technology, 1991.

[41] Y.C. Fung. *Biomechanics: mechanical properties of living tissues*. Springer-Verlag,New York, 1981.

[42] X. Gai. *A Coupled Geomechanics and Reservoir Flow Model on Parallel Computers*. PhD thesis, The University of Texas at Austin, Austin, Texas, 2004.

[43] Y.F. Gao and A.F. Bower. A simple technique for avoiding convergence problems in finite element simulations of crack nucleation and growth on cohesive interfaces. *Modeling and Simulation in Materials Science and Engineering*, 12:453–463, 2004.

[44] J. Ghaboussi and E. L. Wilson. Flow of compressible fluid in porous elastic media. *Int. J. Numer. Meth. Engrg.*, 5:419–442, 1973.

[45] R.E. Gibson, R.L. Schiffman, and S.L. Pu. Plane strain and axially symmetric consolidation of a clay layer on a smooth impervious base. *Quart. J. Mech. and Applied Math.*, 23:505–520, 1970.

[46] A.E. Green and P.M. Naghdi. A general theory of an elastic-plastic continuum. *Archive for Rational Mechanics and Analysis*, 18:251–281, 1965.

[47] M.E. Gurtin. Variational principles for linear elastodynamics. *Archives for Rational Mechanics and Analysis*, 16:34–50, 1964.

[48] M.E. Gurtin. *An introduction to continuous mechanics.* Academic Press, Orlando, Fl., 1981.

[49] W. Han and B.D. Reddy. *Plasticity-Mathematical Theory and Numerical Analysis.* Springer-Verlag, New York, Inc., 1999.

[50] P. Hansbo and M.G. Larson. Discontinuous Galerkin method for incompressible and nearly incompressible elasticity by nitche's methods. *Computer Meth. for Appl. Mech. Engrg.*, 191:1895–1908, 2002.

[51] R. Hill. *The mathematical theory of plasticity.* Oxford University Press, Oxford, U.K., 1950.

[52] R. Hill. A general theory of uniqueness and stability in elasto-plastic solids. *Journal of Mechanics and Physics of Solids*, 6:236–249, 1958.

[53] J.T.R. Hughes. Consistent linearization in mechanics of solid and structures. *Computers and Structures*, 9:391–397, 1978.

[54] J.T.R. Hughes. Unconditionally stable algorithms for quasi-static elasto/viscoplastic finite element analysis. *Computers and Structures*, 8:169–173, 1978.

[55] J.T.R. Hughes. *Numerical implementation of constitutive models: Rate-independent deviatoric plasticity, in Theoretical Foundations for Large Scale Computations of Nonlinear Material Behaviors, eds., S. Nemat-Nasser, R. Asaro, and G. Hegemier.* Martinus Nijhoff Publishers, Dordrecht, The Netherlands, 1984.

[56] J.T.R. Hughes. *The finite element method.* Prentice-Hall, Englewood Cliffs, N.J., 1987.

[57] C.T. Hwang, N.R. Morgenstern, and D.W. Murray. On solutions of plane strain consolidation problems by finite element methods. *Canad. Geotech. J.*, 8:109–118, 1971.

[58] Jeager and Cook. *Fundamentals of Rock Mechanics.* Chapman and Hall, London, 1979.

[59] C. Johnson and V. Thomee. Error estimates for some mixed finite element methods for parabolic type problems. *RAIRO Anal. Numer.*, 15:41–78, 1981.

[60] L.M. Kachanov. *Foundation of the theory plasticity.* North-Holland, Amsterdam, 1971.

[61] S.J. Kim and J.T. Oden. Generalized potentials in finite elastoplasticity. *Journal of Engineering Sciense*, 22:1235–1257, 1984.

[62] R.W. Lewis and B.A. Schefler. A fully coupled consolidation model of the subsidence of venice. *Water Res. Research*, 14:223–30, 1978.

[63] R.W. Lewis and B.A. Schefler. *The Finite Element Method in the Deformation and Consolidation of Porous Media*. Wiley, New York, 1987.

[64] L.P. Li, G. Cederbaum, and K. Schulgasser. A finite element model for poroelastic beams with axial diffusion. *Computers and Structures*, 73:595–608, 1999.

[65] J. Lubliner. *Plasticity theory*. Macmillan, New York, 1990.

[66] L.X. Luccioni, J.M. Pestana, and R.L. Taylor. Finite element implementation of non-linear elastoplastic constitutive laws using local and global explicit algorithms with automatic error control. *International Journal for Numerical Methods in Engineering*, 50:1191–1212, 2001.

[67] D.S. Malkus and T.J.R. Hughes. Mixed finite element methods-reduced and selective integration techniques: a unification of concepts. *Comput. Methods Appl. Mech. Engrg.*, 15, 1978.

[68] J. Mandel. Consolidation des sols. *Geotechnique*, 3:287–299, 1953.

[69] G.A. Maugin. *The thermomechanics of plasticity and fracture*. Cambridge University Press, 1992.

[70] J. McNamee and R.E. Gibson. Plane strain and axially symmetric problems of the consolidation of a semi-infinite clay stratum. *Quart. J. Mech. and Applied Math.*, 13:210–227, 1960.

[71] M.A. Murad and A.F.D. Loula. Improved accuracy in finite element analysis of Biot's consolidation problem. *Comput. Methods Appl. Mech. Engrg.*, 95:359–382, 1992.

[72] M.A. Murad and A.F.D. Loula. On stability and convergence of finite element approximations of Biot's consolidation problem. *J. Numer. Methods Engrg.*, 37:645–667, 1994.

[73] M.A. Murad, V. Thomee, and A.F.D. Loula. Asymptotic behavior of semidiscrete finite element approximations of Biot's consolidation problem. *SIAM J. Numer. Anal.*, 33:1065–1083, 1996.

[74] J. Nitsche. über ein variationsprinzip zur lösung von dirichlet bei verwendung von teilräumen, die keinen randbedingungen unterworfen sind. *Abh. Math. Univ. Hamburg*, 36:9–15, 1970.

[75] J.L. Nowinski and C.F. Davis. The flexure and torsion of bones viewed as anisotropic poroelastic bodies. *Int. J. Engrg Sci.*, 10:1063–1079, 1972.

[76] J.T. Oden. *Finite Element of Nonlinear Continua*. McGrow-Hill Book Company, New York, 1972.

[77] J.T. Oden, I. Bubuska, and C.E. Baumann. A discontinuous hp finite element method for diffusion problems. *J. Comput. Phys.*, 146:491–519, 1998.

[78] J.T. Oden and G.F. Carey. *Finite Elements : Mathematical Aspect.* Prentice Hall, Englewood Cliffs, NJ, 1982.

[79] J.T. Oden and O.-P. Jacquotte. Stability of some mixed finite elements for stokesian flows. *Computer Methods Appl. Mech. Engrg.*, 43:231–247, 1984.

[80] J.T. Oden, N. Kikuchi, and Y. J. Song. Penalty-finite element methods for the analysis of stokesian flows. *Comp. Meth. Appl. Mech. Eng.*, 31:297–329, 1982.

[81] J.T. Oden and J.N. Reddy. *Variational Methods for Theoretical Mechanics.* Springer-Verlag, Berlin, 1976.

[82] M. Ortiz and J.C. Simo. Accuracy and stability of integration algorithms for elastoplastic constitutive equtions. *International Journal for Numerical Methods in Engineering*, 21:1561–1576, 1985.

[83] M. Ortiz and J.C. Simo. Analysis of a new calss of integration algorithms for elastoplastic constitutive relations. *International Journal for Numerical Methods in Engineering*, 23:353–366, 1986.

[84] P. Percell and M.F. Wheeler. A local residual finite element procedure for elliptic equations. *SIAM J. Numer. Anal.*, 15:705–714, 1978.

[85] P.J. Phillips and M.F. Wheeler. A coupling of mixed and Galerkin finite element methods for poroelasticity. *to appear*, 2003.

[86] M.B. Reed. An investigation of numerical errors in the analysis of consolidation by finite elements. *Int. J. Numer. Analy. Meth. Geomech.*, 8:243–257, 1984.

[87] L. Resende and J.B. Martin. Formulation of Drucker-Prager cap model. *Journal of Engineering Mechanics*, 117(7):855–865, 1986.

[88] J.R. Rice and M.P. Cleary. Some basic stress-diffusion solutions for fluid saturated elastic porous media with compressible constituents. *Rev. Geophys. Space Phys.*, 14:227–241, 1976.

[89] B. Riviere, M.F. Wheeler S. Shaw, and J.R. Whiteman. Discontinuous Galerkin finite element methods for linear elasticity and quasi-static linear viscoelasticity. Technical Report TICAM Report 01-04, The University of Texas at Austin, 2001.

[90] B. Riviere and M.F. Wheeler. Optimal error estimates for discontinuous Galerkin methods applied to linear elasticity problems. Technical Report TICAM Report 00-30, The University of Texas at Austin, 2000.

[91] B. Riviere, M.F. Wheeler, and K. Banas. Part ii: Discontinuous Galerkin method applied to a single-phase flow in porous media. *Computational Geosciences*, 4:337–349, 2000.

[92] A. Romkes. *Modeling of Wave Phenomena in Heterogeneous Elastic Solid*. PhD thesis, The University of Texas at Austin, Austin, Texas, 2003.

[93] A. Romkes, J.T. Oden, and S. Prudhomme. A priori error analysises of a stabilized discontinuous Galerkin method. Technical Report TICAM Report 02-28, The University of Texas at Austin, 2002.

[94] R.S. Sanhu, S.C. Lee, and H.-L. The. Special finite element for analysis of soil consolidation. *Int. Numer. Meth. Geomech*, 9:125–147, 1985.

[95] R.S. Sanhu, H. Liu, and K.J. Singh. Numerical performance of some finite element schemes for analysis of seepage in porous elastic media. *Int. J. Numer. Analy. Meth. Geomech.*, 1:177–194, 1977.

[96] R.S. Sanhu and E.L. Wilson. Finite element analysis of seepage in elastic media. *J. Engrg. Mech. Div. Amer. Soc. Civil Engrg.*, 95:641–652, 1969.

[97] A. Settari and D.A. Walters. Advanced in coupled geomechanics and reservoir modeling with applications to reservoir compaction. In *the SPE Reservoir Simulation Symposiu*, Houston, February 1999. SPE. SPE 5192.

[98] J.F. Shao. A numerical solution for a thermo-hydro-mechanical coupling problem with heat convection. *Int. J. Rock Mech. and Min. Science*, 34:163–166, 1997.

[99] J.F. Shao, J.P. Henry, F. Skoczylas, and I. Shahrour. Study of massive water injection by thermoporomechanical coupling model. *Computer and Geotechnics*, 15:105–121, 1993.

[100] J.C. Simo and T.J.R. Hughes. *General return mapping algorithms for rate independent plasticity in Constitutive Laws for Engineering Materials, ed., C.S. Desai*. Elsevier, N.Y., 1987.

[101] J.C. Simo and T.J.R. Hughes. *Computational Inelasticity*. Springer-Verlag, New York, Inc., 1998.

[102] J.C. Simo and R.L. Taylor. Consistent tangent operators for rate independent elasto-plasticity. *Computer Methods Appl. Mech. Engrg.*, 48:101–118, 1985.

[103] B.R. Simon. Multiphase poroelastic finite element models for soft tissue structures. *Applied Mechanical Reviews*, 45:191–218, 1992.

[104] H.J. Siriwardane and C.S. Desai. Two numerical schemes for nonlinear consolidation. *Int. J. Num. Meth. Eng.*, 17:405–426, 1981.

[105] S. Sun. *Discontinuous Galerkin Methods for Reactive Transport in Porous Media*. PhD thesis, The University of Texas at Austin, Austin, Texas, 2003.

[106] S. Sun and X. Gai. The mid term project for CAM 383. Technical report, The University of Texas at Austin, 2000.

[107] S. Sun and M.F. Wheeler. Symmetric and non-symmetric discontinuous Galerkin method for reactive transport in porous media. *SIAM Journal on Numerical Analysis*, to apprear.

[108] R.L. Taylor, P.J. Bereford, and E.L. Wilson. A nonconforming element for stress analysis. *Int. J. Numeri. Method.*, 10:1211–1219, 1976.

[109] K. Terzaghi. *Theoretical Soil Mechanics*. Wiley, New York, 1942.

[110] V. Thomee. *Galerkin finite element methods for parabolic problems, Lecture notes in Mathematics 1054*. Springer, Berlin, 1984.

[111] P.A. Vermeer and A. Verruut. An accuracy condition for consolidation by finite elements. *Int. J. Numer. Analy. Meth. Geomech.*, 5:1–14, 1981.

[112] A. Verruijt. Discussion. In *Proc. 6th Int. Conf. Soil Mechanics and Foundation Engineering*, Montreal, February 1965. vol 3, pages: 401-402.

[113] A. Verruijt. Elastic storage of aquifers. In R.J.M. DeWiest, editor, *Flow through porous media*. New York: Academic Press, 1965. pages: 331-376.

[114] J. Wan. *Stabilized finite element methods for coupled geomechanics and multiphase flow*. PhD thesis, Stanford University, San Jose, California, 2002.

[115] L.C. Wellford and J.T. Oden. A theory of discontinuous finite element approximations for the analysis of shock waves in nonlinear elastic materials. *Journal of Computational Physics*, 19:179–210, 1975.

[116] John Wheeler and Mary Wheeler. IPARS user's manual. Technical report, ICES, The University of Texas at Austin, 2000.

[117] M.F. Wheeler. A priori l^2 error estimates for Galerkin approximations to parabolic partial differential equations. *SIAM J. Numer. Anal.*, 10:723–759, 1973.

[118] M.F. Wheeler. An elliptic collocation finite element method with interior penalties. *SIAM J. Numer. Anal.*, 15:152–161, 1978.

[119] M.F. Wheeler and R.J. Liu. Discontinuous Galerkin finite element solution of 3d elasticity. In *Proceedings of the second MIT Conference on Computational Fluid and Solid Mechanics*, June 2003. Pages: 2170-2172.

[120] T.P. Wihler. Locking-free DGFEM for elasticity problems in polygons. Technical Report Research Report 2002-14, Seminar fur Angewandte Mathematik, Eidgenossische Technische Hochschule, 2002.

[121] C. Williams, I.A. KakadarisK, K. Ravi-Chandar, M.J. Miller, and C. W. Patrick. Simulation studies for predicting surgical outcomes in breast reconstructive surgery. *Lecture Notes in Computer Science*, (2878):9–16, 2003.

[122] Y. Yokoo, K. Yamagata, and H. Nagaoka. Finite element method applied to Biot's consolidation. *Soils and Foundations*, 11(1):29–46, 1971.

[123] Y. Yokoo, K. Yamagata, and H. Nagaoka. Variational principles for consolidation. *Soils and Foundations*, 11(4):25–36, 1971.

[124] A. Zenisek. The existence and uniqueness theorem in Biot's consolidation theory. *Appl. Ma.*, 29:194 –210, 1984.

[125] D. Zhang and S.C. Cowin. Oscillatory bending of a poroelastic beam. *Journal of Mechanical Physics Solids*, 42:1575–1599, 1994.

[126] O.C. Zienkiewicz and T. Shiomi. Dynamic behavior of saturated porous media: the generalized biot formulation and its numerical solution. *Int. J. Numer. Anal. Meth. geomech.*, 8:71–79, 1984.

Vita

Ruijie Liu was born in Tianjin, China on October 6, 1964, the third son of Shubai Liu and Ruiying Li. After completing his B.S. in Applied Mechanics and M.S. in Ocean Egineering in 1987 and 1990 at Tianjin University, China, he worked as a research engineer in offshore engineering during 1990-1996. He entered U.S.A. at the end of 1996 and received a master degree in civil engineering in the summer of 1998 from West Virginia University. In summer of 2000, he transfered to The university of Texas at Austin from Texas A & M University and continued to work toward a Ph.D. in Aerospace Engineering and Engineering Mechanics.

Permanent address: Xi-Nian-Cun, Building 62-2-305
Nankai University
Tianjin 200031, China

This dissertation was typeset with LaTeX[†] by the author.

[†]LaTeX is a document preparation system developed by Leslie Lamport as a special version of Donald Knuth's TeX Program.